VOLUME HOLOGRAPHIC INFRA-RED FILTERS

IN IRON DOPED LITHIUM NIOBATE

P. A. Mills

Hertford College

Oxford

A thesis submitted for the degree of Doctor of Philosophy at the University of Oxford

Michaelmas Term 1985

THE DEPARTMENT OF ENGINEERING SCIENCE

Parks Road

Oxford

To my mother and father.

VOLUME HOLOGRAPHIC INFRA-RED FILTERS

IN IRON DOPED LITHIUM NIOBATE

P. A. Mills

Hertford College, Oxford

A thesis submitted for the degree of Doctor of Philosophy

UNIVERSITY OF OXFORD

Michaelmas Term 1985

ABSTRACT

Two collimated laser beams, wavelength 0·514 μm are overlapped within a crystal of heavily iron doped lithium niobate to form a one-dimensional volume holographic grating, a few mm long, designed to behave as a highly selective filter at near infra-red wavelengths. A novel recording geometry is described and a variety of diagnostic experiments are undertaken to determine the main characteristics of the grating. A filter fabricated using this method is used to obtain single mode operation from a 1·55 μm semiconductor laser.

The historical survey of holography contained in chapter one emphasizes the dynamic properties and applications of photorefractive recording materials. Standard results of two mathematical theories, kinematic and coupled-wave, are used in chapter two to predict the properties of a Bragg grating when replayed with infra-red light. Chapter three details the recording materials suitable for an infra-red filter, followed by a discussion on the concept of 'scaling'. The recording mechanism of iron doped lithium niobate, including its fixing and erasure process, is presented in chapter four as a basis for selecting the most advantageous crystal characteristics. Mathematical models describing the complex dynamic recording process in iron doped lithium niobate are introduced in chapter five. A novel recording geometry involving the use of two prisms is critically described in chapter six, from initial conception to final implementation. The performance of the grating as an infra-red filter is assessed in chapter seven by measuring the angular response of the transmitted and diffracted beams at a wavelength of 1·152 microns. Chapter eight discusses the applications for volume holographic filters, with particular reference to one example. In chapter nine general conclusions are drawn and future directions for research are suggested. A number of appendices are also included.

ACKNOWLEDGEMENTS

With much appreciation I acknowledge the continued help of my supervisor Prof. E.G.S. Paige, whose advice, guidance and support has been invaluable during this research. I am also greatly indebted to Dr. L. Solymar for his constant interest and encouragement.

Special thanks are due to Richard Syms, Andrew Ward and Jeno Takacs for their patience and constructive advice. I must also express sincere thanks to my fellow members of the holography group, John Heaton, Christopher Newell, Sheila Rai, and Christopher Slinger, along with Douglas Hamilton, for their inspiration and fruitful discussions. The technical help from Brian French and Graham Reid with material preparation has been a considerable assistance.

I am grateful for the generous cooperation of Murdo Fraser of Barr & Stroud, Scotland who supplied the boules of iron doped lithium niobate and for the financial support provided by a CASE award from the Science and Engineering Research Council in conjunction with British Aerospace.

INDEX

CHAPTER ONE

INTRODUCTION

I.1 INTRODUCTION

For many years, primarily due to the lack of suitable materials, the promising potential for holography has not been fully realised. Despite these setbacks, however, holography has recently received a resurgence of interest. Associated with the development of improved materials, there are new prospects for practical applications in the expanding technological fields of optical communication systems, signal processing, displays, and storage devices. This thesis specifically concentrates on the applications of holography to infra-red optics, a wavelength band increasingly important in these fields.

The technique of holography can be conveniently separated into two stages called 'recording' and 'replay'. Recording involves the production of a standing wave interference pattern where two or more wavefronts overlap. If a constant temporal relationship exists between the phases of the recording beams, the light pattern will be stationary and a copy can be stored in a photo-sensitive material as a variation of impedance. This is a hologram. A hologram can be classified as either 'planar' or 'volume', but there is no clear cut division. At one extreme there is the surface relief hologram, whereas at the other there is the hologram which derives its performance from a vast number of reflecting planes in the volume of an extensive medium. This thesis will be exclusively involved with the properties and applications of volume holograms.

The second stage called 'replay' can be realised because a hologram has the special ability to reconstruct the phase and intensity distribution of one wavefront from another by the process of diffraction. Re-exposing the hologram to one of the recording beams will reconstruct the other beams present during recording. A popular demonstration of this process is the display hologram, projecting illusionary, lifelike images of three dimensional objects, where the diffracted beams reproduce the rays of scattered light from the original scene.

If the reconstructed wavefront is simpler, the hologram will, for a particular wavelength, perform functions usually associated with conventional optical elements (COE's). For example, a spherically converging beam of light can either be generated by a convex lens or a hologram. When both recording beams have a planar phase front, the hologram becomes a one dimensional periodic grating, which will strongly diffract a collimated beam of light. These types of hologram are usually called volume holographic optical elements [20] or VHOE's. The general advantages of VHOE's are:

1) Once the initial capital investment has been made their manufacture can be cheap and simple.

2) Simultaneous performance of several functions is possible by storing a set of holograms.

3) Parallel performance of the same or different function can be achieved.

4) They have an unconventional shape and lightweight design.

Notable devices which have commercially used VHOE's are the holographic mirror in a jet fighter [32], allowing a Head Up Display of instrumentation, and the high speed rotating supermarket scanner [28] consisting of a set of holographic lenses on a flat disc.

I.2 HISTORICAL

The motivation for what is now called holography was originally to produce an enlarged image of an atomic structure without resorting to electron lenses. To reproduce both the intensity and relative position of the different atoms in the crystal, Gabor [35] had to devise a technique capable of retaining the phase information about the structure. In his method, a planar hologram would be recorded where the electrons reflected off the atomic planes interfered with the nearly undepleted transmitted beam. The idea was to magnify the resultant hologram and then recreate an image of the atomic structure by exposing the hologram to an analogue of the original electron beam at optical wavelengths. To test the idea, he initially used optical radiation to both record and replay the hologram. The trial experiment was a partial success because this particular geometry, responsible for forming the first in-line hologram, was hardly affected by the limited temporal coherence of the source.

Lippmann's colour photographs [58] were the inspiration for the first type of truly volume hologram. In this technique, a mirror was fixed behind a photographic plate coated with a photo-sensitive layer of gelatin about 10 microns thick. On exposing the plate to a collimated beam of light, a stable pattern of light and dark intensity fringes was formed parallel to the mirror, where the incident beam interfered with its reflected counterpart. For normal incidence illumination, each wavelength, λ, in the recording beam formed a sinusoidal pattern with

fringe spacing of $\lambda/2$. When the mirror was removed and the emulsion was chemically developed, the hologram became a frequency selective filter. If the Lippmann hologram is then exposed to light of wavelength λ, with coherence length at least twice the thickness of the gelatin, the diffracted light from each part of the hologram will combine in phase, depleting the transmitted component of the incident beam.

The laser, invented in the early 1960's, offered a monochromatic light source with good coherence which overcame many of the early recording problems and increased the versatility of holography. The two interfering beams could now travel from source to hologram along very different paths, forming what is generally known today as an 'off-axis' hologram. Dennisyuk [27] extended the work of Lippmann-Bragg making different types of reflection hologram in photographic emulsion, including the first holographic version of a curved mirror, while Leith and Upatnieks [56] investigated display holography.

All the early investigations of holography used a latent recording material, namely photographic emulsion. In this class of material an additional development step is essential to produce the final impedance variation. The variety of recording materials was markedly increased by the discovery of a new class which had dynamic recording properties. These materials are different because no further processing after recording is needed to create the final hologram. The interest in dynamic photorefractive materials began in 1966 when Ashkin [6] noticed that an optically-induced refractive index inhomogeneity could be produced in crystals of lithium niobate ($LiNbO_3$), and lithium tantalate ($LiTaO_3$) when a visible laser beam was focussed onto the material. Chen [18] was the first person to demonstrate that this effect could be exploited to form a volume holographic phase grating in a crystal of iron doped lithium niobate. Other photorefractive materials now used for holography are SBN, KTN, BSO, BGO, GaAs and InP.

One early direction of research with these materials was to use their high spatial resolution to develop systems for the compact storage and retrieval [3] of information. The reversible recording properties of the faster responding photorefractives, like BSO, were also considered for optical real-time image processing [61].

Storage of information is possible because several holograms can be stored in the same volume of material either by angular or frequency multiplexing. Angular multiplexing was first demonstrated by Staebler [85] who sequentially recorded 500 holograms in a crystal of lithium niobate. Despite the promising potential [45] to store a large density of data, interest in the subject waned following the discovery that only a poor signal to noise ratio could be achieved.

Real-time applications concentrated on interferometry, coherent beam amplification and aspects of four wave mixing, like phase conjugation (PC). A good review of the whole subject is written by Yariv [25]. PC began to receive widespread attention in the mid 1970's with the invention of the PC mirror, which unlike a normal mirror, could correct the distortion in a laser beam caused by an aberrating medium Huignard [46] used BSO crystals to produce clear, time-averaged, interference patterns of vibrating membranes and also demonstrated amplification.

The refractive index in these electro-optic materials can also be changed by applying an external electric field. The practical limitation with this effect is its weakness, implying that either high voltages or short distances are required to generate sufficient field strength. Bulk material can switch high input intensities, as demonstrated by the Pockels cell, but needs kV to operate. Integrated optical devices, on the other hand, overcome the difficulty by reducing one of the material dimensions to microns, so that only about 100 V is sufficient to modulate the light output.

I.3 THESIS SUMMARY

This work discusses the fabrication and properties of a highly selective infra-red filter recorded in a crystal of iron doped lithium niobate. The special attributes of lithium niobate as a holographic recording material are firstly, its low absorption in the infra-red to a wavelength of 5 microns, secondly its electro-optic properties, and thirdly, its relatively large physical size (crystals with dimensions of mm^3 are common). Although only the performance of filters in the 1 to 2 micron infra-red wavelength band has been measured, the principles can be applied to devices operating at longer wavelengths.

CHAPTER TWO

FILTER PERFORMANCE

II.1 INTRODUCTION

In this chapter, the complex mechanism of dynamic grating formation in iron doped lithium niobate is disregarded and it is assumed that a time-independent volume grating has been created which will diffract light. At infra-red wavelengths the probe beam will not affect the grating. Consequently, as described below, a standard latent theory can be used to predict the expected performance of the filter.

II.2 KINEMATIC THEORY

The theoretical models, describing the optical interaction of a light beam with a passive hologram are based on the analysis of X-ray

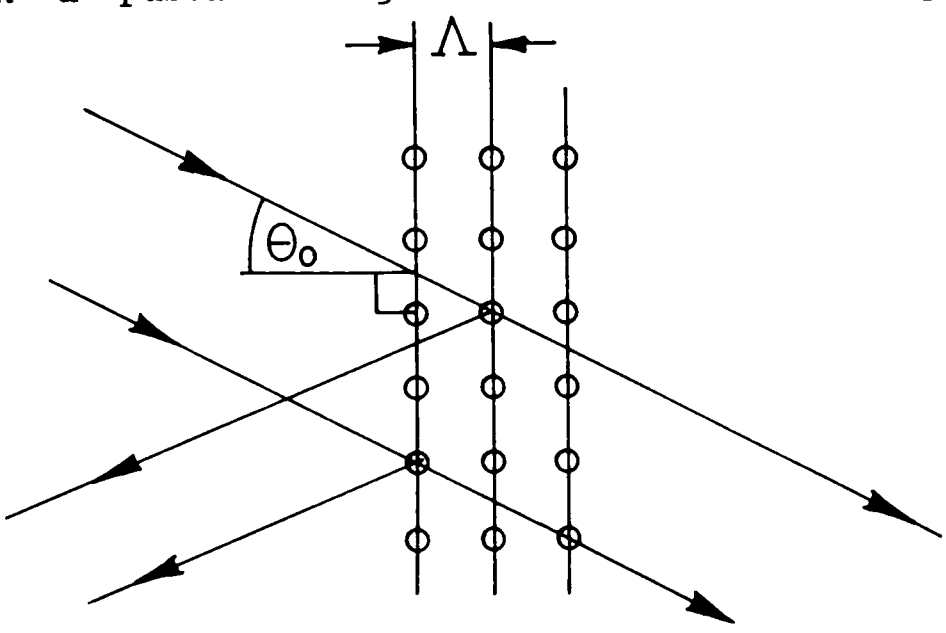

Fig 2.1: Diffraction from a large array of regularly spaced atoms

diffraction by crystals. Bragg [12] considered the interference of scattered X-rays from a large array of regularly spaced atoms (see Fig

2.1) and determined the condition for a strong diffracted beam to be produced. He used a kinematic theory, where multiple reflections are ignored and the incident beam is assumed to be undepleted (the low efficiency approximation). For constructive phase addition of the diffracted radiation,

$$2\,\tilde{n}\,\Lambda\cos(\theta_o) = \lambda \qquad (2.1)$$

where Λ is the spacing between the atomic planes, λ the wavelength of the radiation, θ_o the angle of incidence and $\tilde{n}$ the isotropic bulk refractive index of the medium.

In one dimension the structure can be represented by a set of delta functions, spacing Λ, convolved with a permittivity distribution. If this periodic function is expanded as a Fourier series, and only the first two terms are selected,

$$\tilde{\epsilon}_H(z) = \tilde{\epsilon} + \tilde{\Delta\epsilon}\cos(Kz) \qquad (2.2)$$

where ϵ_H is the permittivity in the hologram, ϵ the average permittivity, $\tilde{\Delta\epsilon}$ the modulated permittivity contribution, and K is magnitude of the grating wavevector $\underline{K}$, with value $\frac{2\pi}{\Lambda}$. The diffracted intensity from these grating planes can be written as $|SS^*|$ where S is the diffracted amplitude. In the kinematic limit,

$$S = \sum_{N=0}^{N=N_m-1} S_N e^{iN\zeta} \qquad (2.3)$$

where N_m is the number of planes. For a medium with no absorption,

$$\zeta = 2\,\beta\,\Lambda\cos(\theta) \qquad (2.4)$$

$$\beta = \frac{2\pi\,\tilde{\epsilon}^{1/2}}{\lambda} = \frac{2\pi\,\tilde{n}}{\lambda} \qquad (2.5)$$

Ewald [31] expressed equation (2.1) in reciprocal or $\underline{K}$-space. The Bragg condition will then be satisfied when the incident $\underline{\rho}$, diffracted $\underline{\sigma}$ and grating $\underline{K}$ wavevectors form a closed triangle.

$$\underline{\rho} - \underline{\sigma} = \underline{K} \qquad (2.6)$$

A common graphical representation of this condition is the Ewald circle, in two dimensions (see Fig 2.2), or the Ewald sphere, in three dimensions, since for an isotropic medium

$$|\underline{\rho}| = |\underline{\sigma}| = \beta. \qquad (2.7)$$

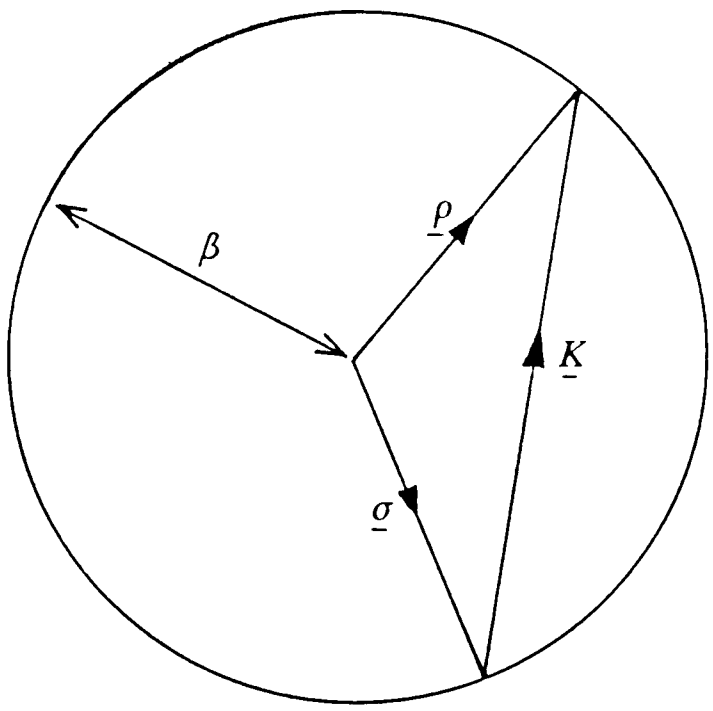

Fig 2.2: Ewald representation of the Bragg condition in two dimensions

This physical picture for a volume grating introduces the idea of 'selectivity' - a constraint between the three variables, wavelength, incident angle and grating spacing, which is not present for a planar grating. Only one diffracted beam is produced from a given set of grating planes.

II.3 COUPLED-WAVE THEORY

Later theories tackled the scattering problem by directly solving Maxwell's wave equation for a general hologram not necessarily volume in character. The particular model used in this thesis is called 'coupled-wave theory'. It accounts for the redistribution of power between incident and diffracted beams and is not restricted like kinematic theories to the low efficiency regime. To simplify the mathematics, fast

varying second derivatives of terms are usually neglected from the starting equations. However, the following limitations are then imposed: self-diffraction is neglected (the geometrical optics condition that an infinitely wide plane wave is incident on the hologram); the propagation direction of the diffracted light is ambiguously defined; Fresnel reflections from the impedance discontinuities at the hologram boundaries have to be separately included; and only a small absorption loss or energy coupling per unit wavelength is assumed - but in practice this is always true.

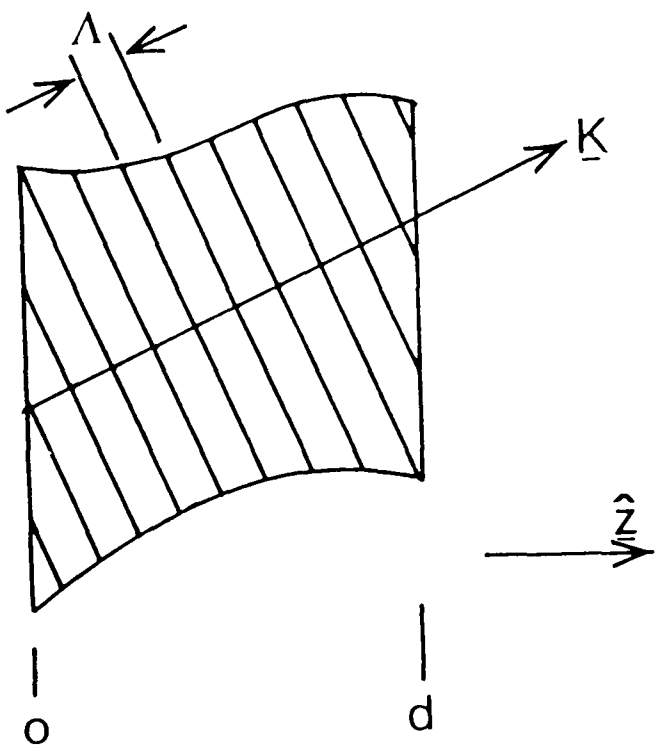

Fig 2.3: Diagram of volume grating

Consider a volume hologram of thickness d, consisting of a one dimensional cosinusoidal grating. Since the electric field polarisation of the incident light is assumed to be perpendicular to the plane of incidence, wave propagation can be described by the following scalar wave equation.

$$\nabla^2 \tilde{E} + k_H^2 \tilde{E} = 0 \qquad (2.8)$$

where,

$$k_H^2 = \left[\frac{\omega^2}{c^2}\tilde{\epsilon}_H\right] \qquad (2.9)$$

$$\tilde{\epsilon}_H = \tilde{\epsilon} + i\tilde{\epsilon}'' + (\Delta\tilde{\epsilon} + i\Delta\tilde{\epsilon}'') \cos(\underline{K} \cdot \underline{\hat{z}} + \Xi) \qquad (2.10)$$

$\tilde{E}$ is the complex, time-independent amplitude of the light electric field inside the hologram, k_H is the propagation constant inside the hologram, c is the velocity of light in free space, ω the angular frequency and Ξ is an arbitrary phase shift. Examining equation (2.10) there are generally four contributions to the permittivity $\tilde{\epsilon}_H$ inside the hologram. The real term $\tilde{\epsilon}$ is the average permittivity, whereas the imaginary term $i\tilde{\epsilon}''$ represents bulk absorption within the crystal. The term $\Delta\tilde{\epsilon}$ is the permittivity modulation strength. The term $i\Delta\tilde{\epsilon}''$ responsible for absorption modulation is assumed to be zero in lithium niobate.

According to Floquet's theorem, the electric field $\tilde{E}$ can be generally written as an infinite Fourier series of grating period harmonics. It implies that the grating can couple energy into a whole series of diffracted beams or excited orders, each denoted by a different value for L. In one dimension,

$$\tilde{E}(z) = \sum_{L=-\infty}^{L=+\infty} A_L(z) \exp(-i \underline{\rho}_L \cdot \underline{\hat{z}}) \qquad (2.11)$$

If the diffracted and transmitted wavevectors always form a closed triangle with multiples of the grating wavevector (the '$\underline{K}$-vector approximation')

$$\underline{\rho}_L = \underline{\rho}_0 + L\,\underline{K} \qquad (2.12)$$

Note the temporary change in notations. The incident wave now has a subscript zero and the diffracted wave with wavevector $\underline{\rho}_0 - \underline{K}$ (previously denoted by $\underline{\sigma}$) is called the - 1 mode. Substituting equation (2.11) into the wave equation,

$$\sum_{L=-\infty}^{\infty} \exp\left[-i\underline{\rho}_L \cdot \underline{\hat{z}}\right] \left[\frac{\partial^2 A_L}{\partial z^2} - 2i(\underline{\rho}_L \cdot \underline{\hat{z}}) \frac{\partial A_L}{\partial z} + \left[\beta^2 - \rho_L^2\right] A_L - 2i\alpha\beta A_L + 2\kappa\alpha\beta\left[\exp(+i\underline{K} \cdot \underline{\hat{z}} + i\Xi) + \exp(-i\underline{K} \cdot \underline{\hat{z}} - i\Xi)\right] A_L\right] = 0 \qquad (2.13)$$

where,

$$\kappa = \frac{\beta}{4}\frac{\Delta\tilde{\epsilon}}{\tilde{\epsilon}} = \frac{\pi}{\lambda}\Delta\tilde{n}, \quad \alpha = \frac{\beta}{2}\tilde{\epsilon}'' \qquad (2.14)$$

By neglecting second derivatives and equating exponential terms of the same order, an infinite set of coupled differential equations are generated,

$$\sum_{L=-\infty}^{\infty} \frac{\rho_{Lz}}{\beta}\frac{\partial A_L}{\partial z} + (\alpha + i\gamma_L) A_L + i\kappa\left[A_{L+1}e^{i\Xi} + A_{L-1}e^{-i\Xi}\right] = 0 \qquad (2.15)$$

where,

$$\gamma_L = \frac{\beta^2 - \rho_L^2}{2\beta} \qquad (2.16)$$

$$\rho_{Lz} = \underline{\rho}_L \cdot \hat{\underline{z}} \qquad (2.17)$$

According to equation (2.3), when the Bragg condition is not satisfied, ζ is not an integral number of 2π, the scattered waves have different phases, and the diffraction efficiency is reduced. For the '$\underline{K}$-vector closure' coupled-wave theory used here, this 'off-Bragg' contribution is associated with a non-zero value for the 'dephasing term' γ_L defined in equation (2.16). The magnitude of γ_L for each order is determined by the distance between the Ewald sphere and the end of the $\underline{\rho}_L$ vector. Figure 2.4 shows the 'on-Bragg' and 'off-Bragg' geometry for L = -1.

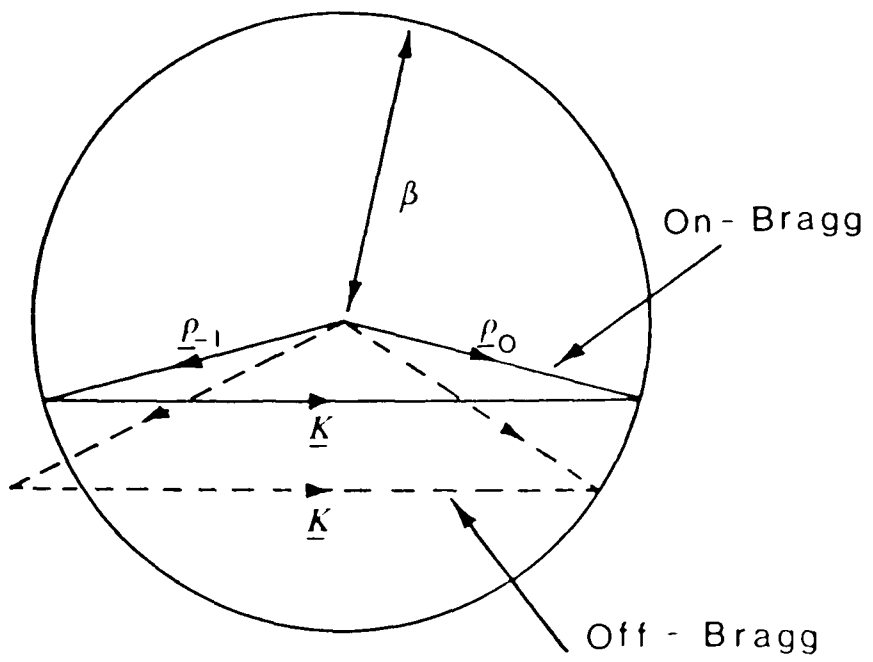

Fig 2.4: Off-Bragg condition assuming '$\underline{K}$-vector closure' for the first order diffracted beam (L = -1).

Two regimes can be distinguished, depending upon whether or not a significant amount of energy is directed into the higher orders. The dimensionless parameter Ω [68], defined as

$$\Omega = \left[\frac{K^2}{2\beta\kappa}\right] \tag{2.18}$$

determines if the mode of diffraction is primarily Bragg (two wave) or Raman-Nath (multi-wave). When $\Omega >> 1$, and $d > \Lambda$, coupling is essentially Bragg and only the incident and first order diffracted beams are important.

Kogelnik [49] modelled Bragg diffraction assuming '$\underline{K}$-vector closure'. He defined R as the amplitude of the transmitted beam $\underline{\rho}$ and S as the amplitude of the diffracted beam $\underline{\sigma}$. Only two coupled-wave equations from equation (2.15) are used

$$\begin{vmatrix} c_R \frac{dR(z)}{dz} \\ c_S \frac{dR(z)}{dz} \end{vmatrix} = \begin{vmatrix} -\alpha & -i\kappa e^{i\Xi} \\ -i\kappa e^{-i\Xi} & -(\alpha + i\gamma) \end{vmatrix} \begin{vmatrix} R(z) \\ S(z) \end{vmatrix} \tag{2.19}$$

where,

$$c_R = \frac{\rho_z}{\beta}, \; c_S = \frac{\sigma_z}{\beta} \tag{2.20}$$

$$\gamma = \gamma_{-1} = \frac{\beta^2 - \sigma^2}{2\beta} \tag{2.21}$$

The parameter κ, proportional to the modulation strength from equation (2.14), determines the rate at which energy is interchanged between the transmitted and diffracted beams on passing through the hologram. The parameter α is the amplitude absorption coefficient. For a perfect grating with spatially constant modulation strength $\left[\kappa(z) = \text{constant}\right]$ and uniform periodicity $\left[\frac{d\Xi(z)}{dz} = 0\right]$, the coupled-wave equations can be analytically solved by finding the eigenvectors and eigenvalues of (2.19) for a given set of boundary conditions. There is the distinction between a transmission and a reflection geometry, depending on whether

the direction cosines of the incident (c_R) and diffracted beam (c_S) are of the same or different signs.

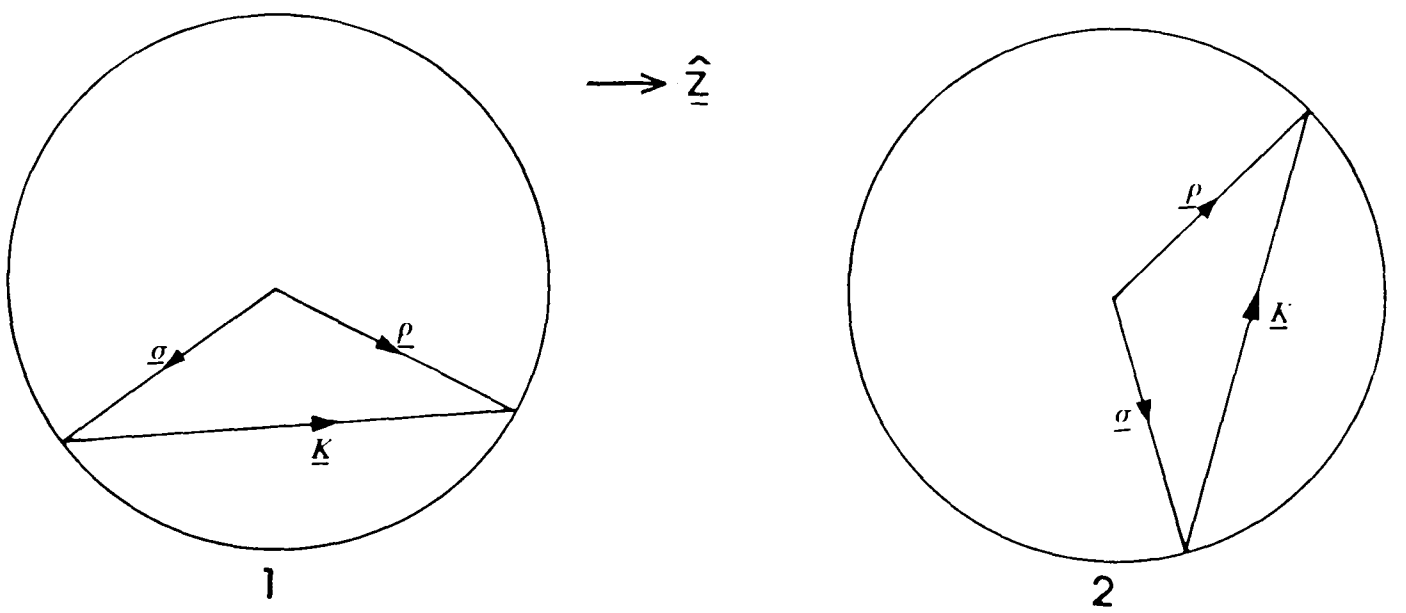

Fig 2.5: (1) - Reflection geometry; (2) - transmission geometry

For a transmission grating the boundary conditions are

$$R(0) = 1,\ S(0) = 0 \qquad (2.22)$$

and for a reflection grating they are

$$R(0) = 1,\ S(d) = 0 \qquad (2.23)$$

The general diffracted beam solution [49] for a transmission hologram is

$$S(0) = -i\left[\frac{c_R}{c_S}\right]^{1/2} e^{\xi} \exp(-\alpha d/c_R)\, \frac{\sin(\nu^2 - \xi^2)^{1/2}}{(1 - \xi^2/\nu^2)^{1/2}} \qquad (2.24)$$

whereas for a reflection hologram it is

$$S(0) = \left[\frac{c_R}{c_S}\right]^{1/2} \frac{\sinh[\nu\cosh(a)]}{\cosh[a + \nu\cosh(a)]} \qquad (2.25)$$

where,

$$\nu = \left[\frac{i\pi\ \tilde{\Delta n}\ d}{\lambda |c_R c_S|^{1/2}}\right] = \left[\frac{i\kappa\ d}{|c_R c_S|^{1/2}}\right] \qquad (2.26)$$

$$\xi = \frac{d}{2}\left[\frac{\alpha}{c_R} - \frac{\alpha}{c_S} - i\,\frac{\gamma}{c_S}\right] \qquad (2.27)$$

$$\sinh(a) = \xi/\nu \qquad (2.28)$$

These equations will be used in the next section to quantify the performance of a filter.

II.4 PREDICTED PROPERTIES OF THE HOLOGRAPHIC FILTER

In this thesis, attention is focussed on a simple holographic filter, which is nevertheless an exceptional example of a volume hologram, both in terms of its physical size (typically mm^3) and in terms of its Bragg mode of diffraction as determined by Q (when $\Lambda = \lambda$ and $\Delta\tilde{n}/\tilde{n} = 10^{-4}$, Q is about 10^4!). In common with other Bragg devices:

1) The filter will have a high wavelength and frequency 'selectivity'.
2) The filter can have a high diffraction efficiency.
3) The filter will have a much larger 'free spectral range' (FSR) than an etalon of the same length.

These aspects will be examined in the following sections.

When a large number of fringe planes contribute to the scattering process ($N_m \approx 10^4$ for this filter), the intensity of the diffracted beam becomes very sensitive to deviations from the Bragg condition. From equation (2.3), if each plane reflects an equal amplitude fraction r, the intensity of the diffracted beam in the kinematic limit will be

$$I = |SS^*| = (N_m r)^2 \, \mathrm{sinc}^2\left[\frac{N_m \zeta}{2}\right] \qquad (2.29)$$

The Bragg condition corresponds to

$$\frac{N_m \zeta_o}{2} = N_m \beta \, \Lambda \cos(\theta_o) = \pi \, m \qquad (2.30)$$

where m is an integer and θ_o is the Bragg angle measured inside the material between the grating wavevector and incident beam. The first minimum of the response occurs, according to equation (2.29), when

$$\frac{N_m \zeta}{2} = N_m\left[\beta + \Delta\beta_{1/2}\right]\Lambda \cos(\theta_o) = \pi(m+1) \qquad (2.31)$$

where $\Delta\beta_{1/2}$ is the wavevector change. The fractional 'selectivity' of

the grating can also be written as

$$\frac{\lambda}{\Delta\lambda_{1/2}} = -\frac{\beta}{\Delta\beta_{1/2}} = \frac{2\,\tilde{n}\,N_m\,\Lambda\cos(\theta_o)}{\lambda} = \frac{2\,\tilde{n}\,d\cos(\theta_o)}{\lambda} \qquad (2.32)$$

where $\Delta\lambda_{1/2}$ is the equivalent wavelength change to reach first minima. Therefore the wavelength selectivity of the grating in the kinematic limit will be proportional to the maximum optical path difference between the interfering beams. Optimising the selectivity, implies normal incidence on the grating fringe planes ($\theta_o \rightarrow 0$) when

$$\frac{\lambda}{\Delta\lambda_{1/2}} = \frac{d}{\Lambda} \qquad (2.33)$$

For a hologram 4 mm long in a crystal of lithium niobate, replayed at a wavelength of 1·152 μm, with refractive index 2·23, there will be about 2×10^4 fringe planes and the smallest resolvable wavelength change is expected to be about 0·5 Å. The angular selectivity can be found from the following equation

$$\cos(\theta) - \cos(\theta_o) = \frac{\lambda}{2\tilde{n}d} \qquad (2.34)$$

where $\theta = \theta_o + \Delta\theta_{1/2}$. When $\theta_o = 0$,

$$\Delta\theta_{1/2} = \left[\frac{\lambda}{\tilde{n}d}\right]^{1/2} \qquad (2.35)$$

or an internal angle of 0·65 degrees. As the Bragg angle θ_o increases the selectivity of the grating rapidly increases. For $\Delta\theta_{1/2} \ll \theta_o$,

$$\Delta\theta_{1/2} = \frac{\lambda}{2\tilde{n}d\sin(\theta_o)} \qquad (2.36)$$

Fig 2.6 plots the external selectivity $\Delta\theta'_{1/2}$ of a filter replayed at 1·152 μm, against the external angle of incidence θ'_o. In practice, this low efficiency value is rarely achieved. The incident beam is usually attenuated, either by diffraction or absorption before propagating across the whole grating, and consequently the full number of reflecting planes are not effectively utilised.

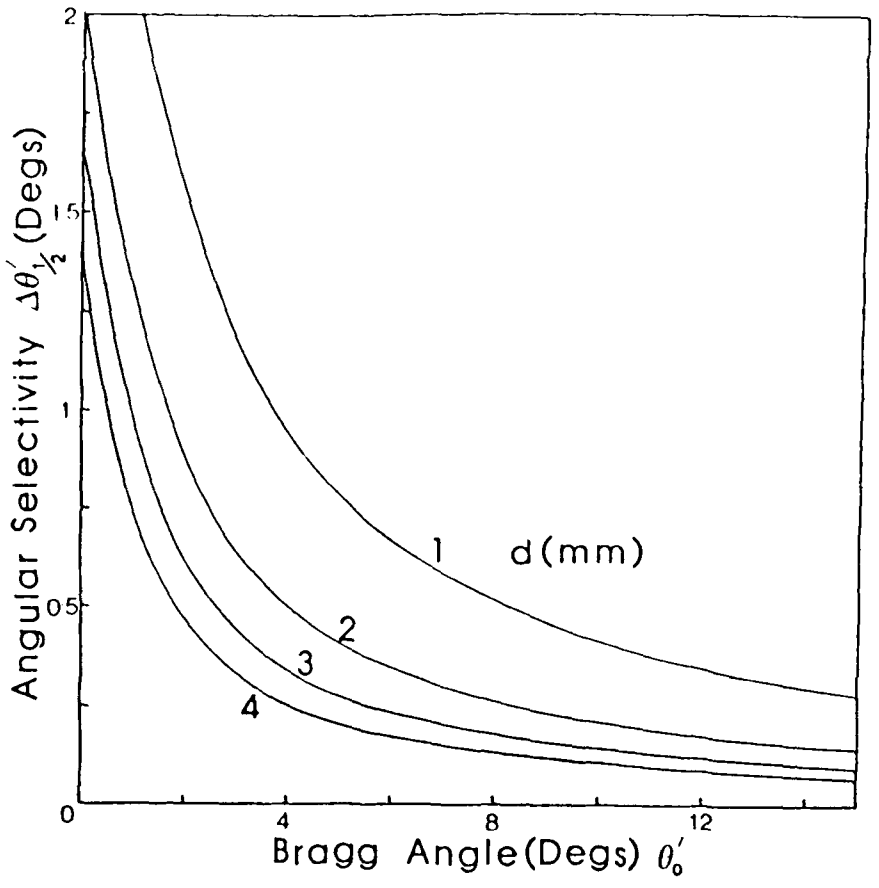

Fig 2.6: Grating selectivity $\Delta\theta'_{1/2}$, as function of the Bragg angle of incidence θ'_o (superscript ' denotes external angle).

Coupled-wave theory provides a simple analytic expression for the grating selectivity in the absence of absorption. From equation (2.25) when $\alpha = 0$, defining $\xi = i\xi_i$, $\sin(a) = \xi_i/\nu$, the diffraction efficiency η becomes

$$\eta = \frac{|C_S|}{C_R} SS^* = \frac{1}{\left[1 + (1 - \xi_i^2/\nu^2)/\sinh^2\left[\nu^2 - \xi_i^2\right]^{1/2}\right]} \qquad (2.37)$$

when $\xi_i = \gamma = 0$, the 'on-Bragg' condition,

$$\eta = \tanh^2(\nu) = \tanh^2\left[\frac{\kappa d}{|C_R C_S|^{1/2}}\right] \qquad (2.38)$$

The efficiency drops to zero when $\xi_i^2 - \nu^2 = \pi^2$. Since ξ_i, proportional to γ, can be written in terms of a wavelength change,

$$\frac{\lambda}{\Delta\lambda_{1/2}} = \frac{d}{\Lambda}\left[1 + \left[\frac{\kappa d}{\pi}\right]^2\right]^{-1/2} \qquad (2.39)$$

Comparing equation (2.39) with equation (2.33), an effective length d_{eff}, shorter than the true length of the grating can be introduced, where

$$d_{eff} = \frac{d}{\left[1 + \left[\frac{\kappa d}{\pi}\right]^2\right]^{1/2}} \qquad (2.40)$$

When κd is large only a grating length of $(1/\kappa)$ contributes to diffraction, whereas when αd is large only a length $(1/\alpha)$ contributes to diffraction. These results set an upper limit on the optimum coupling strength (κd), and also give another reason, apart from insertion loss, why absorption at the replay wavelength should be low.

In the discussion it has been assumed that the grating has constant periodicity (no chirp) and constant modulation strength along its whole length. A selective filter is sensitive to chirp, however, because the selectivity depends upon the uniformity of the grating. Any accumulated change of the grating period Λ across the hologram will increase the bandwidth and reduce the on-Bragg diffraction efficiency because different parts of the grating will diffract different wavelengths with peak efficiency.

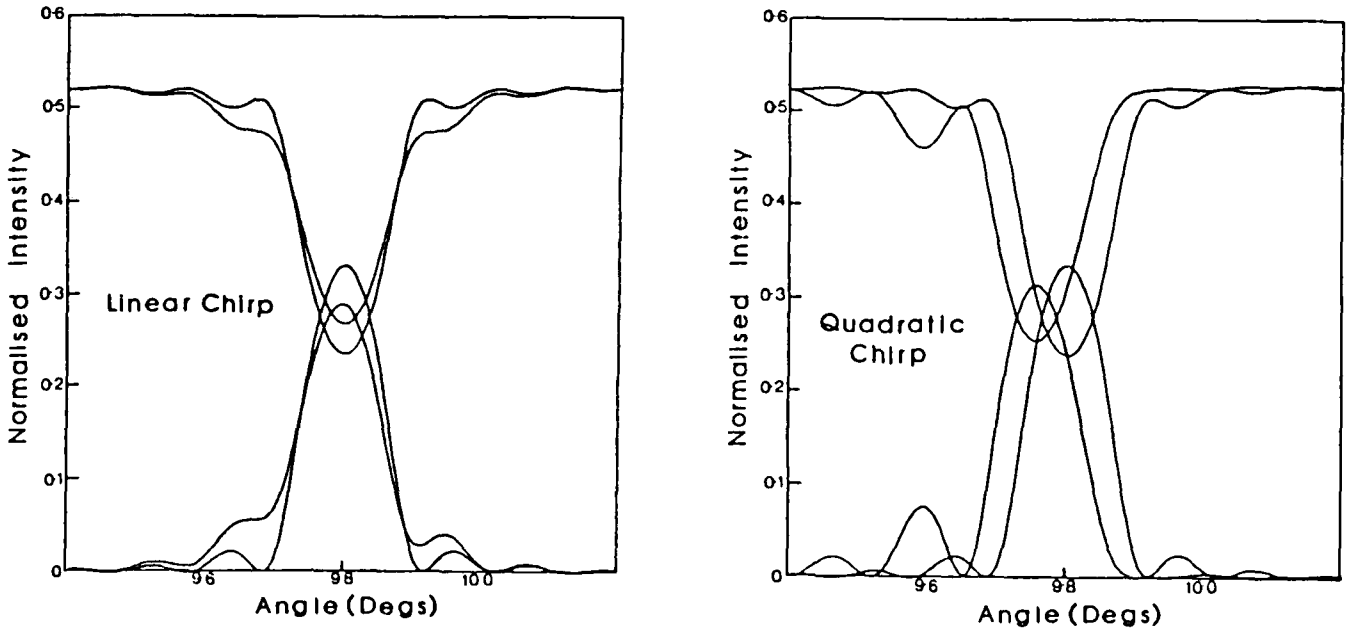

Fig 2.7: Effect of linear and quadratic chirp on the angular response of the grating (θ_o' = 9·8 degrees, d = 4 mm, αd = 0·1, κd = 250) compared with the uniform grating response in both cases

To model these effects a Runge-Kutta algorithm was used to numerically solve [50] equation (2.19). The phase shift $\Xi(z)$ of the grating planes from their periodic positions was expressed as a series expansion

$$\Xi(z) = \Xi_0 + 2\pi F_0 \times \left[\frac{z}{d}\right] + 2\pi F_1 \times \left[\frac{z}{d}\right]^2 + 2\pi F_2 \times \left[\frac{z}{d}\right]^3 \qquad (2.41)$$

where the constant F_1 determines the amount of linear chirp (grating period linear function of distance), and F_2 the amount of quadratic chirp (grating period quadratic function of distance). The effect of both these non-uniformities is shown in Fig 2.7. The difference between linear and quadratic chirp appears in the distribution of the side-lobes.

There is an important tradeoff between the infra-red replay wavelength of the filter (λ_R) and its diffraction efficiency. For a filter of given length (d = constant) the grating wavevector, the density of reflecting fringe planes and the diffracted output must all decrease as λ_R increases. Coupled-wave theory identifies this complication by making the coupling strength $(\kappa d)_R$ defined in equation (2.14) proportional to $1/\lambda_R$. From equation (2.38), to produce an 80% efficient filter,

$$\tanh^2\left[\frac{(\kappa d)_R}{|C_R C_S|^{1/2}}\right] \approx 0.8 \qquad (2.42)$$

or,

$$\left[\frac{(\kappa d)_R}{|C_R C_S|^{1/2}}\right] \approx 1.4 \qquad (2.43)$$

The distinction between a volume grating and an etalon [39] of similar thickness is not their selectivity, which as stated in equation (2.32) should be similar, but their dramatically different FSR. The free spectral range (FSR) is the maximum range of wavelengths that can be unambiguously selected before the next diffraction order or mode overlaps. For an etalon,

$$(\Delta\lambda)_{fsr} = \frac{\lambda_R^2}{2\tilde{n}d} \qquad (2.44)$$

whereas for a perfectly sinusoidal Bragg grating it is infinite!

CHAPTER THREE

PRACTICAL MATERIAL CONSIDERATIONS

III.1 INTRODUCTION

This chapter surveys all the holographic materials suitable for recording infra-red (IR) gratings, setting in context the properties of iron doped lithium niobate. A few general comments about material processing are made, and finally, the basic technique of 'scaling' is introduced which will play an important role in subsequent chapters.

III.2 HOLOGRAPHIC RECORDING MATERIALS

Gelatin based holographic recording materials have historically been popular because of their good optical sensitivity (typically 10 $\mu J/cm^2$ for photographic emulsion) and high resolution (typically 2000 lines/mm). Two different chemical reactions have been investigated. Standard photographic emulsion relies upon the photo-induced conversion of a silver halide [8], usually silver bromide, into metallic colloidal silver, followed by processing to greatly enhance the effect. The other approach is to impregnate the gelatin with dichromated ions (DCG). According to one model [16], microscopic voids are then formed in the material after exposure and rapid dehydration. DCG is an important addition to the list of gelatin recording materials, since it increases the achievable modulation strength from about 1% to 8%, though at the expense of poor holographic reproducibility. The intrinsic sensitivity for both these reactions is restricted to visible wavelengths, unless special measures are taken to extend their range into the infra-red.

Dyes [21] are effective out to about 1 micron, or there is the novel technique in photographic emulsion called the Herschel reversal [40] (named after W. Herschel in 1840), when a photographic latent image is partially erased by exposure to IR radiation. Intense IR radiation [29,64] can also directly create a grating.

Photopolymer materials [91] selectively transform a monomer into a polymer, catalysed by a photo-initiator. These materials are usually dynamic, forming spurious noise gratings on exposure to coherent light, but there is one exception. Chandross [15] recorded in porous glass a latent image consisting of a spatially modulated density of polymerising catalyst. The latent pattern was subsequently developed by exposing the glass, now containing a suitable monomer, to incoherent ultra-violet light, and allowing the polymerisation reaction to proceed. Due to the dimensional stability of the glass, hologram thicknesses of greater than 1 mm can be recorded. The maximum modulation strength so far achieved, however, is only 10^{-4} and the exposure sensitivity is also low (typically $2J/cm^2$). This material is generally sensitive to visible radiation, but IR gratings have been made in an alpha-diketone photopolymer by Brauchie [13] using a two photon effect.

Photorefractive materials [14] rely upon the presence of internal electric fields to form a grating. On receiving sufficient energy from optical radiation, some of the electrons in the crystal are excited from the valence band into the conduction band. Movement of these electrons from regions of high intensity to low intensity creates dipoles and establishes a polarisation field. The linear electro-optic effect converts this electric field pattern into a refractive index variation.

Volume filters in dynamic photorefractives can be designed, either to enhance their real-time recording characteristics, or to be totally passive. An impressive demonstration [7] of a real-time grating was the replacement of a mirror in a dye laser cavity by a reflection grating

recorded in situ. These applications, however, are only possible if a high power laser source is available to initiate the recording process, and will only operate within the recording wavelength band of the material, usually around 0·5 μm, though there is one recently discovered material [48] that is particularly sensitive to IR light.

The photorefractive material, lithium niobate, has a low exposure sensitivity (typically 1J/cm^2 at a wavelength of about 0·5 μm), unless a pulsed laser is used [17], but can store a modulation strength of up to 10^{-3} in the unfixed material. Fixing [85] involves heating the crystal to about 160°C, preferably during recording or soon afterwards. Reflection gratings recorded at visible wavelengths have been briefly investigated by Michalean [63], who exposed a crystal of iron doped lithium niobate to two nearly counterpropagating 0·514 μm or 0·633 μm laser beams, and Yasuhira [103], who used a Lippmann geometry. Like photopolymers, optical sensitivity can be extended into the IR by utilising a two photon effect. For example, Wood [99] recorded gratings in lithium niobate optical waveguides using 1·06 μm radiation.

A bulk acoustic wave filter [71] has been holographically created in lithium niobate, though to be compatible with the frequency range of acoustic transducers, the optical periodicity of the grating corresponded to the mid-IR. The method was successful because the acoustic as well as the optical impedence was modulated. Since lithium niobate is pyroelectric [76], it is possible to record the thermal component of IR radiation. Diffusion, however, will severely limit the maximum spatial frequency response of the material.

Photoresist planar holograms are often used to transfer a grating structure onto other materials. In particular, integrated optical devices with high selectivity (typically a few Å) have been fabricated by lithographically copying a photo-resist mask onto a lithium niobate substrate [1]. Computer generated planar holograms [47] have good design

flexibility and are used at IR wavelengths [36], but fail to achieve the high resolution attainable by holographic methods. Material ablation, caused by the intense heat of high power CO_2 lasers [26], can also directly create a planar modulation pattern.

Comparing the various types of holographic materials, all with their intrinsic limitations, it is evident that only three, ferroelectrics, photopolymers and gelatin varieties, are sufficiently thick to be considered for the fabrication of a highly selective filter.

III.3 MATERIAL THICKNESS

The processing of volume holographic recording materials has an important influence on the uniformity of the created grating. In gelatin based materials, chemicals must be diffused from the surface into the grating during the development stage. A random walk calculation shows that the diffusion distance will be proportional to $(Dt)^{1/2}$, where D is the diffusivity and t the time. Therefore, for a given value of t and D, the overall uniformity of the modulation strength is expected to deteriorate as the prepared thickness of gelatin is increased. Furthermore, because the dimensions of the gelatin can change during processing, phase and amplitude variations in the impedance periodicity can be introduced. These effects have been demonstrated [30] in a DCG layer about 70 μm thick.

Latent photopolymers avoid the problems of diffusion by using a honeycomb matrix, but considerable work is still required to increase the modulation strength of the material. Dynamic materials require no further chemical processing and therefore do not suffer from these problems.

III.4 THE CONCEPT OF SCALING

It is apparent that none of the holographic recording materials easily record holograms directly at IR wavelengths, without loss of resolution, or optical sensitivity. The reduced photon energy necessitates, for emulsion based material a larger grain size, and for ferroelectrics, an intense recording beam. To circumvent some of these material limitations there is the alternative of recording the hologram in the visible, where the material is sensitive, and then using the geometrical properties of the grating to replay the grating at a longer wavelength. Gabor first tried this technique, often described as 'scaling', which has been subsequently developed for the production of IR optical components. Latta, Malin and Owen [55,60,72] specifically investigated IR lenses where aberrations are inevitably introduced, but for a simple filter structure, there are no such fundamental restrictions with fabrication. One weakness still remains due to the change in geometry. Usually any bulk variations of refractive index within the material are compensated by a corresponding change in the spacing between the fringe planes, conserving the important quantity - 'optical path'. If the grating is probed from a different direction, however, this automatic correction is only partially achieved and the hologram becomes more susceptible to optical inhomogeneity.

The main advantage of 'scaling' is the ability to separate the process of recording and replay. For example, absorption during recording is essential for storing the interference pattern via some physical reaction, but absorption at replay, as already shown in chapter two, is not desirable. The insensitivity of the material at longer wavelengths can even be beneficial, as it prevents erasure of the stored grating by the replay beam. Emulsion holograms have to be chemically fixed to overcome the problem of 'print out' but for iron doped lithium

niobate there is the possibility of testing the grating before the fixing operation.

It was decided that the standard recording method in iron doped lithium niobate (exposing with visible light) should be used for this work. Infra-red gratings could then be fabricated by adopting a 'scaling' technique.

CHAPTER FOUR

PROPERTIES OF IRON DOPED LITHIUM NIOBATE

IV.1 INTRODUCTION

This chapter concentrates on the holographic recording material iron doped lithium niobate, which has been used exclusively in this work, and presents a comprehensive survey of its optical storage properties, including recording, fixing and erasure mechanisms. Using this information there is a limited ability to optimise the properties of the crystal for this particular application.

IV.2 DOPING WITH IRON

The performance of lithium niobate as a holographic material was substantially improved following the discovery that dopants could increase the photosensitivity and achievable modulation strength. Different transition-ion impurities were added, since their d-orbital electrons could possibly provide a source of photo-excitable electrons. Iron doping was found to be best [5], introducing donors and traps associated with the Fe^{2+} and Fe^{3+} oxidation states (see Fig 4.1).

When iron-doped material is exposed to wavelengths of light within the visible absorption band (0·45 μm to 0·55 μm), electrons are excited into the conduction band by the conversion of Fe^{2+} ions to Fe^{3+} ions

$$Fe^{2+} \xrightarrow{h\upsilon} Fe^{3+} + e^{-} \qquad (4.1)$$

If the material is exposed to a periodic light pattern, a modulated internal electric field $\underline{E}$ will be established by the movement of

conduction band electrons through the lattice. The field generates a refractive index change $\tilde{\Delta n}$ via the linear electro-optic effect.

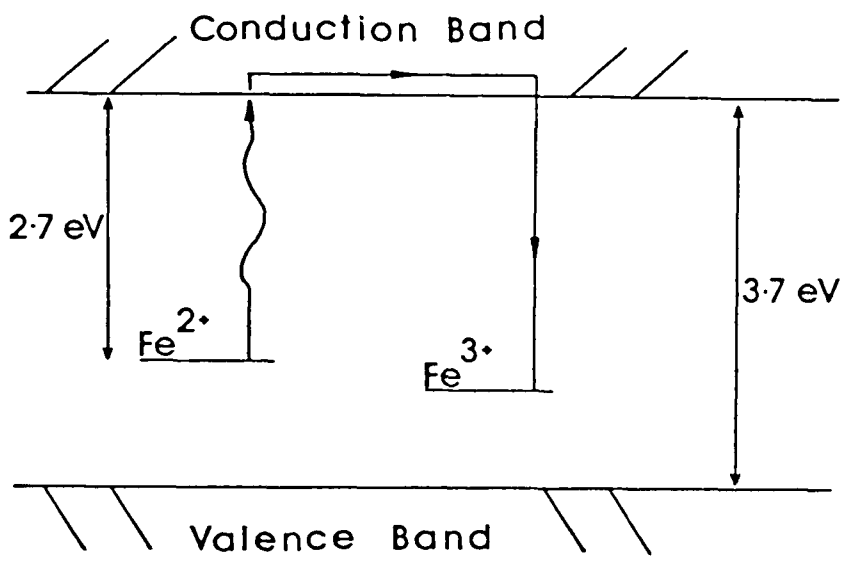

Fig 4.1: Energy level diagram for iron doped lithium niobate [19]

Consider, for example, the phase modulation encountered by a laser beam propagating along the z-axis (or c-axis) of the crystal, when the internal $\underline{E}$ field is along the same direction. From appendix A,

$$\tilde{\Delta\epsilon} = - \frac{r_{113}\ \tilde{\epsilon}_{11}^{2}\ E_k}{\epsilon_o} \qquad (4.2)$$

where r_{113} is the appropriate electro-optic tensor component and $\tilde{\epsilon}$ is the dielectric permittivity at optical frequencies. Expressed in terms of refractive index,

$$\tilde{\Delta n} = - 0{\cdot}5\ \tilde{n}_{ord}^{3}\ r_{113}\ E_k \qquad (4.3)$$

where n_{ord} is the ordinary refractive index of the material. For a 80% efficient infra-red grating, equation (2.43) must be satisfied and therefore,

$$\frac{\pi d \tilde{\Delta n}}{\lambda_R} \approx 1{\cdot}4 \qquad (4.4)$$

where λ_R is the replay wavelength. Combining equations (4.3) and (4.4),

$$|E| = |E_k| \approx \frac{2{\cdot}8\ \lambda_R}{\tilde{n}_{ord}^{3}(\lambda_R)\ r_{113}\ \pi\ d} \qquad (4.5)$$

For a grating replayed at λ_R = 1·15 μm with length d = 2 mm, $\tilde{n}_{ord}(\lambda_R)$ = 2·23 [11], and r_{113} = 8·6 × 10^{-12} mV^{-1} [102],

$\underline{E(min) \approx 50\ kV/cm}$ (4.6)

IV.3 TRANSPORT MECHANISMS

How can internal electric fields of this magnitude be generated inside the crystal? The answer is found by considering the different physical mechanisms of charge transfer within the material. Three mechanisms have been identified: diffusion, and drift due to either an external electric field or an internal photovoltaic current. Their relative importance is determined by the electronic properties of the material and the period of the grating. Electronic diffusion is the easiest to physically describe.

Diffusion of electrons [4] from regions of high light intensity will continue until an opposing diffusion field E_d is sufficiently large to maintain equilibrium. At equilibrium the diffusion current density J_d will equal,

$$J_d = q D \frac{\partial n}{\partial x} = q |\mu_e| n E_d \quad (4.7)$$

where q = |e|, the charge on the electron, n is the electron concentration, μ_e the electron mobility and D the diffusion constant. From the Einstein relation [79] stated below,

$$|\mu_e| = \left[\frac{q}{k_b T}\right] D \quad (4.8)$$

where T is the temperature in degrees Kelvin, and k_b is Boltzmann's constant, E_d can be written as

$$E_d = \left[\frac{k_b T}{q}\right] K = \left[\frac{k_b T}{q}\right] \frac{2\pi}{\Lambda} \quad (4.9)$$

The expression in brackets has a value of about $\frac{1}{40}$ V at room temperature. Therefore, for a typical grating spacing Λ of 0·25 μm, the magnitude of E_d is about 6 kV/cm. It is also independent of doping

level. Diffusion fields are only important in undoped or slightly doped material when other contributions can be neglected.

Photo-excited electrons can also drift from their point of generation, creating a charge distribution out of phase with the interference pattern. The phase shift is determined [66] by the relative values of the characteristic drift length and grating period, Λ.

Glass [37] was the first person to discover an anisotropic, bulk photovoltaic (PV) drift current density, J_p in iron doped lithium niobate. He also proposed that it could be responsible for the drift of carriers along the z-axis (c-axis) of the material during holographic recording. In his experiments he measured the short-circuit photocurrent along the z-axis of different iron doped crystals which were exposed to spectrally filtered incoherent light. The following expression was empirically derived, where κ_p is the photovoltaic constant, α is the absorption coefficient of the material, and I is the light intensity.

$$J_p = \kappa_p \alpha I \qquad (4.10)$$

Although a sensitive ammeter is needed, it is relatively straightforward to measure the short circuit current (typically picoamps). The measurement of voltage is considerably more difficult because the impedance of the voltmeter (in this case an electrometer) and the crystal mount must be significantly higher than the impedance of the crystal itself (typically 10^{12} Ω).

The physical mechanism for the PV effect is still not properly understood [34]. A model, often quoted, is to assume the presence of an asymmetric potential well at the impurity site which causes a statistically preferred direction of electron migration along the c-axis [57,97] of the ferroelectric material. To compare the PV contribution with other fields, a phenomenological PV field E_p is introduced

$$E_p = \frac{J_p}{\sigma_e} = \frac{\kappa_p \alpha I}{q|\mu_e|n_L} \qquad (4.11)$$

where σ_e is the electron conductivity, n_L the density of photo-excited carriers, and $h\nu$ the photon energy. Furthermore, the values for κ_p and $|\mu_e|$ are assumed to be independent of doping level. The magnitude of E_p is typically 10^2 to 10^3 kV/cm for heavily doped material. In comparison, external drift fields E_D [22] up to only 20 kV/cm can be applied before special apparatus is required to prevent electrical breakdown.

The quantity E_p can also be expressed in terms of iron impurity levels. The equation written below is a simple form of the electron continuity equation, where G is the generation rate, R the recombination rate, τ_r is the recombination time to trap conduction band electrons and α is the absorption coefficient.

$$\frac{\partial n_L}{\partial t} = G - R \approx c\ \alpha\ I - \frac{n_L}{\tau_r} \qquad (4.12)$$

In steady state equilibrium,

$$n_L = c\ \alpha\ I\ \tau_r \qquad (4.13)$$

Since $\alpha \propto [Fe^{2+}]$ and $\tau_r \propto 1/[Fe^{3+}]$, where square brackets denote concentration in ions/cm^3,

$$n_L \propto \frac{[Fe^{2+}]}{[Fe^{3+}]} \qquad (4.14)$$

and therefore,

$$E_p \propto [Fe^{3+}] \qquad (4.15)$$

For heavily doped crystals $[Fe^{3+}] > [Fe^{2+}]$, as shown below:

According to Philips and Staebler [74] the value of $[Fe^{2+}]$ can be deduced from the visible attenuation of the crystal. Since a Fe^{2+} concentration of 0·1 mol% (or $1{\cdot}89 \times 10^{19}$ Fe^{2+} ions/cm^3) corresponds to an absorption coefficient α of 150 cm^{-1} ($\underline{\tilde{E}}$ field perpendicular to c-axis, λ of 0·45 μm)

$$[Fe^{2+}] = 1{\cdot}26 \times 10^{17}\ \alpha(cm^{-1}) \qquad (4.16)$$

From the spectral absorption curve for crystal I shown in Fig 4.2, an approximate figure for the contribution due to iron impurities

rather than band gap excitation is (4 ± 0·5) cm^{-1}, or $[Fe^{2+}] \approx 5 \times 10^{17}$ ions/cm^3. The total iron content determined from atomic absorption spectroscopy (see appendix E) was (0·04 ± 0·005) mol%, or $[Fe] \approx 7{\cdot}6 \times 10^{18}$ ions/cm^3.

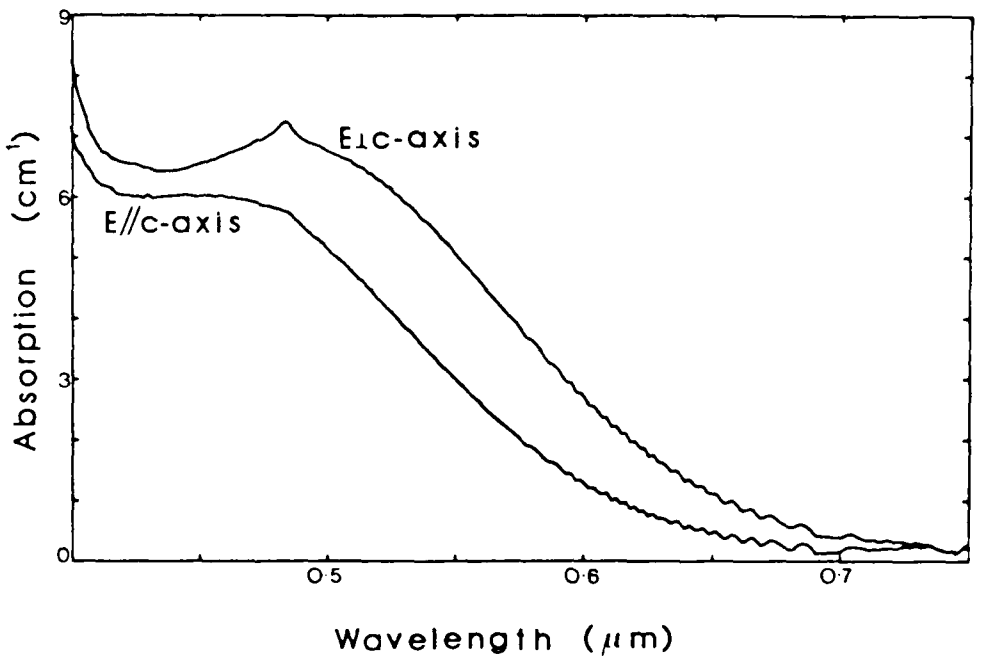

Fig 4.2: Visible absorption spectra for crystal I for both polarisation states

Under these conditions, the magnitude of E_p will be roughly proportional to the total iron content [Fe], or $[Fe^{2+} + Fe^{3+}]$. Confirmation of this functional relationship has been given by Kurtz [54], who experimentally determined the maximum possible modulation strength $\tilde{\Delta n}$ as a function of [Fe]. His results showed a linear dependence on [Fe] up to about 0·1 mol%, followed by saturation and a gradual decline for higher concentrations. The deviation from the linear model, for doping levels greater than 0·1 mol%, can probably be attributed to the disruption of the lattice by the high concentration of impurity ions (one ion in ten along any crystallographic axis, for a 0·1 mol% doping level).

IV.4 EXPERIMENTAL VERIFICATION OF κ_p

To check the quoted value of κ_p ($3{\cdot}0 \times 10^{-9}$ Acm/W [37] at a wavelength of 0·5145 μm) an expanded laser beam was used as the light source, since a sufficiently intense arc lamp was not available. As a result, spurious scatter gratings were formed in the crystal due to the coherent nature of the source (also see section IV.7). The total attenuation inside the crystal (dimensions 1×1×1 cm^3 along crystallographic axes) was sufficiently large to make the reasonable approximation, that all the incident light apart from reflection losses would be completely absorbed. Electrical interference was reduced by placing a metal box (Faraday cage) over the crystal and transient pyroelectric effects [76] were eliminated by waiting for a constant reading. Figure 4.3 below shows the time development of the current for various light intensities.

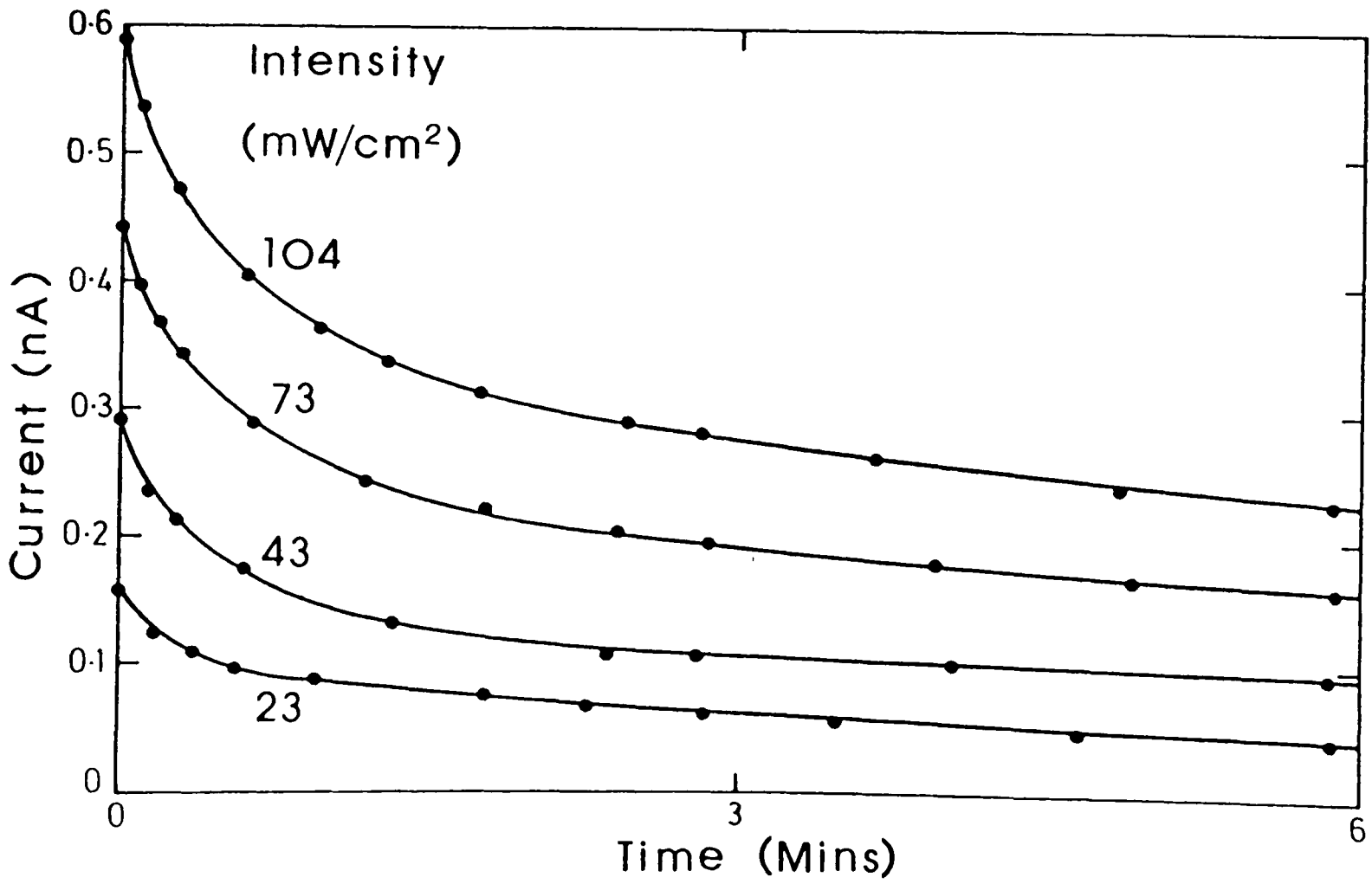

Fig 4.3: Current along c-axis for different light intensities.
Temporal variation can be attributed to a RC time constant effect

A straight line fit of the constant current readings was produced, as shown in Fig 4.4 below. The value for κ_p calculated from this experiment was within a factor of two of the quoted value.

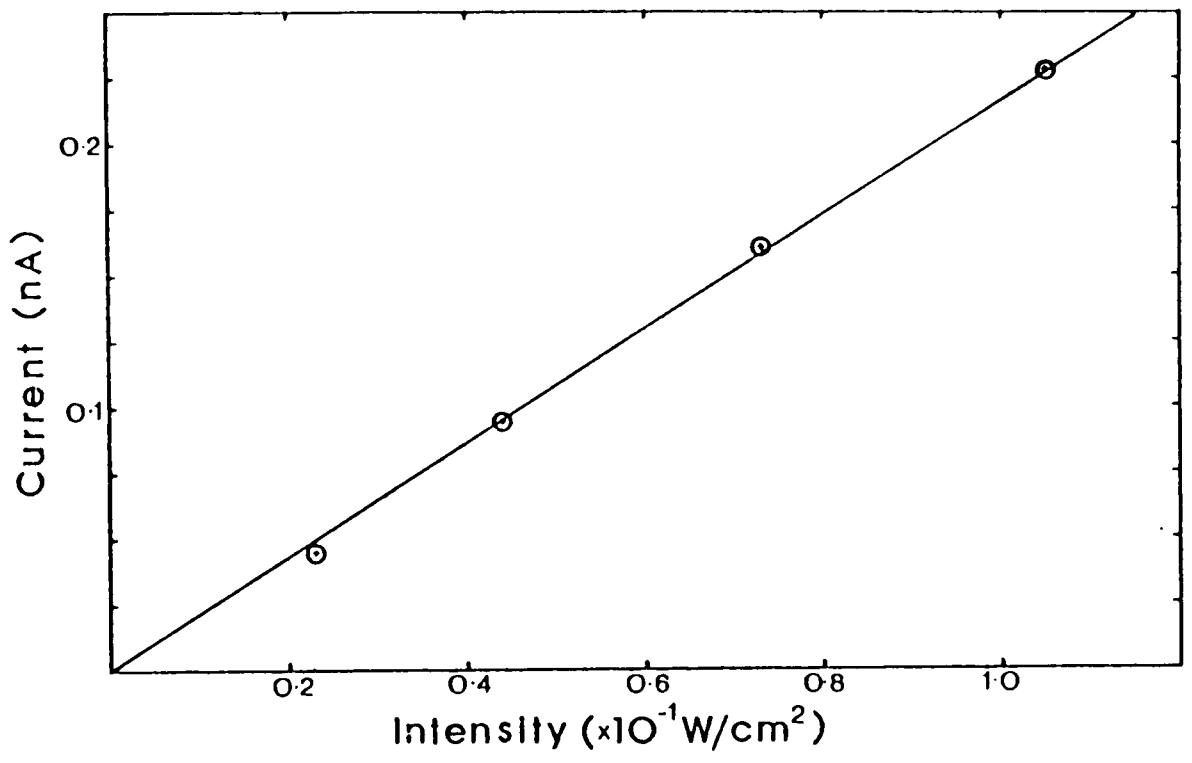

Fig 4.4: Straight line fit of constant current readings

IV.5 SATURATION MECHANISMS

If drift or diffusion fields are sufficiently large, transfer of electrons from donors to traps can continue until either all the traps are filled, or all the donors are ionised - whichever occurs first. In heavily doped material, when $[Fe^{2+}] < [Fe^{3+}]$, the limiting factor will be the available concentration of ionised donors N_D^+. This saturation mechanism sets a limit on the maximum achievable value of E. Consider the internal electric field E generated due to the accumulating periodic charge variation, $N_D^+ \cos(Kz)$ inside the crystal. Neglecting other electric field contributions, the value of E is then found by solving Poisson's one dimensional equation

$$\epsilon \frac{dE}{dz} = q\, N_D^+ \cos(Kz) \qquad (4.17)$$

where ϵ is the dielectric permittivity at static rather than optical frequencies.

Therefore,

$$|E| \leq E_t \qquad (4.18)$$

where,

$$E_t = \frac{q\, N_D^+}{K\, \epsilon} = \frac{q\, N_D^+\, \Lambda}{2\pi\, \epsilon} \qquad (4.19)$$

If all the donors can be ionised N_D^+ will reach the value N_D or $[Fe^{2+}]$. Inserting into equation (4.19), $\Lambda = \frac{\lambda_R}{2\tilde{n}_{ord}}$, $\tilde{n}_{ord} = 2{\cdot}23$, $\epsilon = 30\epsilon_o$ [87], the free space permittivity $\epsilon_o = 8{\cdot}854 \times 10^{-12}$ Fm^{-1}, $q = 1{\cdot}6 \times 10^{-19}$ C implies

$$E_t(max) = 2{\cdot}5 \times 10^{-11}\ [Fe^{2+}] \qquad (4.20)$$

By way of example, for crystal I,

$$E \leq E_t(max) \approx 125\ kV/cm \qquad (4.21)$$

The finite concentration of impurity atoms will also set an upper limit on the maximum spatial frequency response of the recording material. As before, the concentration of Fe^{2+} ions will be the limiting factor. However, since the average separation between Fe^{2+} sites is only

$$(5 \times 10^{23})^{-1/3} \approx 0{\cdot}01\ \mu m \qquad (4.22)$$

whereas a typical value for Λ is $0{\cdot}25\ \mu m$ (at $\lambda_R = 1{\cdot}152\ \mu m$), this effect can be neglected.

IV.6 NON-PERIODIC CHANGES IN REFRACTIVE INDEX

So far the refractive change, due to the average or DC component of the light interference pattern, has been neglected. It is nevertheless an important contribution, generating a change in index comparable with the modulated component. Furthermore, the DC contribution is likely to vary across the crystal [67,23] because the overlapping beams will generally have a non-uniform intensity cross-section.

Short-circuiting the crystal, by evaporating aluminium electrodes onto the c-axis faces of the crystal only ensures that the integrated electric field distribution over the whole crystal is zero. In any case, this 'closed-circuit' condition is usually a good approximation [66], since the surface resistance of the crystal is about 100 times less than the bulk value.

IV.7 SCATTERING

A serious limitation with iron doped lithium niobate is the progressive increase of diffuse scattering [41] during exposure due to the presence of parasitic noise gratings. The effects are particularly harmful in dynamic materials where the process, once begun, will escalate until the main interfering beams are severely depleted. Good optical quality of the crystal is essential, if the growth of the grating is not to be significantly curtailed by dynamic scattering.

A filter produced by a 'scaling' geometry will be less susceptible to the deleterious effect of noise gratings formed at recording. Noise gratings are associated with the coupling between a strong beam and scattered wavefronts inside the material. If the strong beam is incident on the crystal at a different angle, however, these noise gratings will be 'off-Bragg'.

Rayleigh scattering from the crystal surfaces ($\alpha\ 1/\lambda^4$) will also be less at longer wavelengths.

IV.8 ERASURE

The unfixed grating will be erased when it is heated or exposed to a uniform light beam. In both cases, electrons are uniformly excited out of their traps and redistribute back to a state of equilibrium. The

photon energy of the incident light must be sufficient to photo-ionize the electrons out of their traps (at least 2·35 eV according to Wood [100]). Optical erasure can be achieved by illuminating the crystal with a Xenon arc lamp.

The time constant for the process is the electronic relaxation time, τ_e, with the internal electric field strength E decaying as

$$E(t) = E(0) \exp\left[\frac{-t}{\tau_e}\right] \qquad (4.23)$$

where,

$$\tau_e = \left[\frac{\epsilon}{\sigma_e}\right] = \left[\frac{\epsilon}{q|\mu_e|n}\right] \qquad (4.24)$$

Generally,

$$n = n_L \text{ (light generation)} + n_D \text{ (dark generation)} \qquad (4.25)$$

but, on exposure to light when $n_L >> n_D$,

$$\tau_e \propto \frac{1}{n_L} \propto \frac{[Fe^{3+}]}{[Fe^{2+}]} \propto \frac{[Fe - Fe^{2+}]}{[Fe^{2+}]} \qquad (4.26)$$

These results imply:

i) Unfixed, heavily doped materials will be less sensitive to optical erasure than lightly doped materials.

ii) In heavily doped crystals, when $[Fe] \approx [Fe^{3+}]$, the time constant for erasure will be inversely proportional to the amount of visible absorption in the crystal (or $[Fe^{2+}]$).

IV.9 FIXING

The principle of fixing is to establish a semi-permanent periodic electric field variation within the crystal. In practice, it is usually achieved by heating the crystal [85] to about 160°C, either during recording or soon afterwards. At these elevated temperatures an internal ionic charge distribution, identified as H^+ ions [98], becomes mobile, whilst the electronic distribution remains effectively stationary. This

is possible, because the activation energy for H^+ ions is lower than the activation energy for trapped electrons. The internal electric fields will then relax back towards zero and an ionic density variation will be created that almost screens the original electronic pattern (ionic diffusion fields prevent exact cancellation [84]). At room temperatures, the Boltzmann dependence of excitation rate implies that the ionic charge pattern will be immobile for typically 10^5 years.

In heavily doped materials, the high photovoltaic fields can be used to disturb the equilibrium charge balance of the fixed grating. If the crystal is uniformly illuminated with visible light, the electrons are ionized, the modulation strength of the electronic pattern is reduced and the underlying ionic variation partially reappears. In the dark, however, these electrons will slowly relax back to their former positions with a time constant τ_e (or about a month for the crystals in this project). Furthermore, the infra-red replay light supplies insufficient photon energy to ionise the electrons out of their donor traps!

If thermal fixing is not undertaken, there is the alternative of increasing τ_e by cooling the crystal (exploiting the Boltzmann dependence again), or reducing the photoconductivity of the material.

IV.10 SUMMARY

There are two stages at which the grating can be tested, namely before and after fixing. The planned experiments are mainly involved with measuring the diffraction efficiency of the unfixed grating. Under these circumstances the important material characteristics to optimise are the crystal optical quality, the unfixed storage time and the exposure sensitivity. A high modulation strength is advantageous, since efficiency will be lost during the fixing process.

The advantage of heavily doped material is the long unfixed storage time (typically weeks) and high modulation strength (due to E_p), assuming there is sufficient $[Fe^{2+}]$ or visible absorption to prevent premature saturation (see section IV.5). To reduce the exposure time the exposure sensitivity of the material must be increased. From equation (4.12), the generation rate G, the absorption coefficient α and hence $[Fe^{2+}]$ must therefore be high.

CHAPTER FIVE

DYNAMIC THEORIES

V.1 INTRODUCTION

Disussed in this chapter are the complex theories describing the recording of a grating in iron doped lithium niobate. The probability of obtaining good agreement between theory and experiment is low because some of the important parameters, like optical inhomogeneity, scattering, and the history of the material, cannot be easily included, whereas others, like internal fields E_t or E_p, are difficult to experimentally measure. Therefore, the aim of this analysis will be to simplify the theoretical expressions and extract general trends.

In a dynamic recording material the processes of recording and replay are occurring simultaneously. Consequently, there is an interaction between the fringe pattern of optical intensity and the generated refractive index grating. As shown later, the position of the grating can be shifted relative to the position of the interference pattern due to the competing effects of drift and diffusion currents inside the crystal.

Two different theories, Kukhtarev's et al. [52] and Staebler's et al. [2] will be examined. Kukhtarev's et al. model is a general self-consistent formulation, deriving both time-dependent and time-independent effects from fundamental material equations. In this chapter, however, only the steady state condition will be considered. Staebler's model, will be used to explain time-dependent effects. Despite its many assumptions, the model includes all the essential material equations in a

form that could be readily solved to give a physically significant result.

V.2 RECORDING GEOMETRY

It has already been explained in chapter three that a 'scaling geometry' will be used to form the IR filter, because the photorefractive effect in iron doped lithium niobate peaks in the visible and is very weak in the infra-red. Additionally, as noted in chapter four, the photovoltaic contribution is optimised when the grating $\underline{K}$-vector is parallel to the c-axis of the material. The filter will therefore be recorded and replayed in the following way

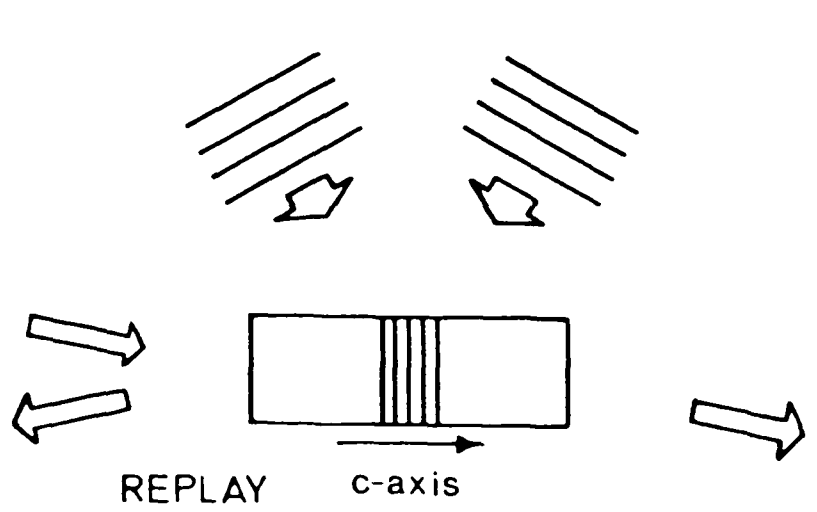

Fig 5.1 Scaling geometry

Two collimated recording beams, interangle separation $2\psi'_G$ (where superscript ' denotes external angle, and subscript G denotes recording wavelength) overlap inside the crystal, as shown in Fig 5.2, to form the interference pattern. The electric field amplitudes of the two beams are $\tilde{E}_{+1}$, $\tilde{E}_{-1}$, with corresponding intensities I_{+1}, I_{-1}, polarisation unit vectors $\hat{\underline{e}}_{+1}$, $\hat{\underline{e}}_{-1}$ and wavevector directions $\hat{\underline{k}}_{+1}$, $\hat{\underline{k}}_{-1}$. The interfering beams can therefore be written as:

$$\underset{+1}{\tilde{\mathbf{E}}} = \tilde{E}_{+1}\,\underset{+1}{\hat{\mathbf{e}}}\,\exp\left[-i\,(\underset{+1}{\mathbf{k}}\cdot\underset{}{\mathbf{r}} + \omega t)\right] \tag{5.1}$$

$$\underset{-1}{\tilde{\mathbf{E}}} = \tilde{E}_{-1}\,\underset{-1}{\hat{\mathbf{e}}}\,\exp\left[-i\,(\underset{-1}{\mathbf{k}}\cdot\underset{}{\mathbf{r}} + \omega t)\right] \tag{5.2}$$

where $\underline{r}$ is the direction of propagation, ω is the angular frequency, and $\tilde{E}_{+1} = |\underset{+1}{\tilde{\mathbf{E}}}|$. The interference pattern has an average component I_0 and modulated component I_1, where

$$I_0 = \tilde{E}_{+1}\tilde{E}^{*}_{+1} + \tilde{E}_{-1}\tilde{E}^{*}_{-1} \tag{5.3}$$

$$I_1 = \tilde{E}_{+1}\tilde{E}^{*}_{-1}(\underset{+1}{\hat{\mathbf{e}}}\cdot\underset{-1}{\hat{\mathbf{e}}})\exp(-iKz) + \tilde{E}_{-1}\tilde{E}^{*}_{+1}(\underset{-1}{\hat{\mathbf{e}}}\cdot\underset{+1}{\hat{\mathbf{e}}})\exp(iKz) \tag{5.4}$$

$$(\underset{+1}{\hat{\mathbf{e}}}\cdot\underset{+1}{\hat{\mathbf{k}}}) = (\underset{-1}{\hat{\mathbf{e}}}\cdot\underset{-1}{\hat{\mathbf{k}}}) = 0 \tag{5.5}$$

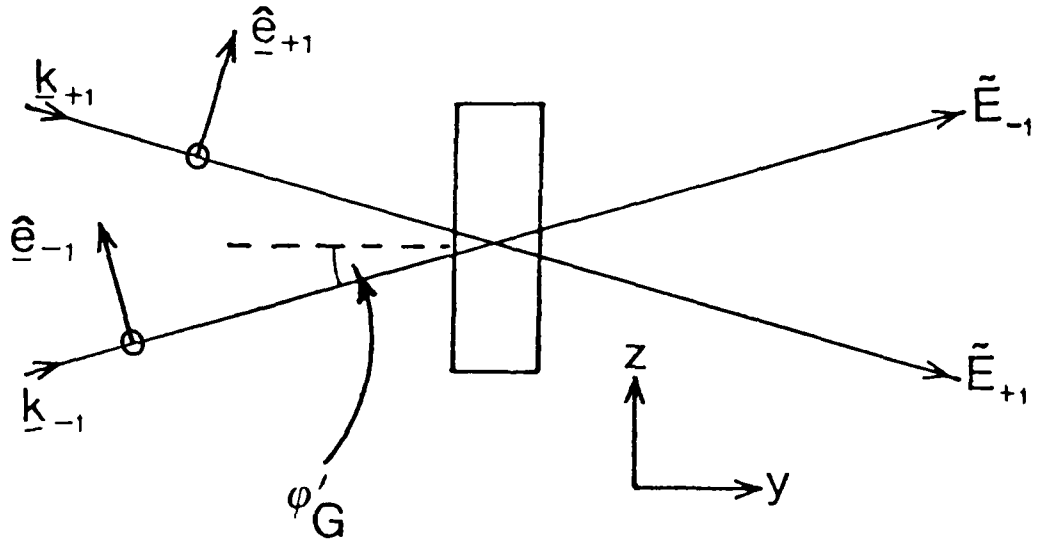

Fig 5.2: Recording geometry in detail

V.3 KUKHTAREV'S MODEL

The first stage in the development of this model is to relate the light interference pattern present during recording to the refractive index change inside the material. It involves solving the fundamental set of material equations given below.

$$\frac{\partial n}{\partial t} = \frac{\partial N_D^{+}}{\partial t} - \frac{1}{q}\,\nabla.\underline{J} \tag{5.6}$$

$$\frac{\partial N_D^{+}}{\partial t} = G - R = f(N_D - N_D^{+}) - \gamma_r\, n\, N_D^{+} \tag{5.7}$$

$$f = (sI + \beta_t) \tag{5.8}$$

$$J_d = q\,|\mu_e|\,n\,E \tag{5.9}$$

$$J_D = |\mu_e|\,k_b T\,\nabla.\underline{n} \tag{5.10}$$

$$J_p = p\,(N_D - N_D^+)\,I \tag{5.11}$$

$$J = J_d + J_D + J_P \tag{5.12}$$

$$\rho_{sc} = -\,q\,(n + N_A^- - N_D^+) \tag{5.13}$$

$$\nabla.\underline{D} = \nabla.(\epsilon\,\underline{E}) = \epsilon\,\nabla.\underline{E} = \rho_{sc} \tag{5.14}$$

(where $q = |e|$)

These equations describe the ionization of electron donors N_D (identified with Fe^{2+} ions) into their N_D^+ state, so that electrons can be contributed to the free carrier density n. The photo-excited electrons move through the crystal producing a current J before relaxing back into the valence band.

Examining each expression in detail, equation (5.6) is the standard continuity relationship applied to conduction electrons. Equation (5.7) states that the change in the concentration of ionised donors N_D^+ must equal the difference between the generation rate G and recombination rate R $\left[= \gamma_r n\,N_D^+,\ \text{when } n << N_D^+\right]$ of free carrier electrons. There are two contributions to G, as stated in equation (5.8), namely thermal ($\alpha\ \beta_t$) and optical (α s) excitation,

Equations (5.9) through to (5.12) introduce the transport equations for the conduction electrons, where J_D is the external drift current density, J_p is the photovoltaic current density ($\alpha\ \alpha I$ from chapter four), and J_d is the diffusion current density. Equation (5.13) is a statement of charge conservation, where N_A^- is the density of acceptor ions, which are assumed to be totally ionised and ρ_{sc} is the local space charge density. Poisson's relation is expressed in equation (5.14). The spatial variation of the permittivity ϵ at DC frequencies is usually neglected.

The acceptor levels N_A^- are assumed to be completely filled by electrons and not involved in the formation of the grating. Their only role is to maintain charge neutrality and in so doing, set the balance between the concentration of donors and traps. It is assumed that the mobility of holes $|\mu_h|$ is much smaller than the mobility of the photo-excited electrons $|\mu_e|$. Consequently the movement of holes can be neglected. In common with all other standard theories, dynamic scattering caused by material inhomogeneity is neglected.

Consider the steady state condition when all temporal variations have reached equilibrium ($\frac{\partial}{\partial t} = 0$). For a 'small signal' approximation the various terms introduced above can be expanded as a linear series. In Solymar's et al. [82] treatment only two terms in the expansion are considered, where '0' denotes the average or DC term, and '1' denotes the fundamental Fourier component with the same period as the light interference pattern. Each of the terms are complex, to allow for the possibility of phase shift. In one dimension,

$$N_D^+(z) = N_D^+[0] + N_D^+[1]\, e^{iKz} \tag{5.15}$$

$$n(z) = n[0] + n[1]\, e^{iKz} \tag{5.16}$$

$$I(z) = I[0] + I[1]\, e^{iKz} \tag{5.17}$$

$$J(z) = J[0] + J[1]\, e^{iKz} \tag{5.18}$$

$$E(z) = E[0] + E[1]\, e^{iKz} \tag{5.19}$$

$$f(z) = f[0] + f[1]\, e^{iKz} \tag{5.20}$$

Equation (5.7) becomes:

$$0 = \left[f[0] + f[1]e^{iKz}\right]N_D - \left[f[0] + f[1]e^{iKz}\right]\left[N_D^+[0] + N_D^+[1]e^{iKz}\right] - \gamma_r\left[n[0] + n[1]e^{iKz}\right]\left[N_D^+[0] + N_D^+[1]e^{iKz}\right] \tag{5.21}$$

Equation (5.12) becomes

$$J[0] + J[1]e^{iKz} = q|\mu_e|\left[n[0] + n[1]e^{iKz}\right]\left[E[0] + E[1]e^{iKz}\right] - i|\mu_e|k_bT\,K\,n[1]e^{iKz} + pN_D\left[I[0] + I[1]e^{iKz}\right]$$

$$- p\left[N_D^+[0] + N_D^+[1]e^{iKz}\right]\left[I[0] + I[1]e^{iKz}\right] \qquad (5.22)$$

Equation (5.14) becomes

$$iK\,E[0] = -\frac{q}{\epsilon}\left[n[0] + n[1]e^{iKz} + N_A^- - N_D^+[0] - N_D^+[1]e^{iKz}\right] \qquad (5.23)$$

The following expressions for electric field are then introduced.

$$E_e = \frac{q\,n[0]}{K\,\epsilon},\quad E_t = \frac{q\,N_D^+[0]}{K\,\epsilon},\quad E_d = \frac{k_b T\,K}{q},$$
$$E_p = \frac{p\,N_D I[0]}{q|\mu_e|n[0]},\quad b = \frac{N_D^+[0]}{N_D},\quad E_D = \frac{J[0]}{q|\mu_e|n[0]} \qquad (5.24)$$

If constant and first order modulated components are separately equated, but higher order cross-terms are neglected, the modulated component of the space charge field E[1] can be expressed as,

$$E[1] = (A + i\,B)\left[\frac{I[1]}{I[0]}\right] \qquad (5.25)$$

where A and iB are the real and imaginary parts of the electric field. Equation (5.25) predicts that the electric field modulation inside the crystal and hence the grating pattern will be shifted relative to the interference pattern by a phase angle Ξ_g, where $\Xi_g = \tan^{-1}\left[\frac{B}{A}\right]$. Making the approximations $E_e = 0$ (assuming n is small), $b = 0$ ($N_D^+ << N_D$), $E_0 = 0$ (no externally applied field),

$$E[1] = \frac{E_p E_t - i\,E_d E_t}{(E_d + E_t)}\left[\frac{I[1]}{I[0]}\right] \qquad (5.26)$$

According to equation (5.26), if $E_t >> E_d$ then

$$|E[1]| = \left[E_p^2 + E_d^2\right]^{1/2}\left[\frac{I[1]}{I[0]}\right] \qquad (5.27)$$

$$\Xi_g = \tan^{-1}\left[-\frac{E_d}{E_p}\right] \qquad (5.28)$$

Rewriting equation (5.25) using equations (5.3) and (5.4), $|E[1]| =$

$$(A^2 + B^2)^{1/2}(\underline{\hat{e}}_{+1} \cdot \underline{\hat{e}}_{-1})\frac{\left[\tilde{E}_{+1}\tilde{E}^*_{-1}\exp -i(Kz-\Xi_g) + \tilde{E}^*_{+1}\tilde{E}_{-1}\exp i(Kz-\Xi_g)\right]}{I_0} \qquad (5.29)$$

The second stage in the development of this model is to determine the coupling between the grating and the recording beams. The coupled wave approach given in chapter two will be adopted. In this case,

however, Maxwell's vector wave equation rather than scalar equation must be solved.

$$\nabla \times \nabla \times \tilde{\underline{E}} + k_H^2 \tilde{\underline{E}} = 0 \tag{5.30}$$

where,

$$\tilde{\underline{E}} = \tilde{\underline{E}}_{+1} + \tilde{\underline{E}}_{-1} \tag{5.31}$$

$$k_H^2 \tilde{\underline{E}}_{+1} = \frac{\omega^2}{c^2}\Big[(\hat{\underline{x}}.\hat{\underline{e}}_{+1})(\tilde{\epsilon}_{11} + \Delta\tilde{\epsilon}_{11})\tilde{E}_{+1}\hat{\underline{x}} + (\hat{\underline{y}}.\hat{\underline{e}}_{+1})(\tilde{\epsilon}_{22} + \Delta\tilde{\epsilon}_{22})\tilde{E}_{+1}\hat{\underline{y}} + (\hat{\underline{z}}.\hat{\underline{e}}_{+1})(\tilde{\epsilon}_{33} + \Delta\tilde{\epsilon}_{33})\tilde{E}_{+1}\hat{\underline{z}}\Big] \exp(-i\,\underline{k}_{+1} \cdot \underline{r}) \tag{5.32}$$

$\tilde{\epsilon}$ is the permittivity tensor at optical frequencies, $\Delta\tilde{\epsilon}$ is the modulated term, $\hat{\underline{x}}$, $\hat{\underline{y}}$, $\hat{\underline{z}}$ are the crystallographic axes, k_H is the propagation constant in the hologram, ω the angular frequency and c the velocity of light in free space. From appendix A, for an internal field along the z-axis,

$$\Delta\tilde{\epsilon}_{ii} = -\frac{\tilde{\epsilon}_{ii}^{\,2}\, r_{iik}\, E_k[1]}{\epsilon_o} \tag{5.33}$$

where r is the electro-optic tensor, ϵ_o is the permittivity of free space and E_k is an internal electric field along the $\hat{\underline{z}}$ axis. Since,

$$|\underline{k}_{+1}| = |\underline{k}_{-1}| = \beta_G, \tag{5.34}$$

$$\nabla \times \left[\tilde{E}_{+1}\,\hat{\underline{e}}_{+1}\exp(-i\,\underline{k}_{+1} \cdot \underline{r})\right] = \exp(-i\,\underline{k}_{+1} \cdot \underline{r})\left[\frac{\partial \tilde{E}_{+1}}{\partial y}(\hat{\underline{y}} \times \hat{\underline{e}}_{+1}) + i\,\beta_G\,\tilde{E}_{+1}(\hat{\underline{e}}_{+1} \times \hat{\underline{k}}_{+1})\right] \tag{5.35}$$

Neglecting second derivatives as in chapter two, and using the vector identity $(\underline{a} \times \underline{b}) \times \underline{c} = (\underline{c}.\underline{a})\underline{b} - (\underline{c}.\underline{b})\underline{a}$

$$\nabla \times \nabla \times \left[\tilde{E}_{+1}\,\hat{\underline{e}}_{+1}\exp(-i\,\underline{k}_{+1} \cdot \underline{r})\right] = \exp(-i\,\underline{k}_{+1} \cdot \underline{r})\left[\hat{\underline{e}}_{+1}\left[2i\beta_G\frac{\partial \tilde{E}_{+1}}{\partial y}(\hat{\underline{k}}_{+1} \cdot \hat{\underline{y}}) + \beta_G^2\,\tilde{E}_{+1}\right] + \hat{\underline{k}}_{+1}\left[-i\beta_G\frac{\partial \tilde{E}_{+1}}{\partial y}(\hat{\underline{e}}_{+1} \cdot \hat{\underline{y}})\right]\right] \tag{5.36}$$

There is a similar expression for $\tilde{\underline{E}}_{-1}$. If both of them are inserted into the wave equation, and equation (5.32) is also expressed in

terms of components along $\hat{\underline{k}}$ and $\hat{\underline{e}}$, the following pair of coupled differential equations [44] are eventually produced,

$$\frac{d\tilde{E}_{+1}}{dy} + i\,|\Gamma_{\Pi}|\exp(+i\,\Xi_g)\,\frac{|\tilde{E}_{-1}|^2\,\tilde{E}_{+1}}{|\tilde{E}_{+1}|^2 + |\tilde{E}_{-1}|^2} = 0 \qquad (5.37)$$

$$\frac{d\tilde{E}_{-1}}{dy} - i\,|\Gamma_{\Pi}|\exp(-i\,\Xi_g)\,\frac{|\tilde{E}_{+1}|^2\,\tilde{E}_{-1}}{|\tilde{E}_{+1}|^2 + |\tilde{E}_{-1}|^2} = 0 \qquad (5.38)$$

where Γ_{Π} is the dynamic coupling constant for $\hat{\underline{e}}_{+1}$, $\hat{\underline{e}}_{-1}$ perpendicular to the plane of incidence and Γ_{σ} is the dynamic coupling constant for $\hat{\underline{e}}_{+1}$, $\hat{\underline{e}}_{-1}$ in the plane of incidence.

$$|\Gamma_{\Pi}| = F\,\tilde{\epsilon}_{11}^{2}\,r_{113} \qquad (5.39)$$

$$|\Gamma_{\sigma}| = F\cos(2\psi_G)\left[-\tilde{\epsilon}_{22}^{2}\,r_{223}\sin^2(\psi_G) + \tilde{\epsilon}_{33}^{2}\,r_{333}\cos^2(\psi_G)\right] \qquad (5.40)$$

$$F = \frac{\omega^2}{c^2 2\beta_G\cos(\psi_G)}\left[A^2 + B^2\right]^{1/2} \approx \frac{\omega^2\,E_p}{c^2 2\beta_G\cos(\psi_G)} \qquad (5.41)$$

Making the substitution,

$$\tilde{E}_{\pm 1} = |\tilde{E}_{\pm 1}|\exp(\pm i\,\Xi_{\pm 1}) \qquad (5.42)$$

produces the following set of equations

$$\frac{dI_{+1}}{dy} + 2\,\Gamma_B\,\frac{I_{+1}\,I_{-1}}{I_{+1} + I_{-1}} = 0 \qquad (5.43)$$

$$\frac{dI_{-1}}{dy} - 2\,\Gamma_B\,\frac{I_{+1}\,I_{-1}}{I_{+1} + I_{-1}} = 0 \qquad (5.44)$$

$$\frac{d\Xi_{\Delta}}{dy} - \Gamma_A\,\frac{I_{+1} - I_{-1}}{I_{+1} + I_{-1}} = 0 \qquad (5.45)$$

where $I_{\pm 1} = |\tilde{E}_{\pm 1}\,\tilde{E}_{\pm 1}^{*}|$, $\Gamma_A = \Gamma_{\Pi_{\sigma}}\cos(\Xi_g)$, $\Gamma_B = \Gamma_{\Pi_{\sigma}}\sin(\Xi_g)$ and $\Xi_{\Delta} = \Xi_{+1} - \Xi_{-1}$ is the phase shift between the beams.

These are key equations, since they determine the interaction between the two interfering beams, $I_{+1}(y)$ and $I_{-1}(y)$. When $|\Xi_g| = \frac{\pi}{2}$ or $\Gamma_A = 0$ (diffusion dominates), there is strong intensity coupling between the beams, but no phase coupling (the grating planes are straight). Whereas, when $\Xi_g = 0$ or $\Gamma_B = 0$ (drift dominates) there is strong phase coupling but no intensity coupling between the beams. Adding and subtracting equations (5.43) and (5.44)

$$I_{+1} + I_{-1} = I_0 = \text{constant} \tag{5.46}$$

$$\frac{dI_{+1}}{dy} + 2\,\Gamma_B \frac{I_{+1}(I_0 - I_{+1})}{I_0} = 0 \tag{5.47}$$

By making the substitution $I_{+1} = \frac{1}{u}$ equation (5.45) can be integrated.

Introducing, $m_0 = \dfrac{I_{-1}(0)}{I_{+1}(0)}$, (5.48)

$$I_{+1}(y) = \frac{I_{+1}(0)}{1 + m_0 \exp(-2\,\Gamma_B\, y)} \tag{5.49}$$

$$I_{-1}(y) = \frac{I_{-1}(0)\, m_0 \exp(-2\Gamma_B\, y)}{1 + m_0 \exp(-2\,\Gamma_B\, y)} \tag{5.50}$$

$$\frac{d\Xi_\Delta}{dy} = \Gamma_A \left[\frac{1 - m_0 \exp(-2\,\Gamma_B\, y)}{1 + m_0 \exp(-2\,\Gamma_B\, y)}\right] \tag{5.51}$$

Equation (5.51) can be immediately integrated by making the substitution $a = m_0 \exp(2\,\Gamma_B\, y)$, giving,

$$\Xi_\Delta(y) = \Xi_\Delta(0) + \frac{\Gamma_A}{2\Gamma_B} \ln\left[\frac{(1 + m_0)^2 \exp(-2\,\Gamma_B\, y)}{\left[1 + m_0 \exp(-2\,\Gamma_B\, y)\right]^2}\right] \tag{5.52}$$

The phase shift Ξ_Δ has been plotted below as a function of distance for different values of Ξ_G when $m_0 = 1$ and $\Gamma = 10^3$. As explained in appendix C, however, fringe warping will not be important when the grating is replayed at infra-red wavelengths.

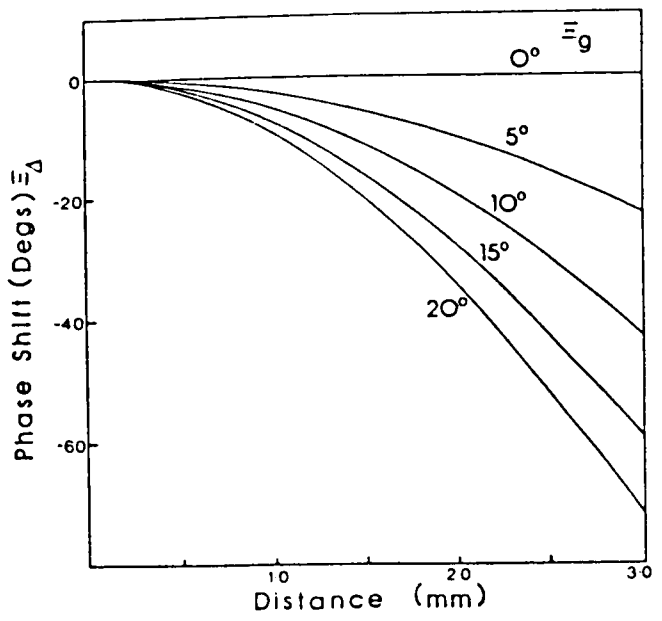

Fig: 5.3: Phase shift Ξ_Δ as a function of distance into the grating for $m_0 = 1$ and $\Gamma = 10^3$

For heavily doped material, Ξ_g tends to zero [101] (corresponding to $\Gamma_B \rightarrow 0$) and equations (5.49), (5.50) and (5.51) simplify to

$$I_{+1} = I_{+10},\ I_{-1} = m_0\, I_{10} \text{ and } \Xi_\Delta = \Xi_\Delta(0) - \frac{(1 - m_0)}{(1 + m_0)} \frac{\Gamma_\Pi}{\sigma} y \qquad (5.53)$$

According to equation (5.53), for the special symmetry case $\Xi_g = 0$, $m_0 = 1$ the grating will not interact with the recording beams and the dynamic recording model reduces to a latent recording model (this assumption is used in the next chapter). If $\Xi_g = 0$, $m_0 \neq 1$ the fringe planes inside the crystal will be slanted by a small angle. This is equivalent to replaying the grating at a slightly off-Bragg angle.

V.4 STAEBLER'S MODEL

Staebler's model will be used to predict the time development of the evolving grating. Combining equations (5.6) and (5.7),

$$\frac{\partial n_L}{\partial t} = G - \frac{n_L}{\tau_r} - \frac{1}{q}\frac{\partial J}{\partial z} \qquad (5.54)$$

where τ_r is considered as a constant recombination time and n_L is the density of photo-excited carriers. The effect of the spatially modulated N_D^+ and N_D concentration is therefore neglected. Furthermore, the free

carrier transport length, the distance electrons can move before being retrapped, is assumed to be considerably less than a fringe spacing, Λ. In other words, the value of τ_r is very small (typically between 10^{-9} and 10^{-8} s) and consequently n_L will always be in phase with the light interference pattern. If n_L is assumed to equal the steady state value,

$$n_L = G\,\tau_r = n[0]\left[1 + v\cos(Kz)\right] \tag{5.55}$$

where v is the modulation strength. From Maxwell's equation $\nabla\times\underline{H} = \underline{J} + \frac{\partial \underline{D}}{\partial t}$

$$\nabla.\left[\epsilon\,\frac{\partial \underline{E}}{\partial t} + \underline{J}\right] = 0 \tag{5.56}$$

or in one dimension,

$$\frac{d}{dz}\left[\epsilon\,\frac{\partial E}{\partial t} + J\right] = 0 \tag{5.57}$$

From equations (5.9) to (5.10)

$$J = q|\mu_e|n_L\left[E + E_p\right] + qD\,\frac{dn_L}{dz} \tag{5.58}$$

Equation (5.57) is integrated with values for n_L and J found in equations (5.55) and (5.58). Introducing the dielectric relaxation time τ_e in equation (4.21) and the Einstein relation in equation (4.6),

$$\frac{\partial}{\partial t}\left[E(z,t)\,\exp\left[f(z)\frac{t}{\tau_e}\right]\right] = -\frac{E_p}{\tau_e}\left[1 + v\cos(Kz)\right] +$$

$$+\frac{E_d}{\tau_e}\,v\sin(Kz) + \text{const} \tag{5.59}$$

$$\text{where, } f(z) = 1 + v\cos(Kz) \tag{5.60}$$

If E(z,0) = 0, then

$$E(z,t) = \left[E_p^2 + E_d^2\right]^{1/2}\,\frac{v}{f(z)}\left[1 - \exp\left[-f(z)\frac{t}{\tau_e}\right]\right]\cos(Kz-\Xi_g) \tag{5.61}$$

where,

$$\Xi_g = \tan^{-1}\left[\frac{E_p}{E_d}\right] \tag{5.62}$$

which for small modulation strengths approximates to

$$E(z,t) = \left[E_p^2 + E_d^2\right]^{1/2}\,v\left[1 - \exp\left[-\frac{t}{\tau_e}\right]\right]\cos(Kz-\Xi_g) \tag{5.63}$$

in agreement with equation equation (5.27) for $t \to \infty$.

Staebler's model predicts a saturation mechanism, with a time constant τ_e, due to the appearance of a space charge depletion field E which, in steady state equilibrium balances the internal fields. In practice, it is difficult to distinguish between the effects of field saturation and scattering since both will progressively retard the rate of grating formation. This will be apparent in the following chapter when the time development of the recorded grating is monitored.

CHAPTER SIX

RECORDING

VI.1 INTRODUCTION

This chapter examines the theoretical and practical design of the recording apparatus used to produce an IR filter in iron doped lithium niobate. Throughout, the experimental problems and their possible solutions are critically discussed.

The suitable recording wavelengths within the visible absorption band of the material are the strong 0·514 μm and 0·488 μm lines of the Argon-ion laser (though as explained later only the 0·514 μm line was used). For most experiments the replay wavelength was chosen to be 1·152 μm, compatible with the output from a IR converted He-Ne laser, though longer wavelengths of 1·3 μm and 1·5 μm, compatible with semiconductor lasers were also chosen.

The two material limitations listed below will play a central role in the rest of this chapter.

i) The refractive index of lithium niobate is particularly high (ordinary index $\tilde{n}_{ord}$ = 2·33 at a wavelength of 0·514 μm, compared with about 1·5 for glass).

ii) The exposure sensitivity of lithium niobate is low (typically 1 J/cm^2, compared with 10 $\mu J/cm^2$ for photographic emulsion).

The first limitation implies that only a restricted range of angles within the crystal are accessible to an external recording beam. The

second limitation implies long exposure times (of the order of minutes) and potentially serious stability problems.

VI.2 RECORDING ANGLES

The first stage in the design process is to calculate the angles of the incident recording beams, both inside and outside the crystal, necessary to form the desired IR grating. These angles will allow the grating to satisfy the Bragg condition at both the recording wavelength λ_G (where G stands for 'green') and the replay wavelength λ_R (where R stands for 'red'). Taking the modulus of equation (2.6),

$$2\,\underline{\rho}\,.\,\underline{K} = K^2 \qquad (6.1)$$

For a given grating the value of the expression on the left hand side of equation (6.1) must be independent of replay wavelength. In this infra-red filter

$$\underline{K} = \frac{2\pi}{\Lambda}\,\hat{\underline{z}} \qquad (6.2)$$

and therefore,

$$\underline{\rho}_G\,.\,\hat{\underline{z}} = \underline{\rho}_R\,.\,\hat{\underline{z}} = \text{const} \qquad (6.3)$$

The Ewald sphere representation of this relationship is shown in Fig 6.1. Expressed in terms of the beam angles inside the crystal at recording and replay, ψ_G and ψ_R and their corresponding wavenumbers β_G and β_R, equation (6.3) becomes,

$$\beta_G \sin(\psi_G) = \beta_R \sin(\psi_R) = \text{const} \qquad (6.4)$$

or,

$$\sin(\psi_G) = A \sin(\psi_R) \qquad (6.5)$$

where,

$$A = \left[\frac{\lambda_G}{\lambda_R}\right] \times \left[\frac{\tilde{n}_x(\lambda_R)}{\tilde{n}_x(\lambda_G)}\right] \qquad (6.6)$$

and $\tilde{n}_x(\lambda)$ is the dispersive refractive index of doped lithium niobate.

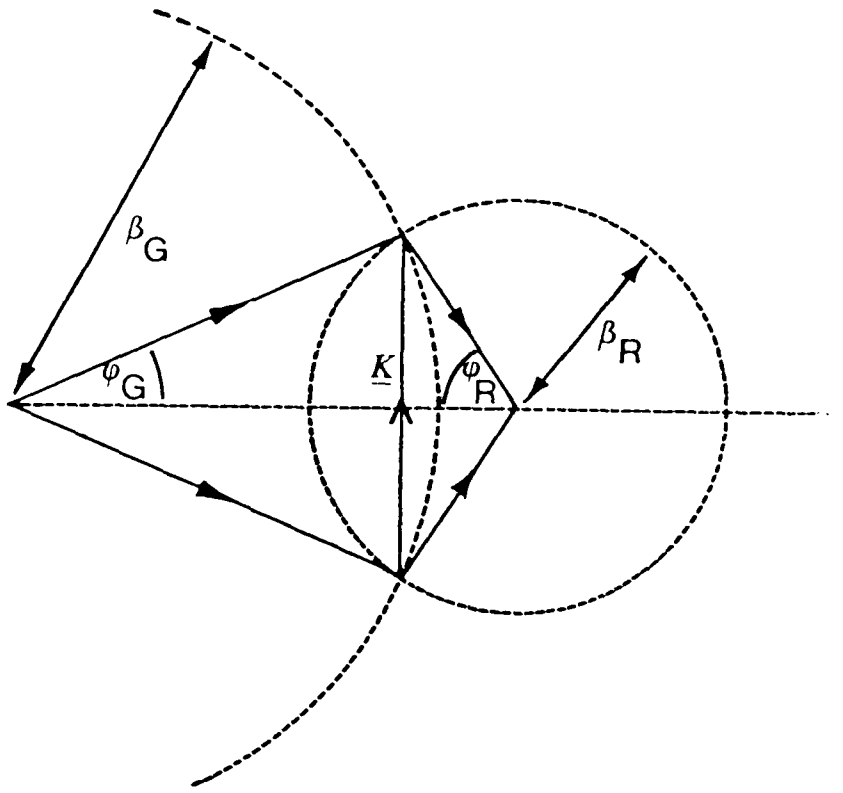

Fig 6.1: Ewald circles for recording and replay

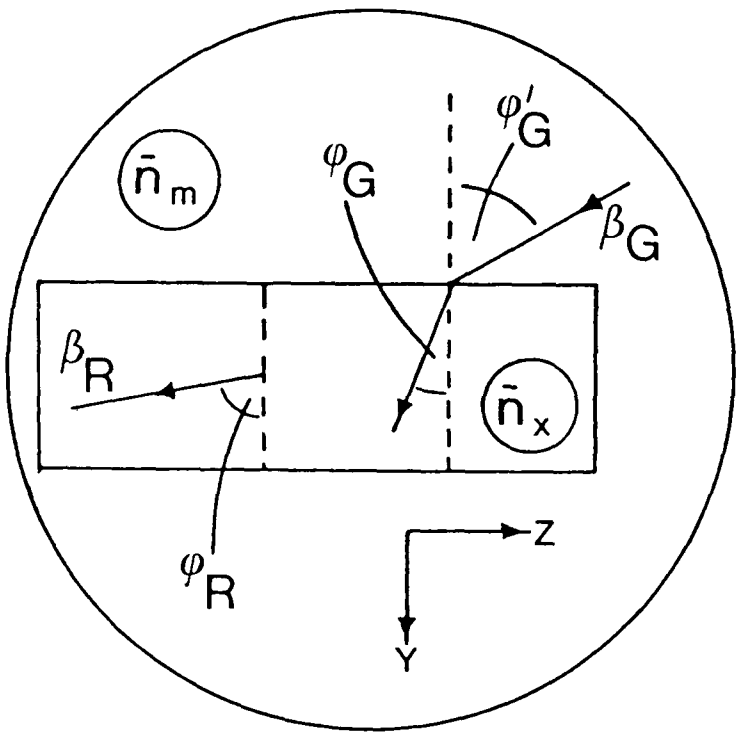

Fig 6.2: External and internal recording angles

If the recording beams are incident upon a (XZ) crystal face (see Fig 6.2), ψ_G can be easily related to the corresponding external recording angle, ψ'_G in a medium $\tilde{n}_m(\lambda_G)$. Phase matching at the boundary implies,

$$\sin(\psi'_G) = B \sin(\psi_R) \qquad (6.7)$$

where,

$$B = \left[\frac{\lambda_G}{\lambda_R}\right] \times \left[\frac{\tilde{n}_x(\lambda_R)}{\tilde{n}_m(\lambda_G)}\right] \qquad (6.8)$$

Only two refractive indices are needed to evaluate equation (6.8): the index of the external medium at recording, $\tilde{n}_m(\lambda_G)$, and the index of the holographic material at replay, $\tilde{n}_x(\lambda_R)$. No experimental figures have been found for the dispersive refractive index of iron doped lithium niobate crystals at visible and near infra-red wavelengths. According to the Debye equations [9] the difference in refractive index between doped and undoped samples will be caused by the main Fe^{2+} absorption band at a wavelength of 0·5 μm. At infra-red replay wavelengths (1·55, 1·3 and possibly 1·152 μm) the effect of the dopant will be small, justifying the use of values for undoped material. For example, direct excitation across the band-gap of undoped material at about 0·350 μm is responsible for the decrease in refractive index as the visible wavelength increases. At wavelengths longer than about 0·8 μm, however, the change is negligible.

The following table can therefore be compiled for replay at normal incidence ($\psi_R = 90^\circ$).

λ_G (μm)	λ_R (μm)	$\tilde{n}_x(\lambda_R)$	ψ_G (degs)	AIR ψ'_G (degs)	GLASS ψ'_G (degs)
0·514	1·152	$2·230^1$	27·8	84·8	40·9
0·514	1·3	$2·222^1$	22·1	61·4	35·3
0·514	1·55	$2·213^1$	18·4	47·3	28·9

Table 6.1: Recording angles for replay at normal incidence

where the refractive index for,

BK-7 glass : $\tilde{n}_m(0·514\ \mu m) = 1·52$ (from tables)

Air : $\tilde{n}_m(0·514\ \mu m) = 1·0$

Crystal : $\tilde{n}_x(0·514\ \mu m) = 2·33^1$

^{1} = values for undoped lithium niobate [11]

VI.3 FORMATION OF RECORDING BEAMS

Three different ways of producing the two interfering beams were considered (see Fig 6.3 below).

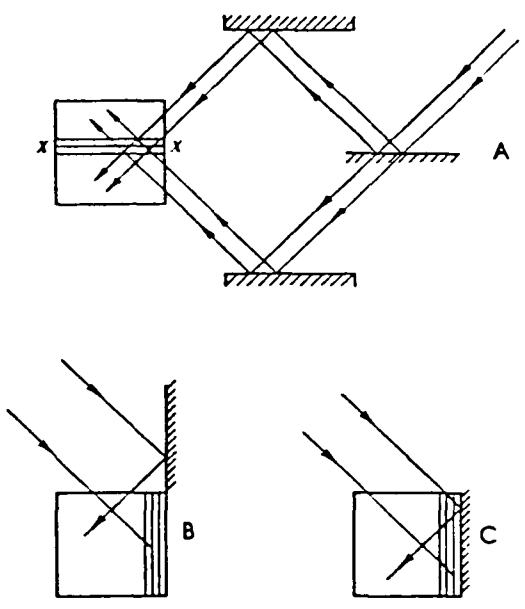

Fig 6.3: Types of recording geometry: (A) Beam splitter; (B) Lloyd's; (C) Lippmann.

Version A is the standard 'division of amplitude' method. In the symmetry plane XX the visibility of the light pattern is good because both interfering beams are derived from the same portion of the incident wavefront. Most of the interference pattern within a thick hologram, however, cannot satisfy this condition. Away from plane XX the grating quality will deteriorate, due to the progressively increasing spatial incoherence and intensity discrepancy between the two overlapping rays. In version A three separate optical components (two mirrors and a beam-splitter) have to be accurately aligned and rigidly fixed in position. For small angles of incidence (typically 10 to 20 degrees) this can be achieved using a specially constructed mirror and beam splitter assembly [62].

The alternative method, called 'division of wavefront', is typified by a Lloyd's or an off-normal Lippmann mirror. The incident beam is then divided into two halves by a mirror, either held above or fixed onto the

crystal. The quality of the grating should be best near the mirror and deteriorate further away.

The dynamic recording properties of lithium niobate impair the performance of version C in the following way. The evolving grating, behaving as a distributed Bragg mirror, intercepts and diffracts the incident light before it can reach the silvered mirror. By spatially altering the visibility of the interference pattern, the growth of the grating near the mirror is retarded. This mechanism was used to monitor the growth of a normal reflection Lippmann hologram recorded at 0·514 μm. As mentioned in chapter two, the effective path length of the diffracted beam within the crystal is determined by the efficiency of the grating. When bulk absorption is present, this change of path length causes a substantial increase of the diffracted intensity.

VI.4 THE FINAL DESIGN

Following the discussions in sections VI.2 and VI.3 it was decided to use a prism in an original way - not only to reduce the high angles of incidence, but also to create the two beams using the version B configuration.

In the final design the crystal was positioned between two polished 45^{o} right-angled prisms made from high optical quality, inexpensive, BK-7 glass. Between the crystal and each prism was a thin liquid layer of dibutate (di-n-butyl phthalate) with a refractive index of 1·498 (at a wavelength of 0·5 μm) which partially index matched the crystal onto the glass and also held the optical components together by surface tension. The idea of a hollow prism [93], containing both dibutate and the crystal was rejected, despite its excellent temperature control, on the grounds that phase instability could be a problem. Nevertheless, if the crystal

has to be held at an elevated temperature for simultaneous recording and fixing, the method is worth trying.

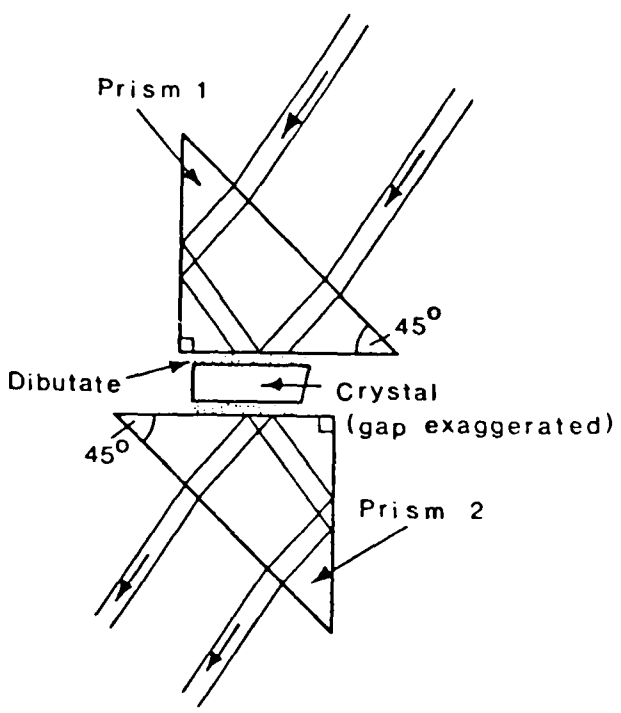

Fig 6.4: Double prism recording arrangement.

As shown in Fig 6.4, one half of the incident beam is internally reflected within prism 1 to form the other recording beam. The two halves of the collimated beam, of near equal intensity, overlap within the crystal to form a light interference pattern with fringe planes perpendicular to the c-axis of the crystal. The accuracy of alignment is primarily limited by the accuracy of X-ray crystal orientation (typically ± 0·5 degrees). Prism 2 serves to realign the two halves of the beam so that they propagate in the same direction in free space.

The incident beams were deliberately polarised normal to the plane of incidence. The grating coupling is then determined by the coefficient Γ_{π}, smaller than Γ_{σ} because the electro-optic tensor component $r_{113} < r_{333}$ (see chapter five and appendix one). Although a high coupling coefficient is desirable at replay, the opposite is true at recording. Coupling at recording causes unwanted effects like fringe bending and dynamic scattering.

This design has the following advantages and disadvantages:

VI.4.1 Advantages

1) - The large incident angles of the beams in free space, necessary to record a grating in a high refractive index material (see table 6.1), are difficult to achieve and will also make the dimensions of the slanted crystal appear in perspective considerably different from their normal values. Consequently, most of the incident light will be wasted, unless the spherical collimating lenses are replaced by cylindrical lenses. A prism considerably reduces these angles and allows more efficient utilisation of the available light. 2) - The alignment procedure is straightforward: with the angles of the prism already known, only the hypotenuse of prism 1 has to be orientated relative to the incident beam during the experiment. 3) - Each incident beam can be separately blocked or attenuated. 4) - The position of the fringe pattern inside the crystal will be immune to linear displacement of the prism assembly. 5) - Because only one external beam is necessary, the recording geometry can be very compact.

VI.4.2 Disadvantages

1) - The quality of the grating relies upon the good spatial coherence, parallelism and intensity uniformity of the laser beam. The spatial coherence and uniformity across the interfering beams can be improved by expanding the laser beam to a larger diameter, though at the expense of a reduced beam intensity and hence a longer exposure time.

The phase front across a slightly de-collimated laser beam can be represented by a mathematical function of the form [59]

$$\chi(w) = \pm A w^2 \qquad (6.9)$$

where the variable A determines the degree of de-collimation and w is measured across the beam. If the prism reflects the incident beam about

a point $w = w_o$ on the wavefront (as shown in Fig 6.5) the relative phase between the recording beams will depend on w. For rays derived from points $\chi(w + \omega_o)$ and $\chi(w - w_o)$,

$$\chi(w + w_o) - \chi(w - w_o) = \pm 2 A w_o w \qquad (6.10)$$

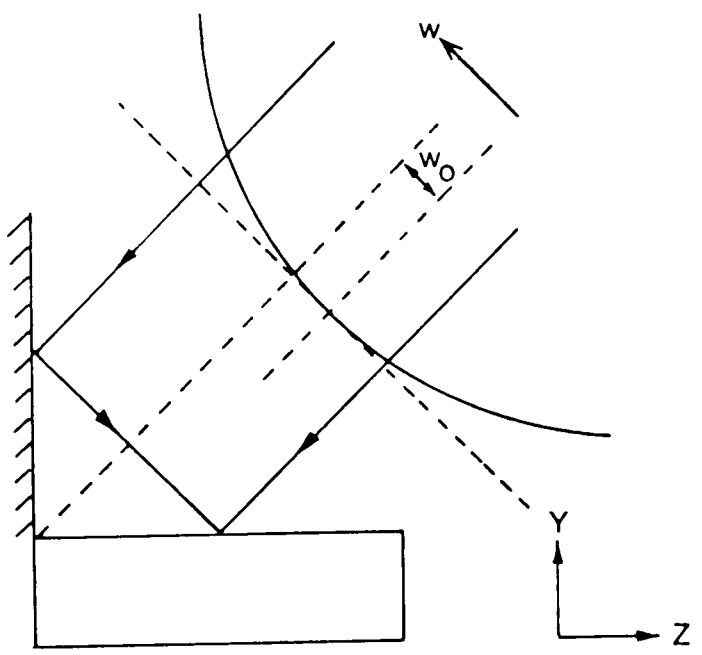

Fig 6.5: De-collimated incident beam

Consider the effect of this phase shift on the position of the grating near the incident face (y = 0). When the incident beam is not exactly divided into two symmetrical halves ($w_o \neq 0$) the grating will be linearly chirped along the crystallographic z-axis direction.

2) - The several optical surfaces involved are potential sources of scattered and reflected radiation. Scattered light will help to cause noise gratings, whereas reflected light may cause spurious infra-red gratings.

VI.5 EXPOSURE TIME

The choice between the 0·514 μm and 0·488 μm recording wavelength was a compromise between the optical sensitivity of the crystal, the laser power, and the uniformity of the desired grating. The 0·488 μm line, at the centre of the visible Fe^{2+} absorption band, optimises the holographic exposure sensitivity of the material, but implies that the

recording beams will be substantially attenuated as they pass through the crystal, forming a grating with large variations in modulation strength. The power output from the laser at this shorter wavelength is also less. Therefore, the 0·514 μm line, associated with lower absorption was chosen.

VI.6 EQUIPMENT

The layout of the recording apparatus is given overleaf in Fig 6.6. In the rest of this section the various components will be described in detail.

An Innova 164 Argon-ion laser was the source of coherent light used in the recording experiments. This laser can generate a maximum single frequency power output of 1·4 Watt at a wavelength of 0·5145 μm or 0·8 Watt at 0·488 μm, has a longitudinal coherence length of several metres, excellent spatial coherence operating TE-00 mode, and emits vertically polarised light due to the Brewster cavity windows.

The recording beam was obtained by expanding the laser beam to a diameter of about 4 cm using a high quality × 20 microscope objective lens, and an Ealing Beck achromatic doublet lens mounted on a minibench. A 20 μm pinhole was placed at the focus of the lens to spatially filter the beam. The spatial coherence across the expanded beam was checked with a Fresnel bi-prism. Two halves of the expanded beam were overlapped to form a far field interference pattern with low fringe frequency. The visibility of this pattern was measured at different distances from the prism. As expected, the spatial coherence across the whole width of the recording beam was found to be good.

Diagnostic techniques were also developed to quantify the wavefront aberration of the beam forming assembly. For example, the performance of

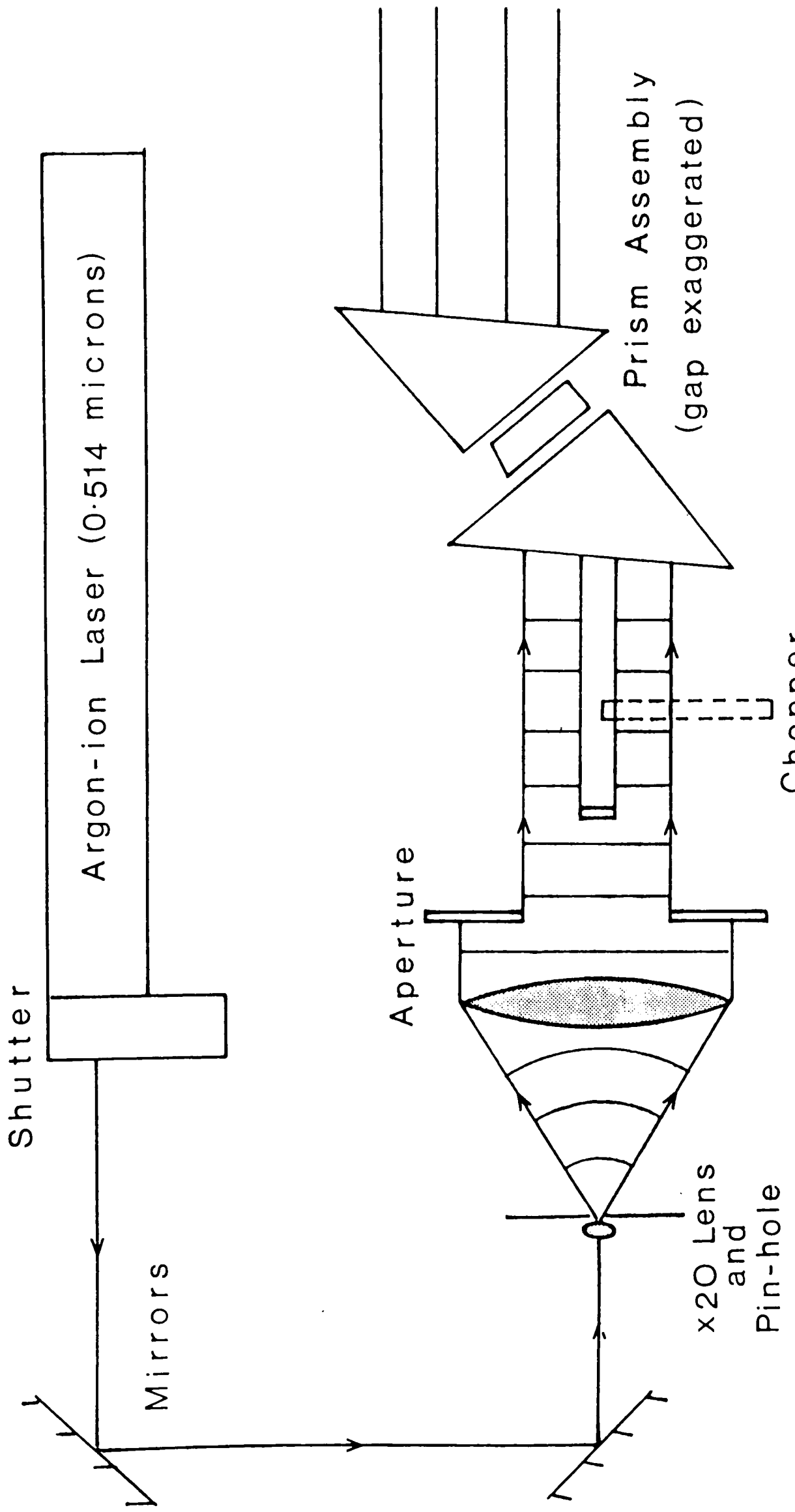

Fig 6.6: Diagram of recording apparatus

the collimating lens was deduced from measurements taken on a **Twyman**-Green interferometer at the National Physical Laboratory. The two interferograms shown in Fig 6.6 below indicate that, although the lens was not diffraction limited, a good central portion existed.

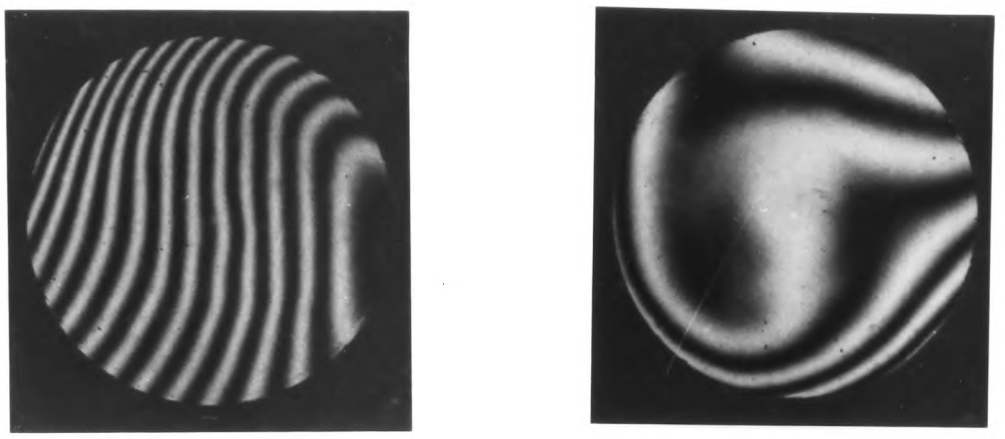

Fig 6.6: Two **Twyman**-Green interferograms of the achromatic doublet collimating lens

A wavefront shearing interferometer [69], in practice a solid glass etalon about 2 cm thick, was regularly used to minimise collimation errors and other residual aberrations in the expanded beam. The etalon was placed in the expanded beam at an angle of about 45 degrees and a series of lines were observed in the region where the reflected beams from the two glass faces overlapped. When these lines disappeared the beam was judged to be well collimated.

The crystals used in this project were $9 \times 3 \times 9$ mm^3 in dimension (orthogonal axes corresponding to the X,Y,Z material directions). Further details of their growth and preparation can be found in appendix E. In a Newton's rings experiment the flatness of every polished crystal face was compared with a reference $\lambda/20$ optical flat. The consistently straight fringes obtained demonstrated the high quality of polishing and implied less than a $\lambda/10$ variation in dimension across each face (where λ is the wavelength of the mercury green line). If, as occurs here, non-uniform changes in thickness are negligible, the refractive index homogeneity of the crystal can be determined from optical path measurements alone. For these crystals the test was particularly

straightforward to implement, because the two 9×9 mm^2 (XZ) faces, polished nearly parallel, formed a solid etalon. The interference pattern produced by a collimated (0·514 μm) laser beam reflected off these faces is shown below, for crystal I and crystal II.

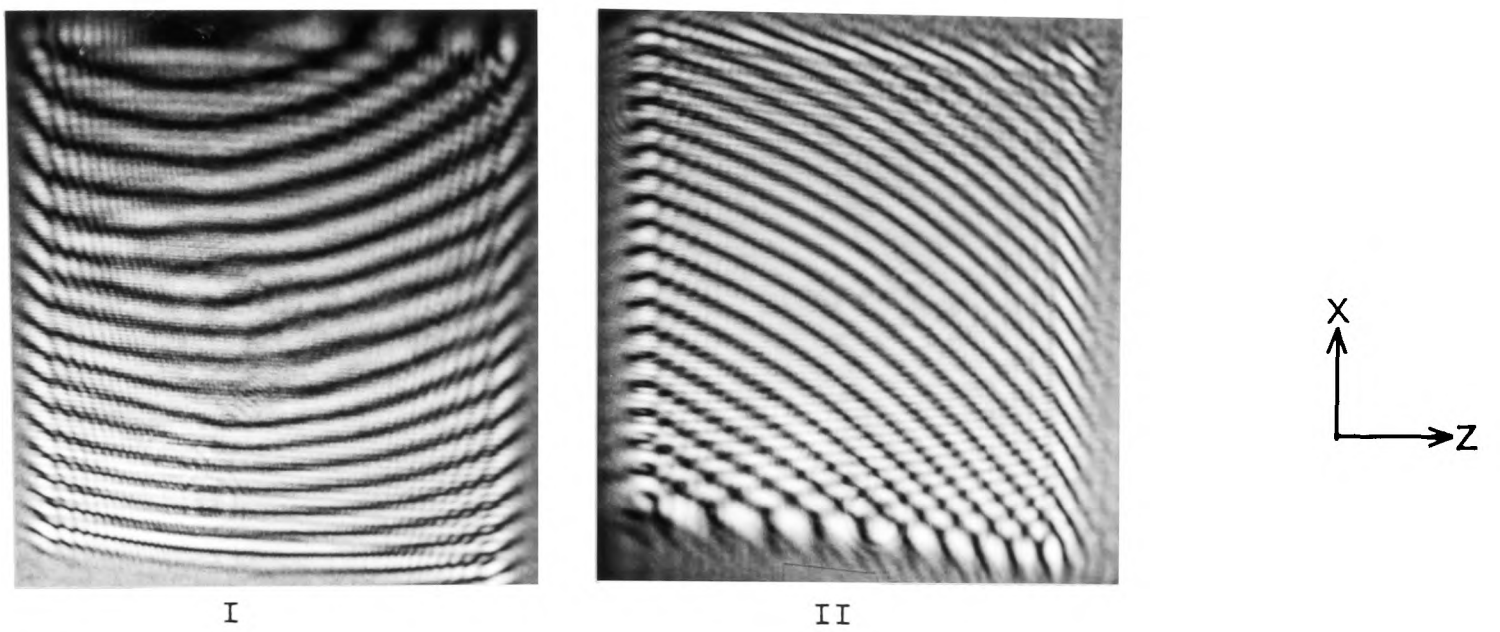

Fig 6.7: Etalon fringes from crystal I and crystal II

The two right-angled, BK-7 glass prisms used in the recording experiments, dimensions $(17 \times 17 \times 14)$ mm^3, were polished flat to $\lambda/10$ on all square faces and were bloomed on their hypotenuse faces to reduce reflections. An accurate value for the refractive index of the glass was determined by placing each prism on a prism spectrometer. The light source was an incandescent lamp, spectrally filtered to produce a narrow wavelength range, centred on (0·515 ± ·001) μm. Minimum deviation of a refracted beam from a ($45^\circ \pm 1'$) apex occurred at ($26^\circ \pm 1'$), corresponding to a refractive index of (1·521 ± 0·001) – in good agreement with standard data.

VI.7 STABILITY

Changes in room temperature and light absorption within the crystal were sources of thermal instability. The importance of these effects can be assessed from a few preliminary calculations. The relaxation time τ_t

defined below, determines the time for the crystal to reach thermal equilibrium with its mount before the exposure (assuming good thermal contact).

$$\tau_t = \left[\frac{L}{2\pi}\right]^2 \times \left[\frac{C_p \rho_t}{k_t}\right] \leqslant 2 \times 10^{-2} \text{ secs} \qquad (6.11)$$

where L is the period of the thermal variation, assumed to be $\leqslant$ 9 mm, C_p is the heat capacity of undoped material, with value [104] 640 J/kg/K, k_t is the thermal conductivity with value [104] 420 W/m/K, and ρ_t is the density of the material, with value $4{\cdot}65 \times 10^3$ kg/m^3. According to equation (6.11) thermal equilibrium is quickly established.

When the laser beam illuminates the crystal, heat will be generated internally. The worst possible practical case occurs when a beam with a typical intensity I of 100 mW/cm^2 is totally absorbed within the material and no heat sink is present. The rate of temperature increase inside the crystal, ΔT will then be,

$$\Delta T = \frac{I\ A\ t}{C_p\ \rho_t\ V} \approx 0{\cdot}1\,^{\circ}\text{C/sec} \qquad (6.12)$$

where A is the area of the crystal, V its volume, and t the time.

Consider the effect of temperature on the optical path $\Delta(OP)$ along the c-axis of the crystal. The quantity $\Delta(OP)$ can be written as

$$\Delta(OP) = \tilde{n}d \left[\alpha_c + \delta_c\right] \Delta T \qquad (6.13)$$

where,

$$\alpha_c = \frac{\partial d(T)}{\partial T\ d} \qquad (6.14)$$

$$\delta_c = \frac{\partial \tilde{n}(T)}{\partial T\ \tilde{n}} \qquad (6.15)$$

The first term inside the brackets is the contribution to optical path changes caused by changes in length, where α_c is the linear expansion coefficient. The second term is the contribution caused by changes in refractive index. Typical values for $\tilde{n}$, α_c and δ_c at both recording and replay are tabulated below (where ^{1} = [11], and ^{2} = [104]).

λ (μm)	$\tilde{n}$	δ_c (10^{-6})	α_c (10^{-6})	($\delta_c + \alpha_c$) (10^{-6})
0·514	2·34	$14·0^1$	$2·0^2$	16·0
1·152	2·23	$2·0^1$	$2·0^2$	4·0
1·29	2·22	$1·0^1$	$2·0^2$	3·0
1·55	2·21	$1·0^1$	$2·0^2$	3·0

Table 6.2: Contributions to changes in optical path along the c-axis.

For a fixed external recording angle ψ'_G, wavelength λ_G and external refractive index $\tilde{n}_m$, the grating period Λ will be independent of crystal refractive index $\tilde{n}_x$, since,

$$\Lambda = \frac{\lambda_G}{2\,\tilde{n}_x \sin(\psi_G)} = \frac{\lambda_G}{2\,\tilde{n}_m \sin(\psi'_G)} \qquad (6.16)$$

Therefore, from the point of view of the recording beams, internal refractive index changes are unimportant. Thermal expansion, however, will shift the partially formed grating relative to the interference pattern. If the total length of the crystal along the c-axis is to change by less than half a fringe plane,

$$\alpha_c\, d\, \Delta T < \frac{\Lambda}{2} \qquad (6.17)$$

For Λ = 0·5 μm, d = 4 mm, $\Delta T(\max) < 30^{\circ}C$.

The recording apparatus was rigidly attached by magnetic bases to an optical table, vibration isolated from the ground by inflatable tyres. The prism assembly, however, was left free-standing and only held together by surface tension forces. The idea of mechanical restraint, achieved by clamping the prism, was rejected because the stress could cause either perturbations in refractive index or mechanical creep.

VII.8 FINAL PREPARATIONS

All the optics including the two prisms and crystal were carefully cleaned with methanol, prior to the exposure. Aided by the process of capillary action, only a few drops of dibutate were sufficient to coat the crystal surfaces. The success of the technique could then be assessed by observing the intensity of the two parallel beams emerging from the far prism. Air bubbles in the liquid film were easily detectable as dark patches.

The following procedure was undertaken to align prism 1. As an initial precaution, to prevent premature formation of the grating, the expanded laser beam was attenuated with a 20 dB neutral density filter, and its diameter reduced to about 1 mm using an iris. The prism mount was rotated until the hypotenuse face of prism 1 back reflected the incident beam (to within ± two minutes). The crystal and prism assembly could then be rotated about a vertical axis to its final angle: $6^{o}\ 30^{"}$, with the incident face of the crystal turned towards the beam. This value corresponded to an external replay angle of about 10 degrees measured relative to the c-axis at a wavelength of 1·152 μm. The reason for this choice is explained in chapter seven.

VI.9 MONITORING

VI.9.1 Real-time Holographic interferometry

Observing the temporal change of the intensity profile across either of the two output beams gave information about the mechanical and thermal stability of the crystal. The chief advantage of this technique was its simplicity; no additional equipment is needed to make this measurement. The conclusions were therefore directly relevant to the recording process, though with the grating evolving over a period of

minutes, any features must be considered as only a time integrated contribution.

The intensity change will be derived from a simple model assuming the latent interaction of two coherent, spatially uniform beams on a sinusoidal phase grating. A spatially variable phase shift is introduced, either by displacing the z-origin of the grating, or by assuming a phase change between the two interfering beams; both approaches are mathematically identical. The former model is appropriate for thermal expansion, whereas the latter is appropriate for phase variations in the index matching liquid.

For an 'on-Bragg' transmission grating ($c_R = c_S$) with no absorption, equation (2.19) reduces to

$$\frac{dR(y)}{dy} = - i\kappa^o S(y), \quad \frac{dS(y)}{dy} = - i\kappa^o R(y) \tag{6.18}$$

where,

$$\kappa^o = \frac{\kappa}{c_R} \tag{6.19}$$

and the crystallographic z-axis, appropriate for replay, has been replaced by the crystallographic y-axis. Solving these pair of equations,

$$R(y) = a\, e^{i\kappa^o y} + b\, e^{-i\kappa^o y} \tag{6.20}$$

$$S(y) = -a\, e^{i\kappa^o y} + b\, e^{-i\kappa^o y} \tag{6.21}$$

The coefficients a and b are determined from the boundary conditions at the incident face for unity beam ratio,

$$R(0) = 1, \; S(0) = e^{i\Xi} \tag{6.22}$$

Hence,

$$R(y) = \cos(\kappa^o y) - i\, e^{-i\Xi} \sin(\kappa^o y) \tag{6.23}$$

$$S(y) = -i \sin(\kappa^o y) + e^{i\Xi} \cos(\kappa^o y) \tag{6.24}$$

$$I_R(d) = |R(d)R^*(d)| = 1 - \sin(2\kappa^o d) \sin(\Xi) \tag{6.25}$$

$$I_S(d) = |S(d)S^*(d)| = 1 + \sin(2\kappa^o d) \sin(\Xi) \tag{6.26}$$

Equations (6.25) and (6.26), predict that the beam amplitudes, I_R and I_S, will pass through a series of maxima and minima as the phase discrepancy Ξ between the grating and light pattern increases, with the size of the variation determined by the coupling efficiency of the hologram.

Consider the expected pattern across the output beam due to thermal expansion of the crystal. Initially the period of the grating and the interference pattern will be the same, with value Λ given by equation (6.16). As the crystal expands the distance between the grating planes will also increase. The result will be an accumulated phase mismatch across the interfering beams between the position of the light interference pattern and the grating planes. For a thermal expansion along the c-axis of the crystal by Λ, one straight line will be produced across the output beam. In the recording experiments generally no intensity variation across the recording beams was observed.

VI.9.2 Michelson interferometer

Optical path changes in the crystal were measured interferometrically using a 1 mW, 0·633 μm Helium-Neon laser beam. It is a good way to monitor the development of the grating because, at this long wavelength and low power level, electrons in the crystal will not be significantly photo-excited. Consequently, an efficient grating cannot be formed. Furthermore, with both length and refractive index contributing to thermal changes in optical path, the diagnostic technique is a sensitive monitor of crystal temperature.

One arm of a Michelson interferometer contained the c-axis of the crystal and two photodiodes measured the intensity of the expanded interference pattern at different places. The signals from these detectors were combined in an X-Y oscilloscope to form a Lissajous

figure. In a series of experiments, for a typical laser intensity of about 80 mW/cm^2, less than a $\lambda/8$ movement of the fringe pattern occurred over a three and half minute exposure.

VI.9.3 Diffraction efficiency measurements

When monitoring the formation of the grating, the dynamic recording properties of the material can be used to advantage. If one of the interfering beams is blocked, the recording geometry is converted into the replay geometry at the same wavelength and the grating strength can be inferred from the intensity of the diffracted beam. This information is useful for a number of reasons. By periodically measuring the diffraction efficiency, a temporal profile of the grating strength can be produced. Consequently, a), the growth of the grating can be stopped at a predetermined, reproducible point, b), the strength of the IR grating can be predicted, and c), the effect of dynamic scatter loss can be monitored.

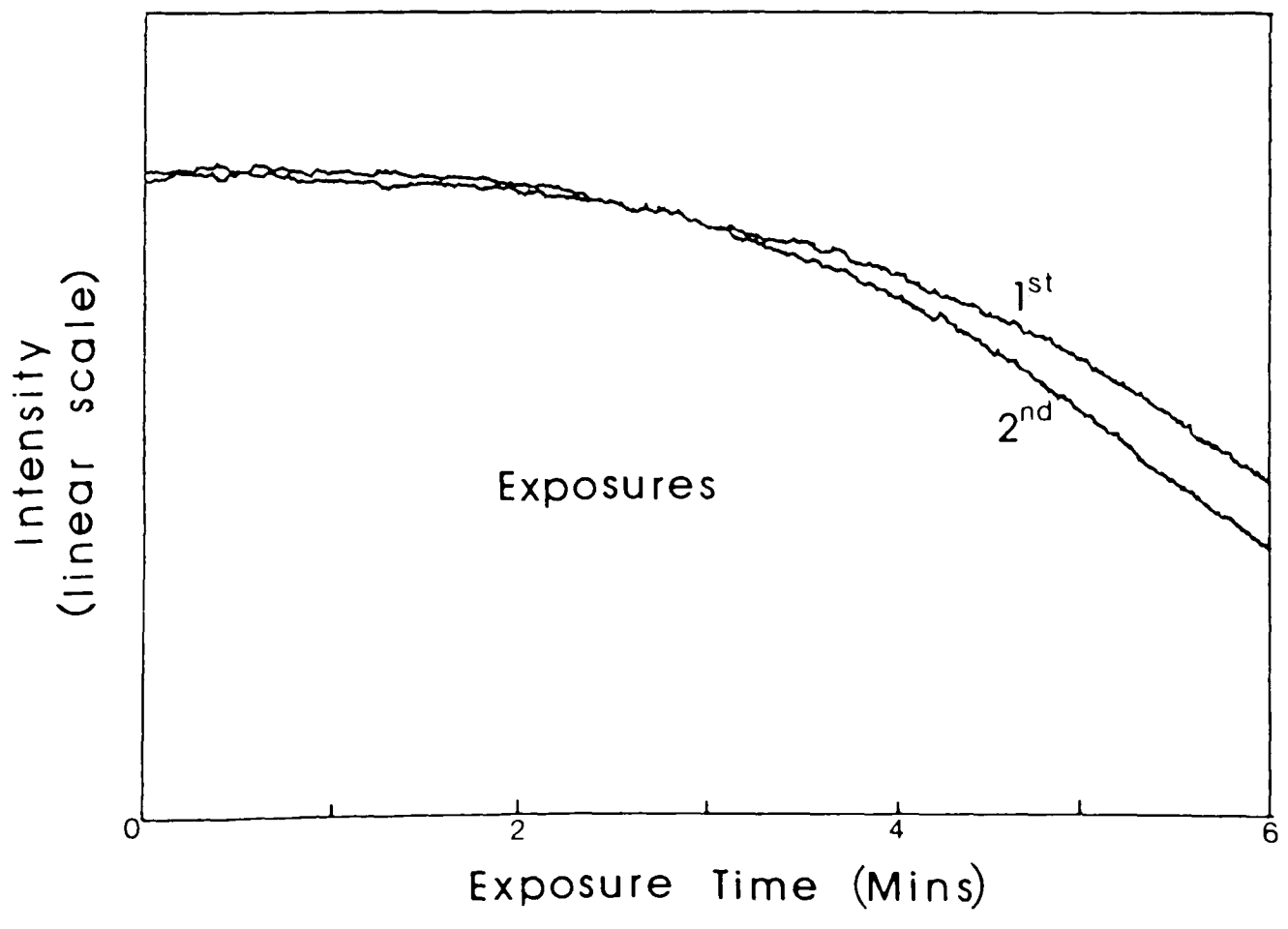

Fig 6.8: Transmitted intensity of a single laser beam passing through crystal I (optically erased with incoherent light between exposures)

In photographic emulsion, the exposure-modulation strength characteristics of the hologram are repeatable. Holograms recorded in iron doped lithium niobate, on the other hand, differ from exposure to exposure, when produced under comparable conditions. This can be attributed to the unpredictable effects of dynamic scattering (see Fig 6.8) and the previous history of the material. It is a major failing with the material and means that the growth of the grating must always be monitored.

To minimise the change in recording conditions caused by the process of measurement, the period while one beam is blocked must be small compared with the total time of recording. If this is not achieved the grating will be partially erased when only one beam illuminates the crystal. Fortunately, the erasure time for heavily doped material is substantially longer than the recording time.

A rotating mechanical chopper with four thin vanes was arranged to block one of the recording beams every 4·0 s for about 0·3 s, while the intensity in either the diffracted or transmitted beam (see Fig 6.9) was

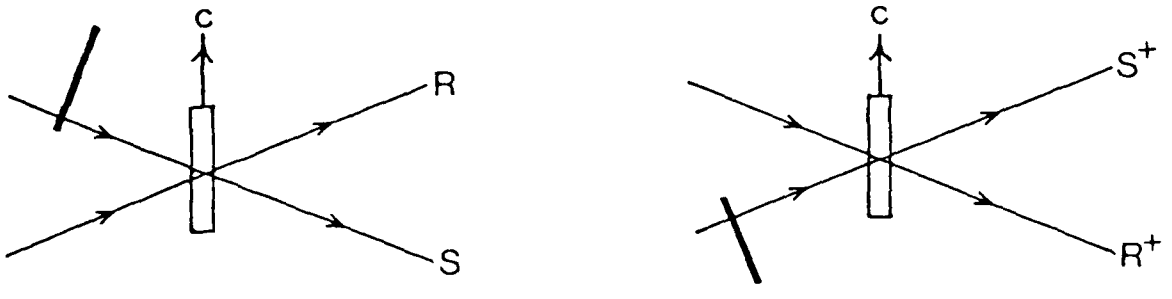

Fig 6.9: Notation for recording beams

being measured with a small area silicon photodiode detector. Only one detector was used in order to standardise the results of the diagnostic equipment. The electronic output from the detector was stored for convenience on a high slew rate digital storage scope before being plotted out on a X-Y chart recorder.

The recorded data plotted the beam intensity when both one or two incident beams were present. A sample trace is given in Fig 6.10 below, where the sharp vertical lines mark the periods of beam interruption.

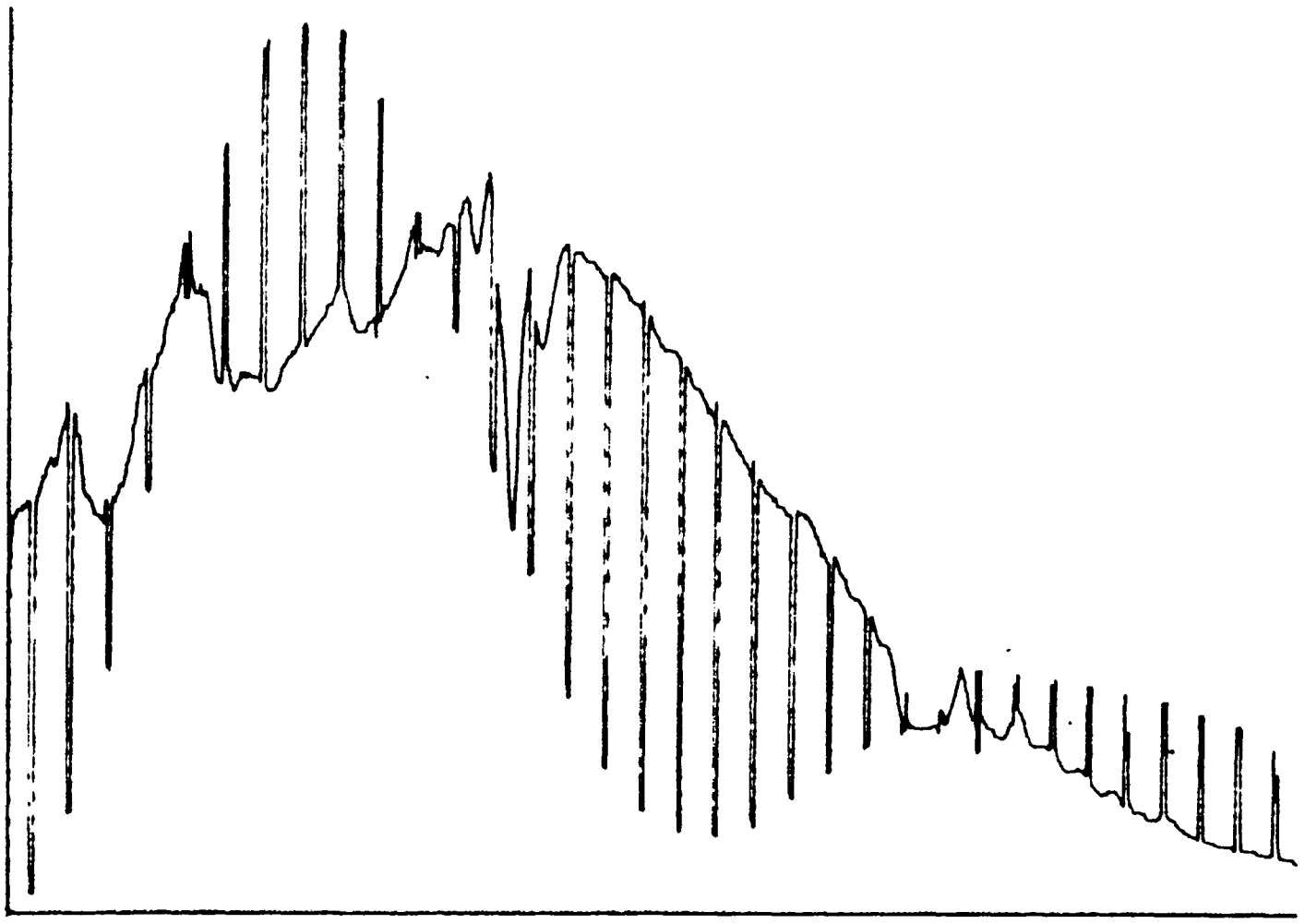

Fig 6.10: Sample trace of original data

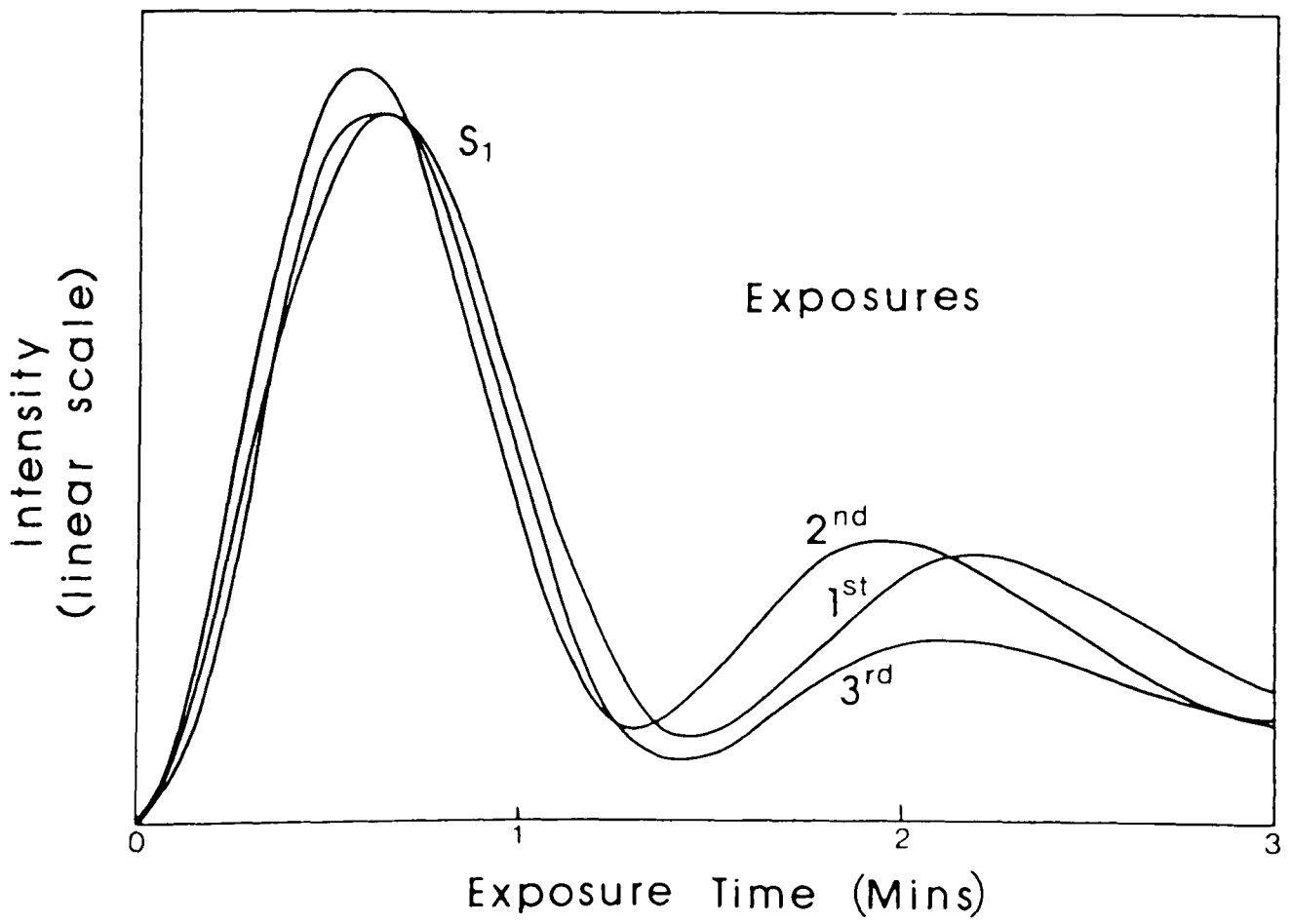

Fig 6.11: Intensity of diffracted beam S_1 (where 1 denotes one incident beam) for three gratings recorded under similar conditions.

The first set of results, traced from the original data, draws a comparison between curves showing the time development of diffracted beam intensity for three different exposures on the same day. Between each exposure the crystal was illuminated with incoherent light for about two hours to remove the grating (see section IV.5). The aim of this procedure was to return the crystal to its former state without disturbing the recording arrangement. As shown in figure 6.11, although the agreement between the curves is initially good, there is a progressive deterioration in similarity for longer times of exposure. Since all the curves start from zero, there is good evidence that complete optical erasure has occurred.

Figure 6.12 compares the output beam intensity for two exposures, when both incident beams are present. As discussed in section 9.1, the output beam intensity is now very sensitive to phase instability - demonstrated by the jagged features of the trace. Nevertheless, the similarity is remarkably good.

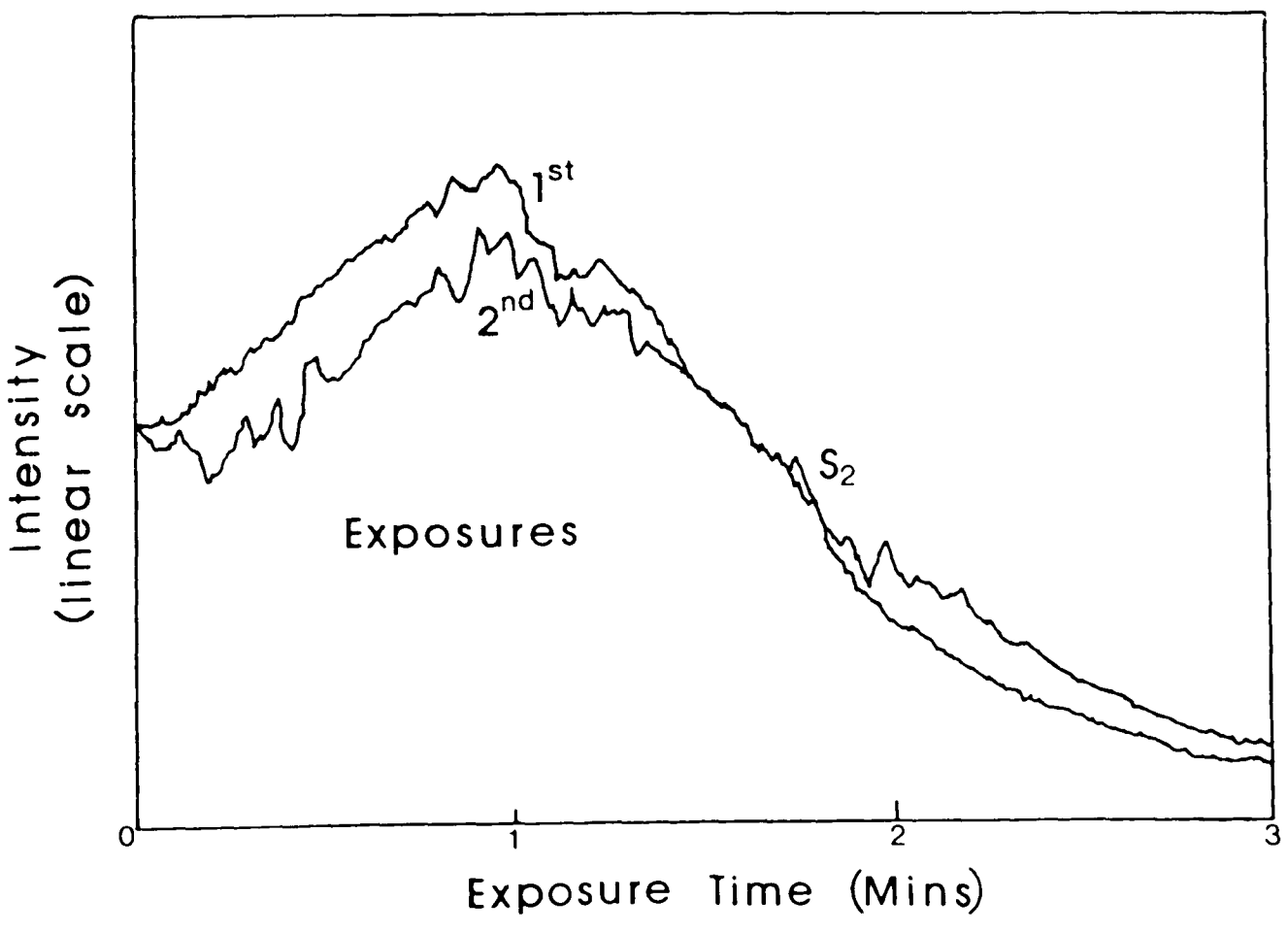

Fig 6.12: Intensity of output beam S_2 (where $_2$ denotes two incident beams) under similar conditions.

The signal levels implied a non-unity beam ratio at the incident face of the crystal. To confirm this hypothesis, without changing the intensity or position of the beams, the mirror image of the recording geometry was created by making the chopper and detector intercept the other beam. The discrepancy in signal levels between the two arrangements (see Fig 6.13) was consistent with a nearly 2:1 beam ratio.

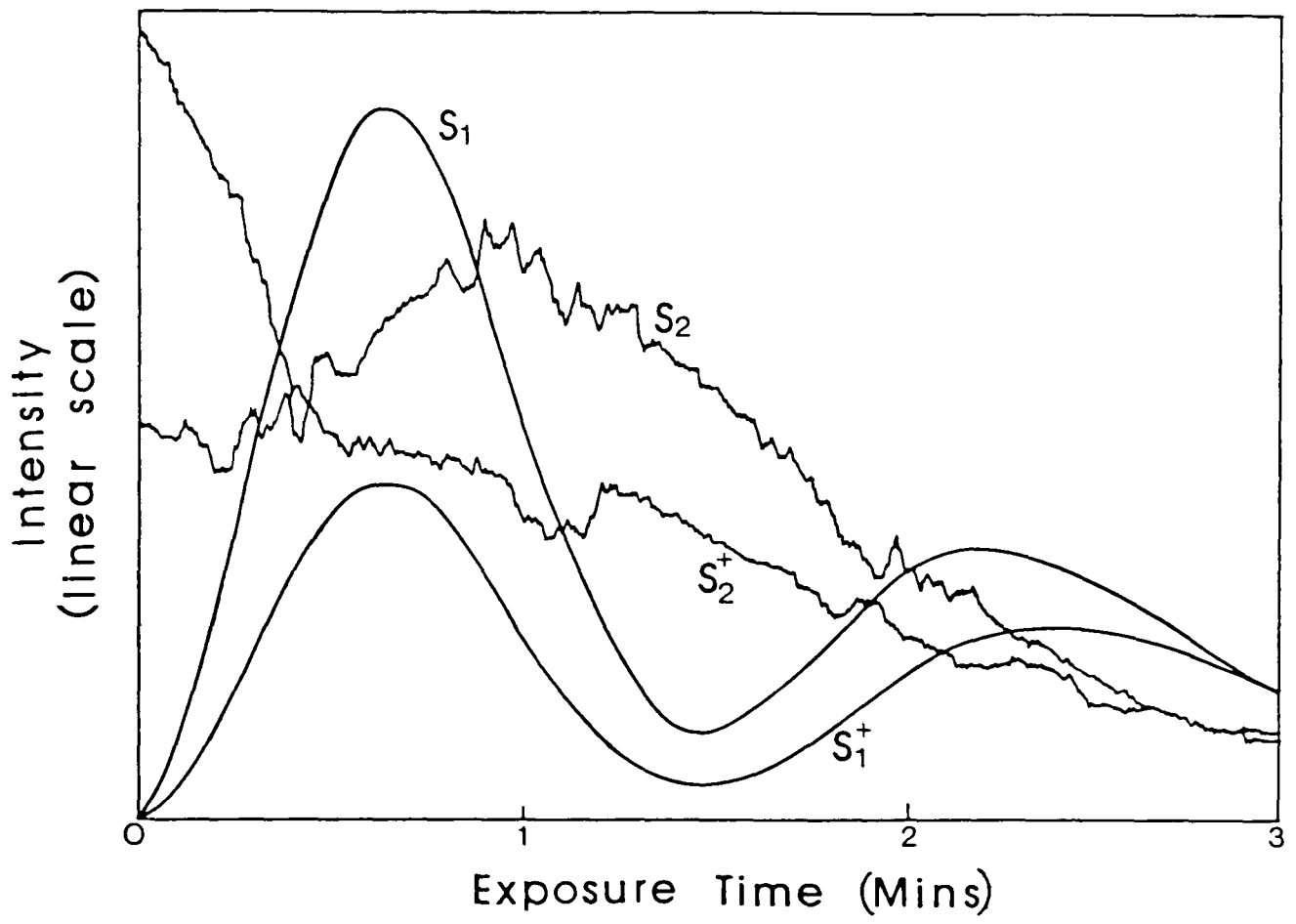

Fig 6.13: Inversion of beam ratio by moving chopper and detector to the other beam

The average intensity of the expanded beam was temporarily reduced by a factor of two and the time development of the diffracted beam was measured again (Fig 6.14 overleaf). Within the limits of experimental variation the exposure time required was now twice as long.

The growth of the transmitted beam intensity relative to diffracted intensity is shown in Fig 6.15. On adding the intensities of both beams together, power conservation failed to be satisfied, primarily because the transmitted beam was oscillating at a faster rate than the diffracted beam. As discussed in detail below, there is a good reason for this effect - noise or other spurious gratings are also diffracting power out

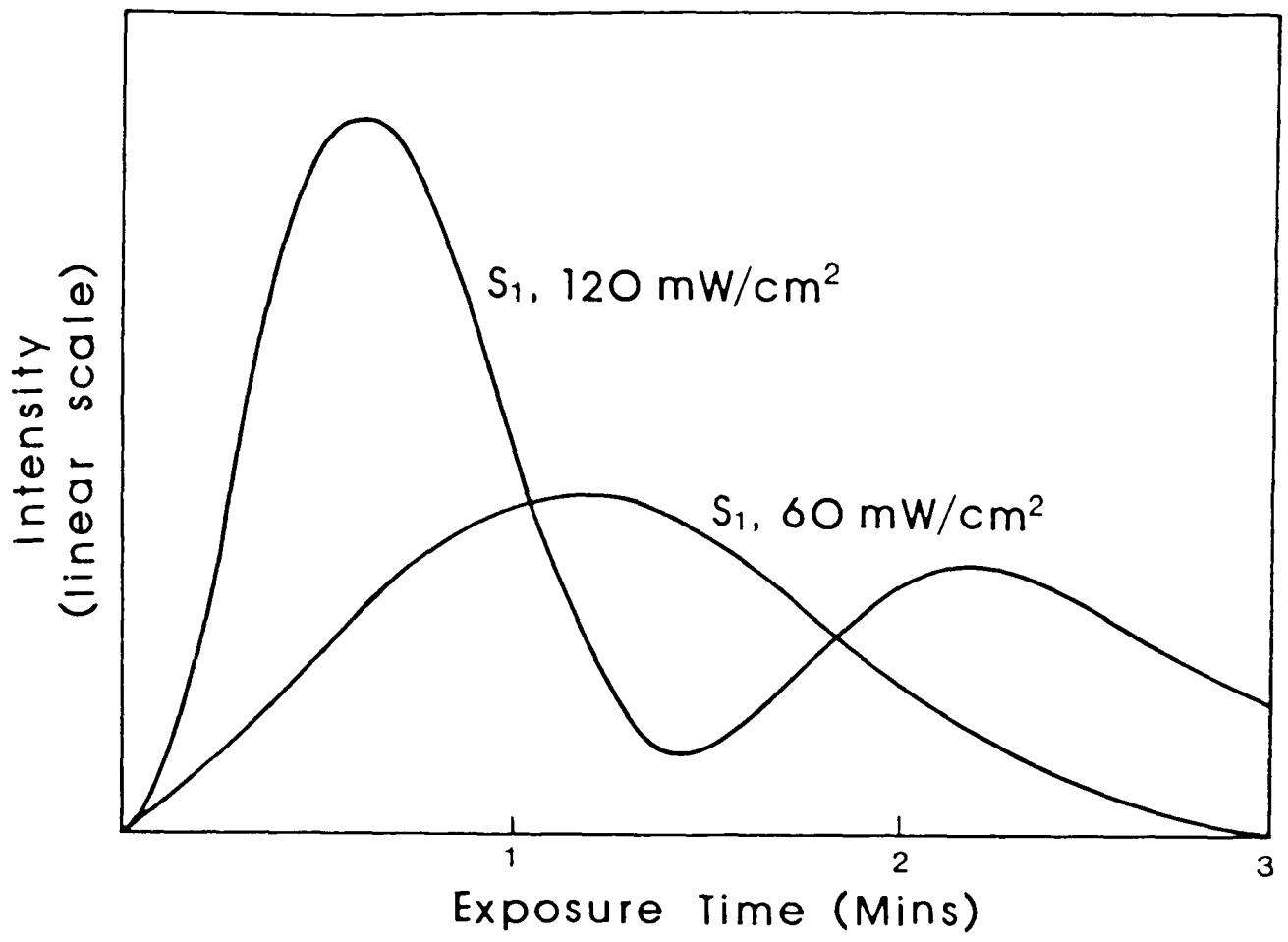

Fig 6.14: Time development of the diffracted beam for two different exposure intensities

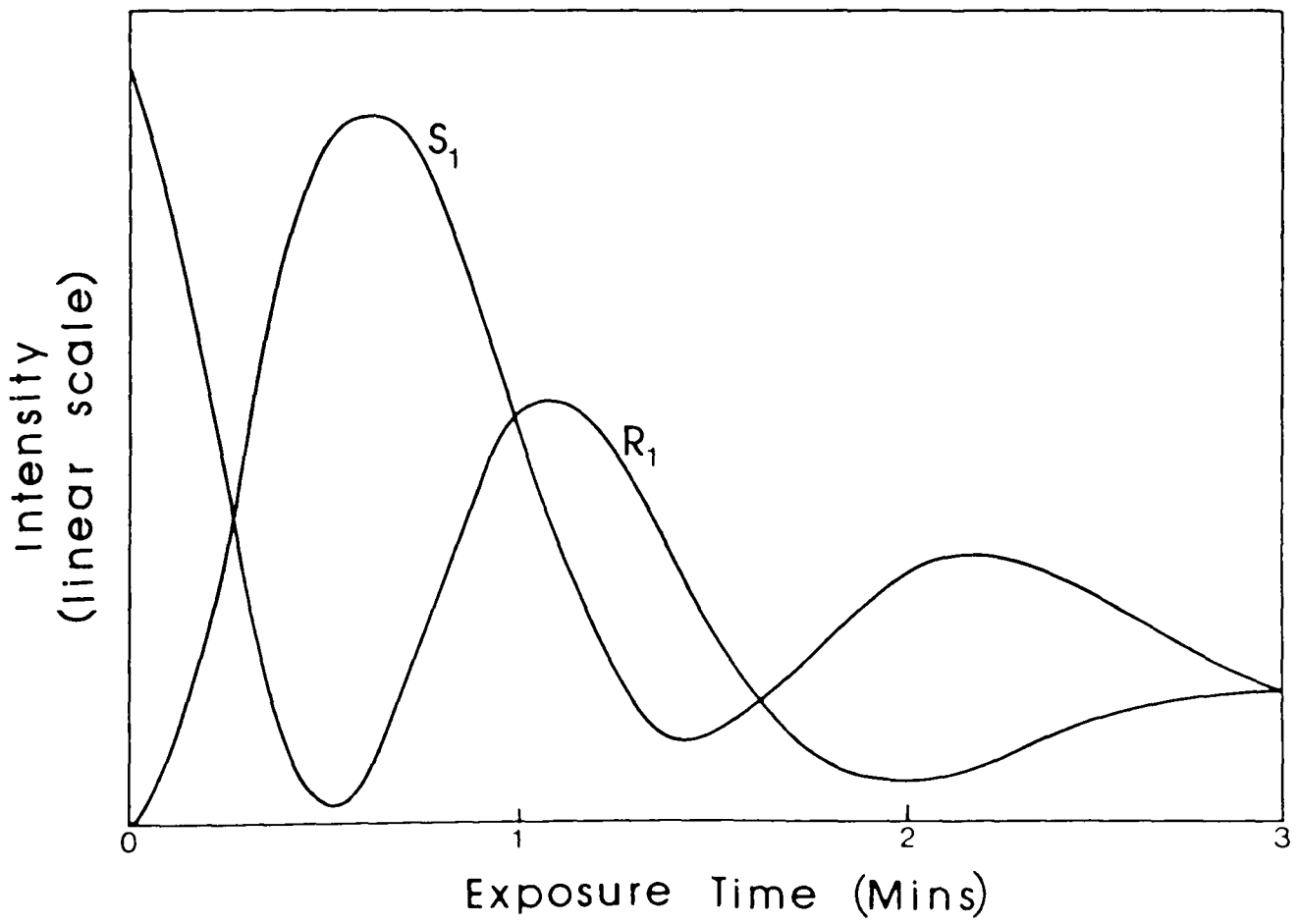

Fig 6.15: Time development of diffracted and transmitted beam (two separate exposures)

of the main recording beams. Good evidence for the presence of dynamic scattering has already been found in previous curves as beam attenuation. The oscillation rates confirmed this idea.

If the recording is assumed to be a latent process (see chapter five), the oscillation can be interpretated as a change in refractive index modulation. From equation (2.24), for polarisation normal to the plane of incidence, the diffraction efficiency η, will equal

$$\sin^2\left[\frac{(\kappa d)_G}{\cos(\psi_G)}\right] \qquad (6.27)$$

where κ is the coupling strength and d is the length of grating along the crystallographic y-axis (3mm). The increase in period with exposure time can then be attributed to either a saturation mechanism (see chapter five) or attenuation of the main recording beams. A good way to check that κ is monotonically increasing with exposure time is to stop the recording at different points and measure the IR efficiency of the filter. For a transmission geometry the diffracted intensity can decrease for increasing κ (called 'overcoupling'), whereas for a reflection grating, this is not possible. Experimental results, not given here, agreed with the hypothesis that the grating strength was always increasing.

According to this simple model, the maximum coupling at recording obtained was

$$\left[\frac{(\kappa d)_G}{\cos(\psi_G)}\right] \approx 2\pi \qquad (6.28)$$

From equation (4.3), since the r_{113} electro-optic tensor component, the refractive index n_{ord} and the internal electric field E are the same at both recording and replay,

$$\frac{(\kappa d)_R}{(kd)_G} = \frac{d_R}{d_G}\frac{\lambda_G}{\lambda_R}\frac{\tilde{n}^3_{ord}(\lambda_R)}{\tilde{n}^3_{ord}(\lambda_G)} \qquad (6.29)$$

Inserting typical values for these constants: $n_{ord}(\lambda_G) = 2{\cdot}33$, $n_{ord}(\lambda_R) = 2{\cdot}23$, $d_G = 3$ mm, $d_R = 4$ mm, $\lambda_G = 0{\cdot}514$ μm, $\lambda_R = 1{\cdot}152$ μm, and from table 6.1, $\cos(\psi_G) = 0{\cdot}9$, this model predicts that,

$$(\kappa d)_R \approx 0{\cdot}5\ (\kappa d)_G \approx 3 \qquad (6.30)$$

CHAPTER SEVEN

REPLAY

VII.1 INTRODUCTION

The objective of the replay experiment was to determine the diffraction efficiency and uniformity of the grating and to assess its performance as an IR filter. The results will highlight areas that need further investigation.

Since the primary role of this device is to act as a wavelength filter the obvious diagnostic test is to probe the grating with a tunable IR laser source. Two sources were considered: a colour-centre dye laser, or a temperature tuned, single mode semiconductor laser calibrated by a high resolution (0·1 Å or better) IR spectrometer. Unfortunately, this equipment was too expensive to acquire. Consequently, inferior, indirect methods had to be examined. These methods determined the response either by changing the incident angle of the probe beam, the temperature of the crystal, or by applying external electric fields. Temperature tuning is slow [43], whereas electro-optic tuning requires high fields and can induce non-uniform refractive index variations due to 'fringing' effects at the edges of the electrodes. The other alternative was to rotate the crystal. This was the method chosen for all laboratory measurements.

This method has limitations because the section of grating being probed will continually change as the grating is turned. If the grating is non-uniform, the off-Bragg response will give a misleading answer. The effect can be minimised by recording a grating designed to replay at an angle a few degrees away from normal incidence to the grating. The angular selectivity of the grating is then considerably greater (see Fig

2.6), the limits for the angle scan will be less, and the section investigated becomes restricted. There are two additional advantages associated with the off-normal geometry which simplify comparison between theory and experiment. Firstly, the off-Bragg side-lobe distribution will be almost symmetrically disposed about the central peak, and secondly, the selectivity of the grating will be less dependent on the exact angle of beam incidence.

The crystal was usually rotated about its crystallographic Y-axis, with the grating K-vector remaining in a horizontal plane (see Fig 7.1). The reasons for choosing this geometry are discussed below.

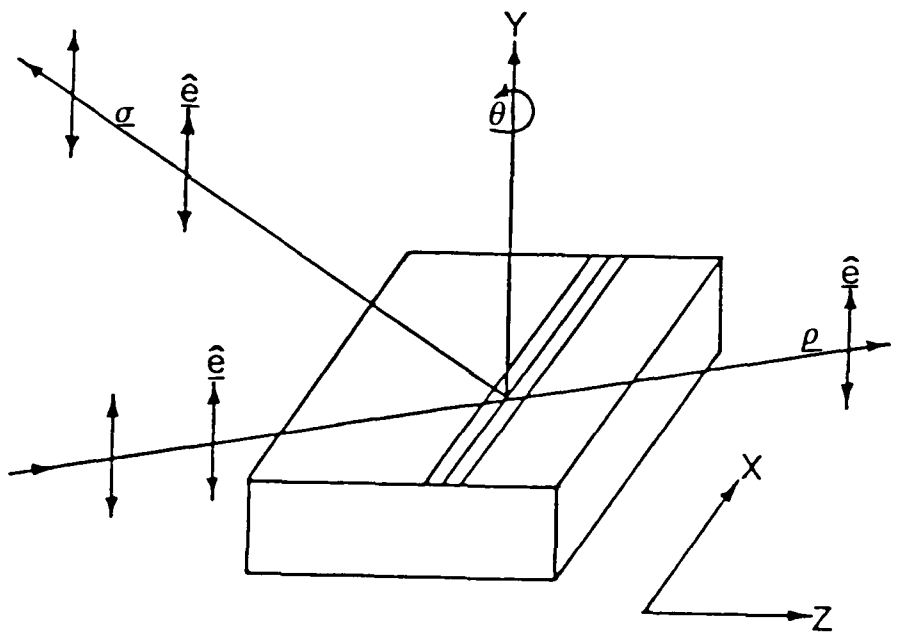

Fig 7.1: Standard orientation of crystal in replay apparatus

As mentioned in section VI.5, the modulation strength inside the crystal is expected to be non-uniform, being highest near the incident recording face where the light intensity is a maximum, and then decreasing towards the exit face. At replay, however, the laser beam passes through the crystal in a different direction. If the replay beam is narrow in the Y-dimension, it can probe a thin planar cross-section of the grating, a fixed distance from the recording face. The measured modulation strength profile should then be nearly uniform. The other advantage of this configuration, as discussed in appendix B.2, is the ability to probe a grating with a well defined length. A weakness with

the scaling geometry is the production of a grating with complicated shape, where the recording beams overlap. This technique is one way to overcome the problem without physically cutting the ends off the grating; optical erasure, introduced later, is another.

In conclusion, the quality of the grating should be superior at IR compared with visible wavelengths. Furthermore, by moving the crystal in the Y-direction relative to the IR beam, a depth profile of the recorded grating strength can be directly obtained; whereas, if the grating is only tested at its recording wavelength, this information has to be derived from a complicated theoretical model.

So far the anisotropic properties of lithium niobate have been totally neglected. Referring to appendix D, this is only possible if a), the crystal is probed along its axis of symmetry (the c-axis), when the ordinary and extra-ordinary index components degenerate into one value, or b), the polarisation of the IR light is perpendicular to the c-axis, when the apparent index is always the ordinary value. Option a) is the expected configuration for the device in its final operating environment, whereas option b) will be adopted for most of the diagnostic tests.

VII.2 EQUIPMENT

A diagram showing a general layout of the replay apparatus is given in Fig 7.2. The rest of this section describes in detail the various optical and mechanical components.

The particular commercial IR laser chosen for this experiment was a 1 mW Spectra Physics '120S', where the letter 'S' denotes the 'stabilite' option. The stable output, small pointing error (maximum change < 10^{-3} degrees) and the long life of the '120S' made it extremely useful for an

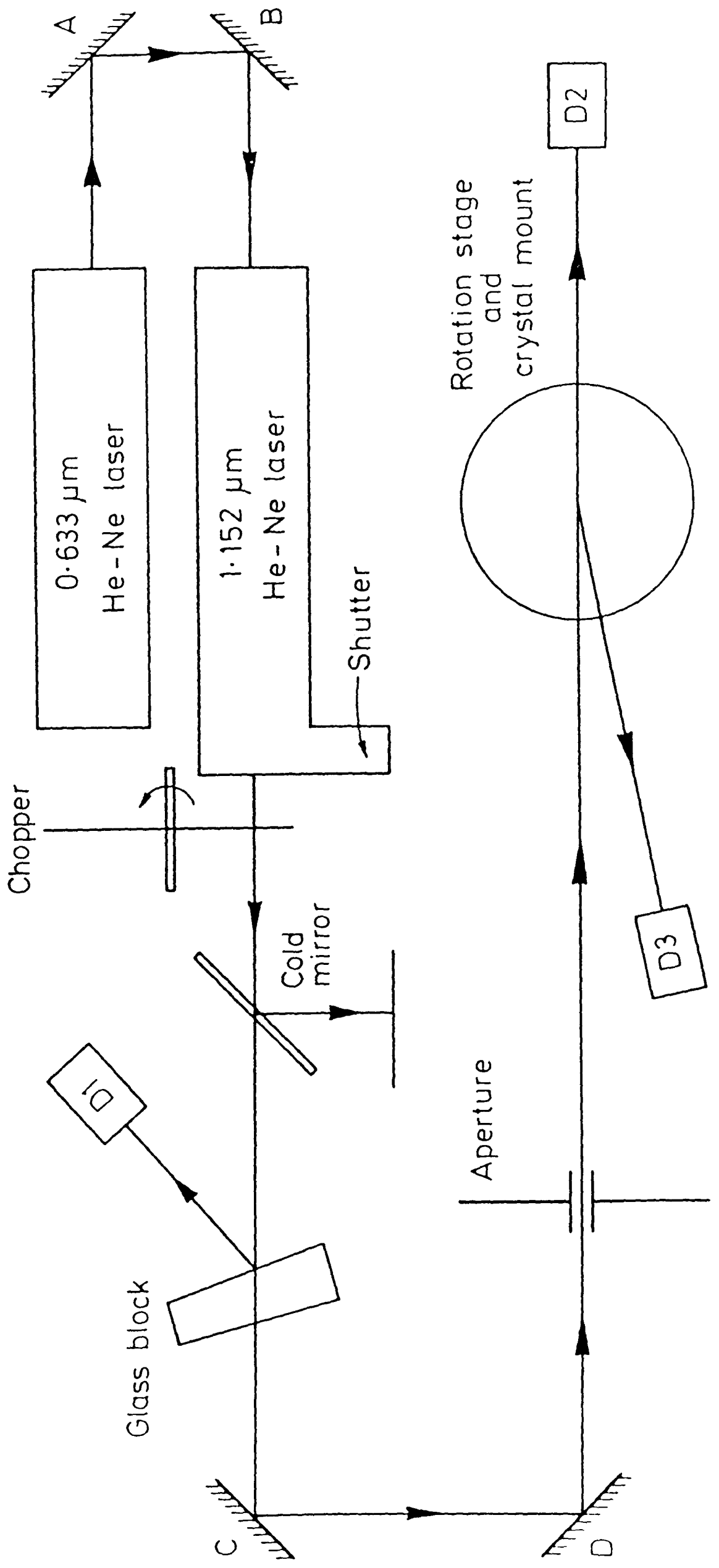

Fig 7.2: Diagram of the replay apparatus

application where highly reproducible results were desired. Furthermore, the coherence length of the '120S', quoted by the manufacturers as about 30 cm, is substantially greater than double the optical path length of the grating (about 1 cm). The resolution of the grating will therefore not be limited by the spectrum of modes generated by the laser.

The output from the laser was measured using a phase sensitive lock-in amplifier, a commercial Scitec chopper to periodically block the incident beam and a germanium photodiode as the detector. Germanium has an unrivalled optical sensitivity in the 1-2 μm wavelength range and AC detection allows excellent noise rejection. A cold mirror filter (90% rejection of wavelengths < 0·8 μm) was placed in front of the laser to attenuate the incoherent visible discharge light.

After a 'warm-up' period of two hours the laser intensity drifted by less than 3 percent. To further reduce this fluctuation the measured signal was divided or 'normalised' by a constant fraction split from the main beam. An AD533 analogue divider IC performed the real-time division. In practice, due to the time constants of the lock-in amplifiers, only the long term variations of the signal could be removed. Nevertheless, this was sufficient to compare readings measured over a period of hours, or even days.

Two methods were used to observe the path of the IR light. A visible He-Ne laser beam, was aligned coaxially with its IR He-Ne counterpart (as shown in Fig 7.2). Implementation is straightforward, because the two end mirrors of the IR laser are transparent to visible wavelengths. The technique became a standard way to orientate the crystal by back reflection. Additionally, an IR videcon camera, having a slow response time of a few seconds, was occasionally used to check for the presence of any spurious beams.

A nylon screw, attached to a retaining plate, lightly clamped the crystal in its mounting jig while keeping the pressure evenly

distributed. A pair of translation stages, accurate to 0·01 mm, allowed X-Y movement of the jig relative to the probe beam. Two rotation stages, one controlled by a stepper-motor (horizontal plane), the other under manual control (vertical plane), held the whole assembly as shown below in Fig 7.3.

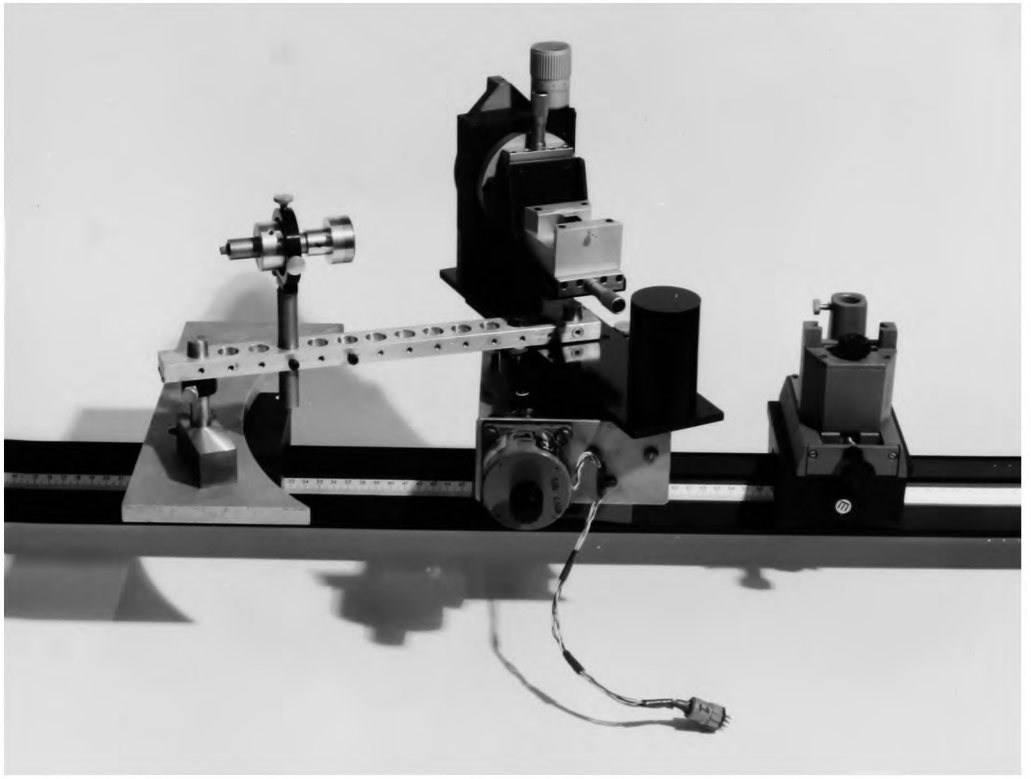

Fig 7.3 Replay apparatus, showing from left to right; detector intercepting the diffracted beam, positioning equipment, mount for the detector when the transmitted beam is being measured.

The infra-red detector measuring either the transmitted or diffracted beam (D2 or D3 in Fig 7.2) was designed to need a minimal amount of alignment. If manual adjustment between readings could be avoided the speed of data gathering can be dramatically increased. This was an important goal, since the unfixed grating only had a limited lifetime. Various hybrid combinations were considered: detector and lens, detector and diffusing screen, or large area detector. The uniformity across the active region of a large area germanium photo-diode cannot be guaranteed and the detector noise will also be substantially greater. Placing the photo-diode at the focal point of a lens will make the measured signal insensitive to lateral movement of the beam. A diffusing screen was found to be the best compromise by averaging out any

variations across the beam and being relatively insensitive to beam position. Furthermore, the large attenuation of the beam was acceptable. The addition of a circular aperture screened out any spurious beams reflected from the slanted Z-faces of the crystal. The design was very successful for the transmitted beam. The diffracted beam, however, rotating through an angle 2θ', had to be measured by manually moving the detector between each reading. To simplify the alignment procedure, the detector was mounted on a radial arm.

A BASIC programme on a 380-Z computer controlled the stepper-motor driven rotation stage, turning the crystal about a vertical axis (the Y-axis). It also automatically converted the analogue electronic signal derived from the lock-in amplifier into digital form via an A-D board, with a resolution of about 1%. A simple form of experimental verification was introduced by programming the computer to take a series of readings, separated by a short time interval (typically 1 second). A reading was only stored if two successive readings agreed to within a predetermined tolerance. In this way a large number of data points could be recorded on a floppy disc in a relatively short space of time.

Two sets of jaws, vertical and horizontal, partially blocked the beam produced by the laser. The intensity half-width of the IR beam after propagating about 0.5 metres between the mirrors was about 4 mm. The apertures reduced the dimensions of this beam to about 2 mm in the horizontal and 1 mm in the vertical direction. According to appendix B.1, for horizontal slit widths $\geq$ 1 mm the angular width of the Bragg response will not be significantly increased by instrumental broadening.

VII.3 EXPERIMENTAL RESULTS

Using the visible He-Ne beam the crystal was moved into approximately the correct position. The dip in the transmitted beam

established the position of the Bragg angle. A standard recording angle was used for all these experiments and a number of diagnostic tests were undertaken to establish the important characteristics of the grating. The main concern was to devise tests which changed only one parameter of the grating. For example, if the +1 diffraction order is measured instead of the -1 order, (see chapter two), the crystal has to be rotated through a relatively large angle (nearly 20 degrees in this case). The beam will then probe a different part of the grating and consequently, the two sets of results are not necessarily comparable.

The first set of experiments were designed to test the performance of the replay apparatus. To obtain reliable results, a) the rotation stage must be sufficiently accurate, b) the detection system must be capable of providing repeatable readings and c) the angular position of the Bragg interaction must not be significantly affected by changes in ambient temperature. Fig 7.4 are two curves taken in succession. The dips are in good alignment and the traces are generally very similar.

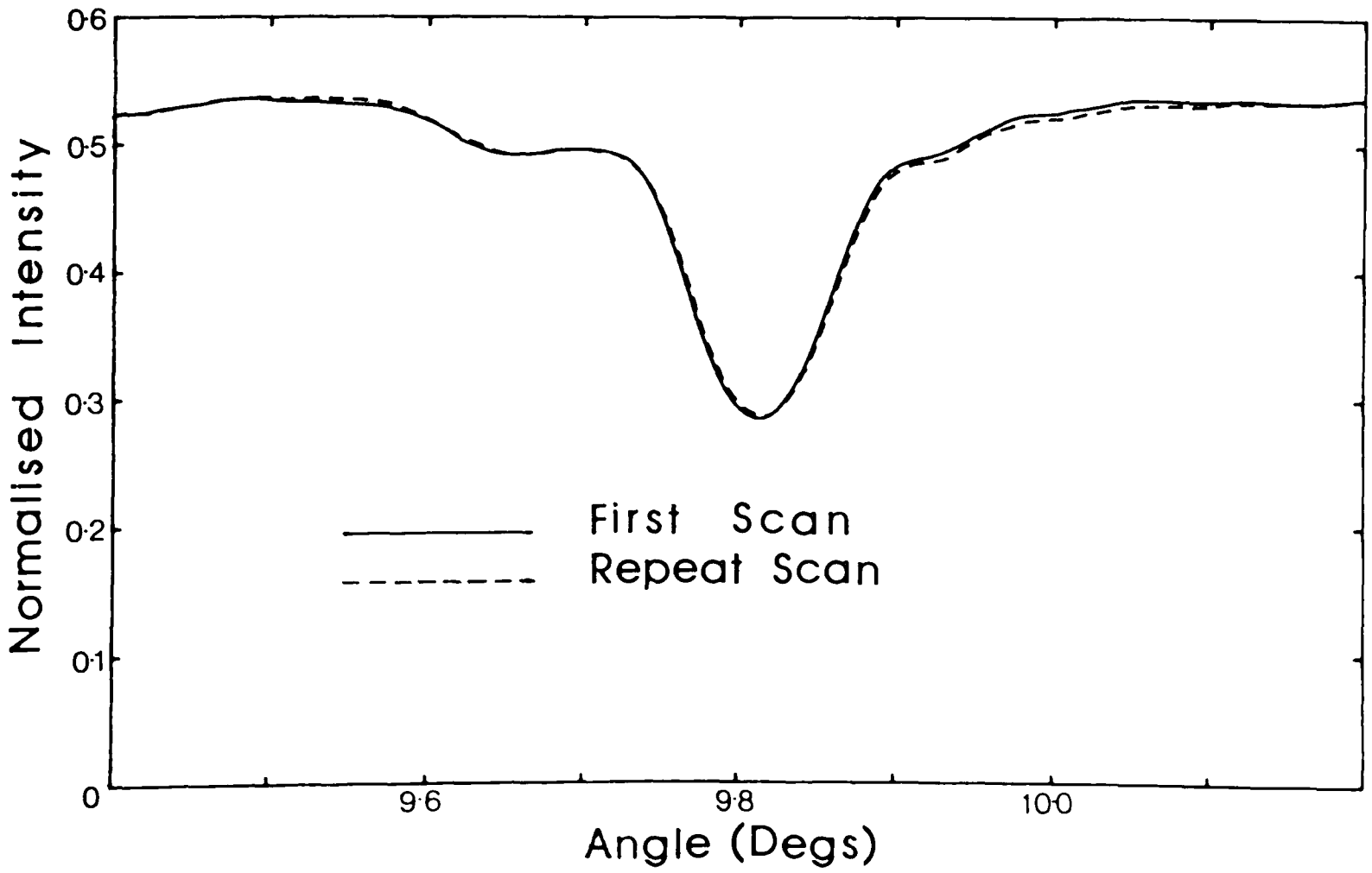

Fig 7.4: Two curves measured in succession

Figures 7.5 and 7.6 demonstrate the effect of temperature on the position of the Bragg angle for both +1 and -1 orders.

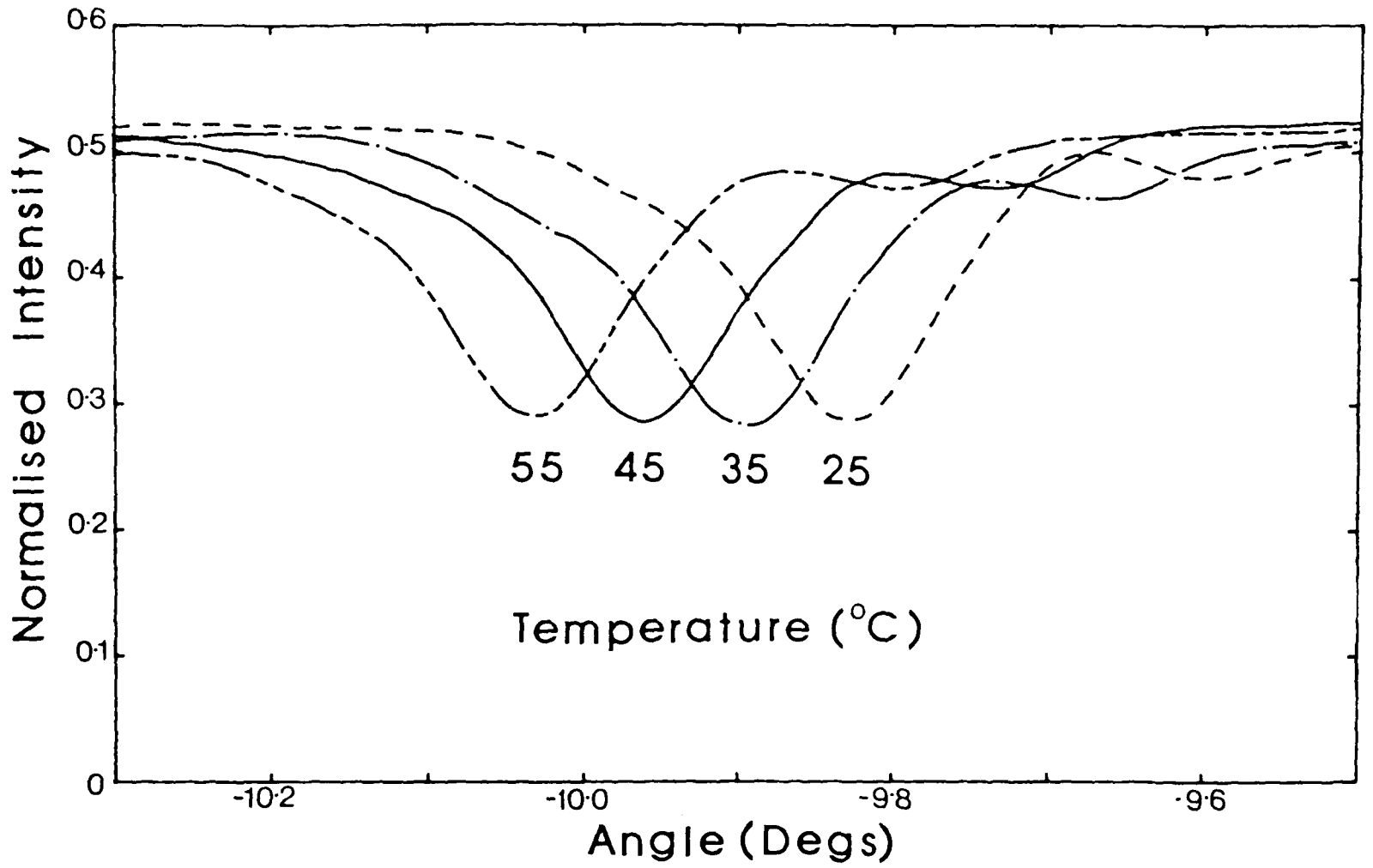

Fig 7.5: Temperature dependence of the +1 order (crystal I)

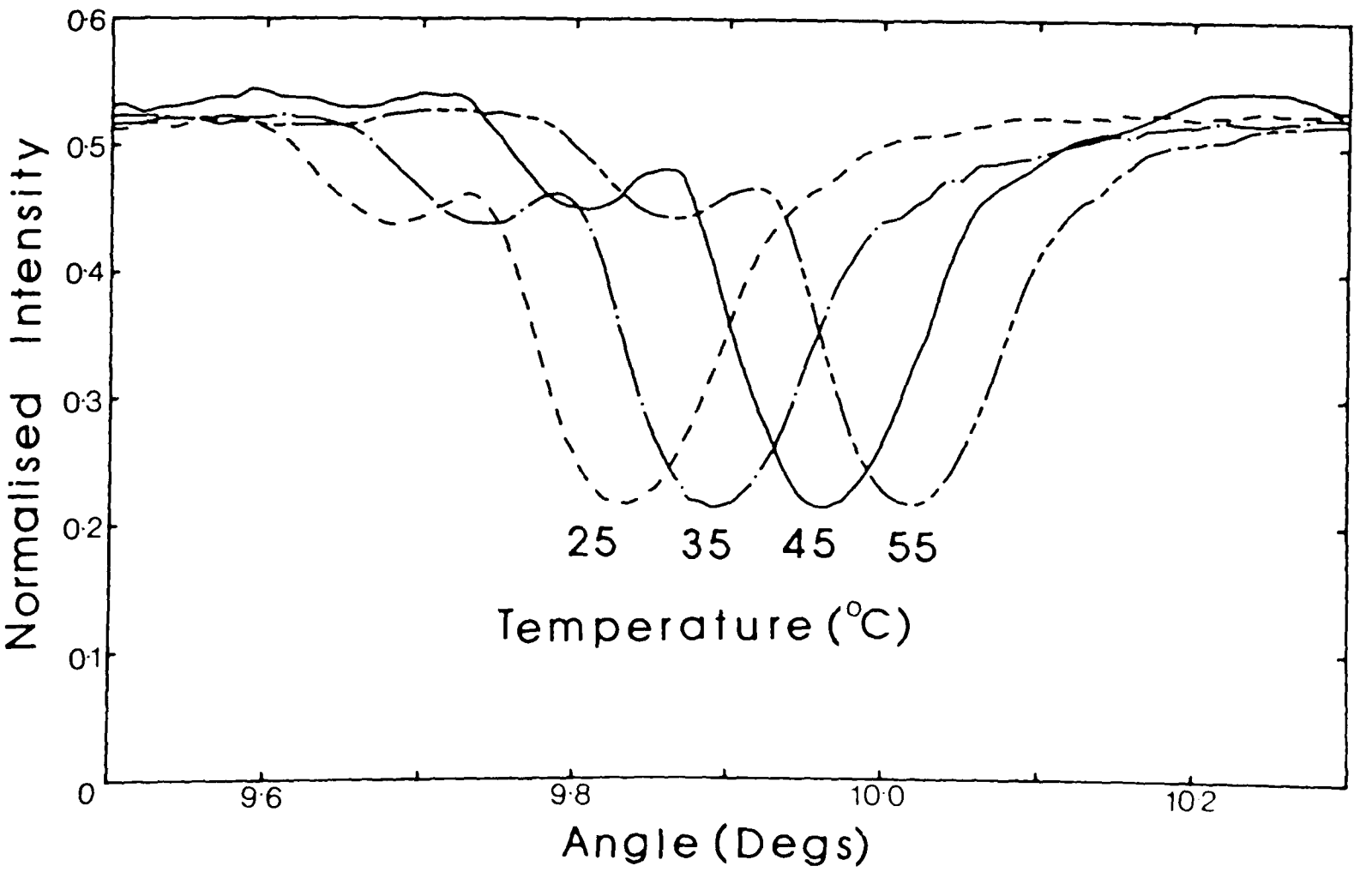

Fig 7.6: Temperature dependence of the -1 order (crystal I)

Crystal I was placed in an adapted commercial oven, capable of keeping the temperature constant to about 0·1 degree. Note the difference in grating efficiency between the two sets of curves.

From equation (2.1),

$$\cos(\theta_o) = \frac{\lambda_R}{2\tilde{n}\Lambda} = \frac{\lambda_R}{2\tilde{n}d}\left[\frac{d}{\Lambda}\right] \qquad (7.1)$$

Making the approximation $\theta_o >> \Delta\theta_t$, where $\Delta\theta_t$ is the thermally induced change in Bragg angle,

$$\Delta\theta_t = \left[\frac{\Delta(\tilde{n}d)}{(\tilde{n}d)}\right] \times \left[\frac{\lambda_R}{2\,\tilde{n}\Lambda\,\sin(\theta_o)}\right] \qquad (7.2)$$

From equation (2.36) assuming $\Delta\theta_{1/2} << \theta_o$,

$$\Delta\theta_t = \Delta\theta_{1/2} \times \left[\frac{\Delta(\tilde{n}d)}{(\tilde{n}d)}\right] \times \left[\frac{2\,\tilde{n}d\,\cos(\theta_o)}{\lambda_R}\right] \qquad (7.3)$$

where (see section VI.8),

$$\left[\frac{\Delta(\tilde{n}d)}{(\tilde{n}d)}\right] = \left[\alpha_c + \delta_c\right]\Delta T \qquad (7.4)$$

Heating the crystal will increase its optical path length and according to equation (7.3) increase the Bragg angle θ_o. It was confirmed by the experimental results. Inserting typical values into equation (7.3) λ_R = 1·152 μm, d = 4 mm, $\tilde{n}$ = 2·23, θ_o = 4 degrees, the condition $\Delta\theta_t = \Delta\theta_{1/2}$ will occur when,

$$\underline{\Delta T \approx 16\ ^{o}C} \qquad (7.5)$$

Adequate temperature control can therefore be achieved by keeping all the equipment in an air-conditioned room capable of keeping ambient temperature variations less than 1°C.

VII.3.1 Comparison between crystals

A major problem encountered with these experiments was the lack of consistent results between different crystals. Shown in Fig 7.7 is a typical set of angle scans for crystal II. The normal Bragg response has become severely distorted due to the presence of a second dip. A considerable number of angle scan measurements were made to explain this effect, but no general trends could be established. For example, this type of response could not be fitted to the chirped grating model in chapter two. The result was unexpected because crystal II was specially selected to have better optical quality than crystal I (see appendix E). The remainder of the experimental results in this chapter are derived from gratings recorded in crystal I, associated with more understandable characteristics.

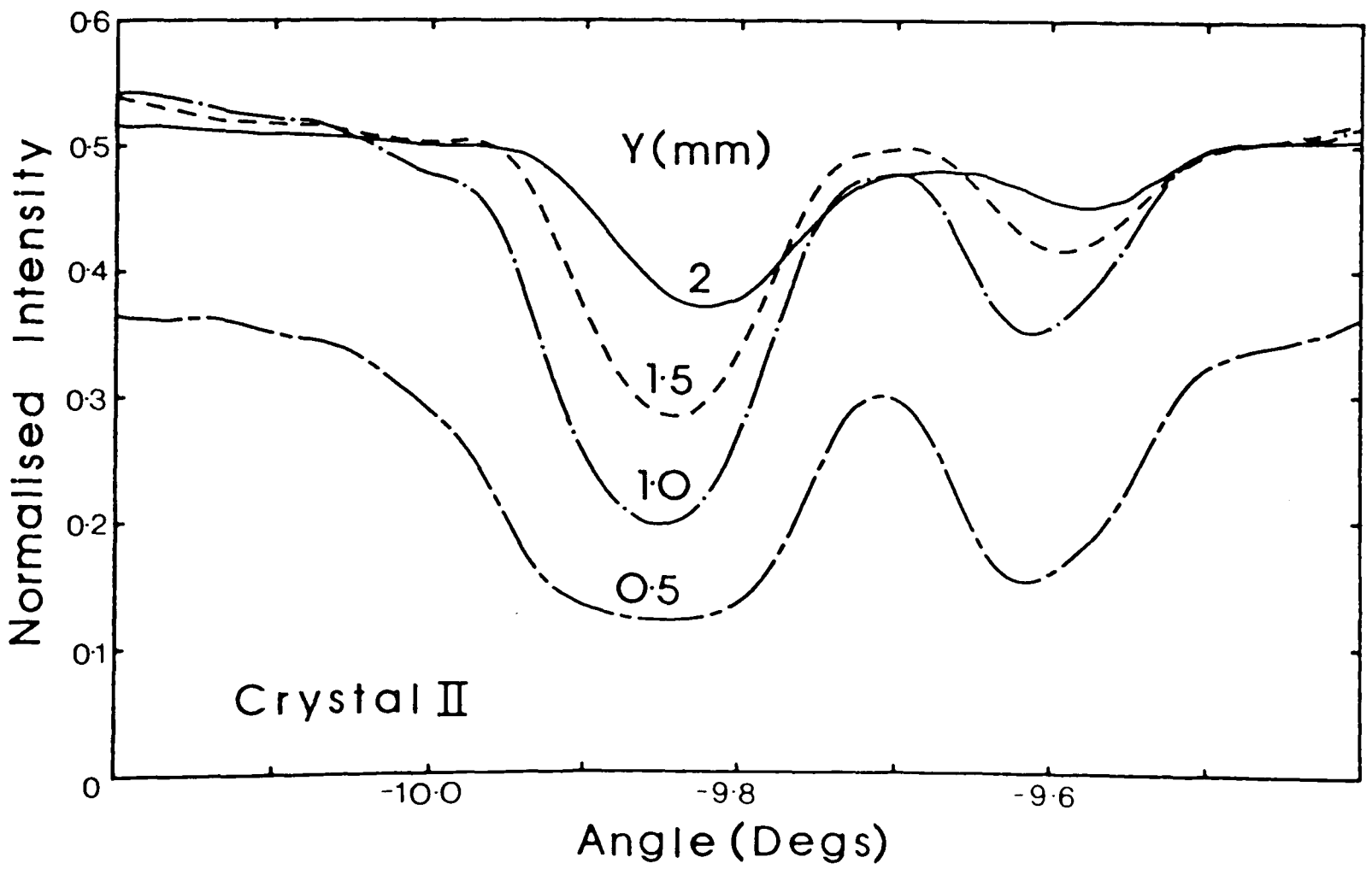

Fig 7.7: Function of Y co-ordinate (crystal II)

VII.3.2 Effective grating length

A typical grating interaction in crystal I was fitted to the coupled-wave numerical model established in chapter two including a small amount of absorption (the infra-red absorption band centred at about 1·2 μm as shown in Fig 7.8 is caused [19] by an Fe^{2+} optical transition). Reasonable agreement between theory and experiment was obtained by assuming the grating to have an effective length of 4 mm (as shown in Fig 7.9). The presence of absorption implies that power conservation will not be satisfied when the theoretical transmitted and diffracted components are added together.

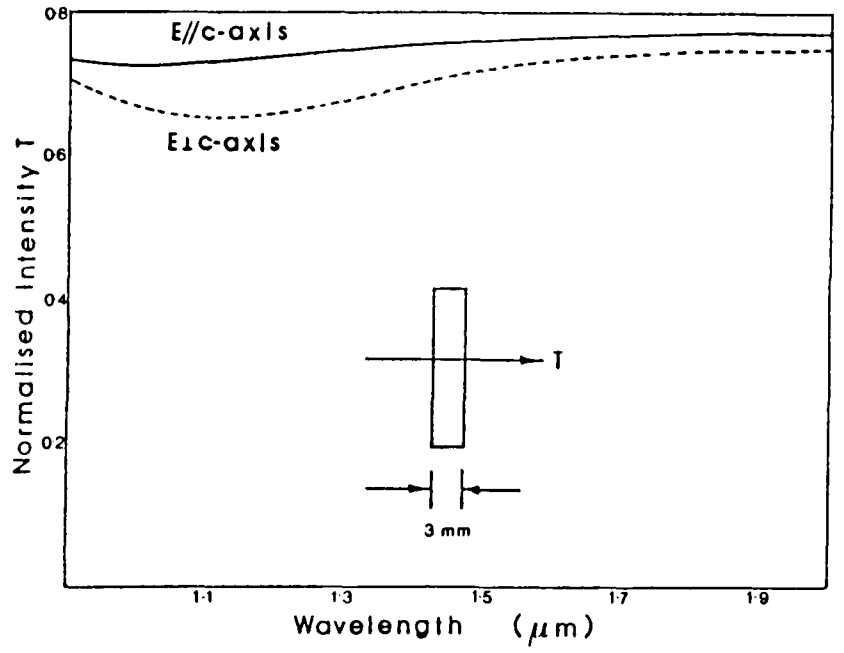

Fig 7.8: Infra-red transmission of crystal I

A strong diffracted beam was essential for the grating to operate as a band pass filter. The presence of a dip in the transmitted beam, was insufficient evidence to prove that such a diffracted beam existed, since there was always another explanation: noise gratings. A noise grating will attenuate the transmitted beam, but, unlike a filter, diffract the light in all directions. As shown in these results, however, most of the intensity lost from the transmitted beam was transferred to the measured diffracted beam.

Comparing theory and experiment, it is noticeable that the expected side-lobe structure of the Bragg interaction is absent. This is a drawback, and means that only a limited amount of information can be obtained about the grating profile. As discussed in appendix B.3, the replay geometry is partly responsible for this effect, but equally, it could be caused by a spatial variation of modulation strength inside the crystal. The latter possibility will reduce the high frequency Fourier components of the grating which in the kinematic limit are responsible for side-lobes (an example of apodization).

In Fig 7.9 the structure present in the transmitted beam is duplicated in the diffracted beam. It is evidence that the additional peak on the right is not a spurious effect caused by internal reflections. Etalon effects can be neglected, since the ends of the crystal were deliberably slanted by a few degrees.

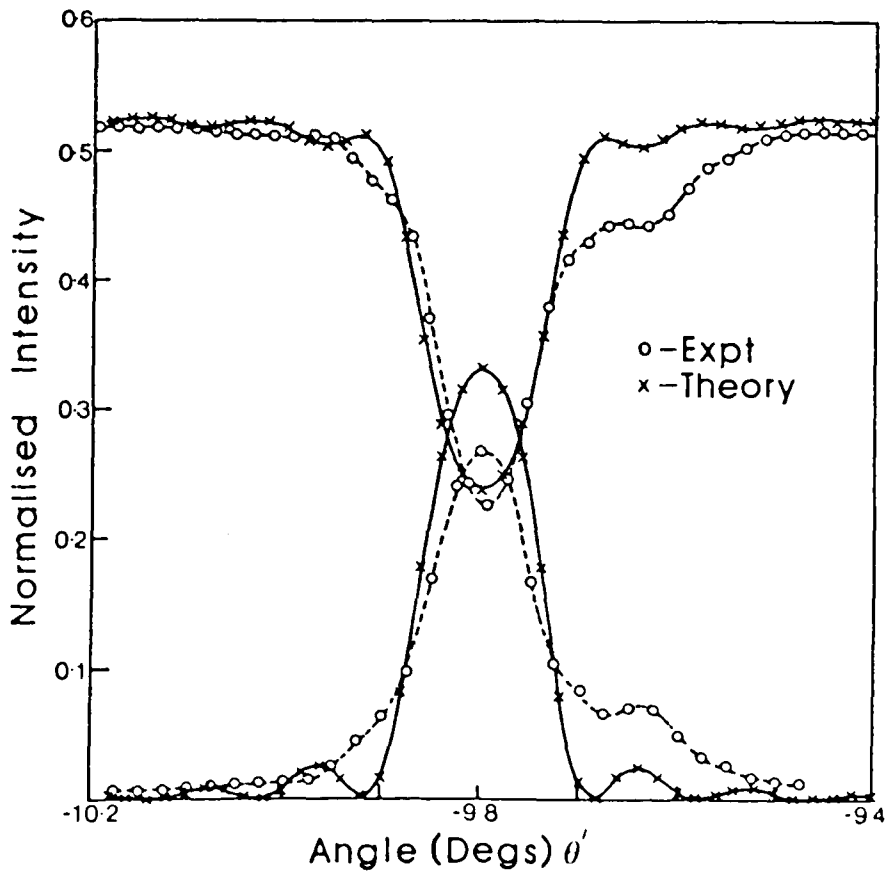

Fig 7.9: Agreement between theory and experiment for both transmitted and diffracted beams in crystal I

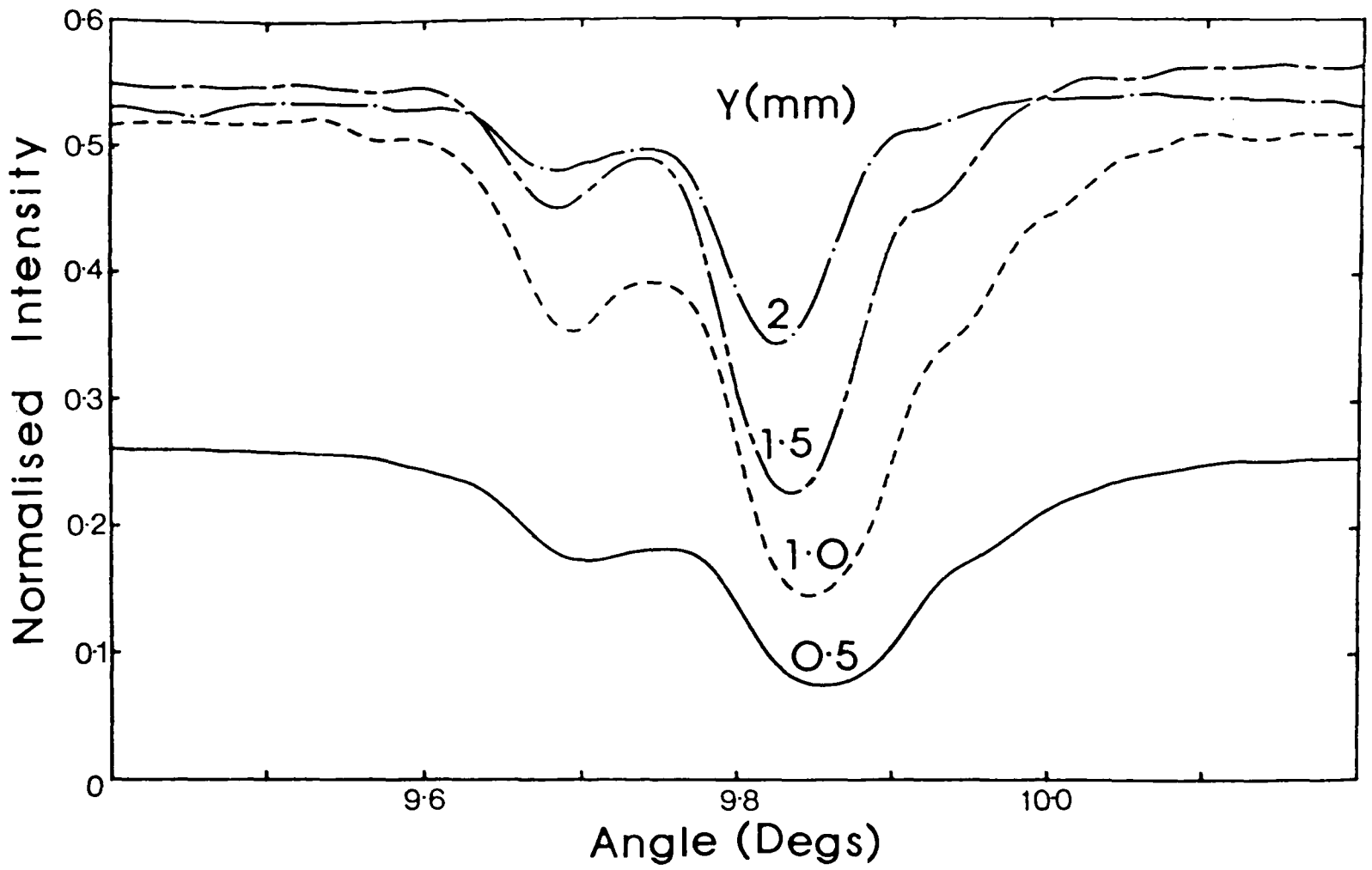

Fig 7.10: Function of Y co-ordinate (crystal I)

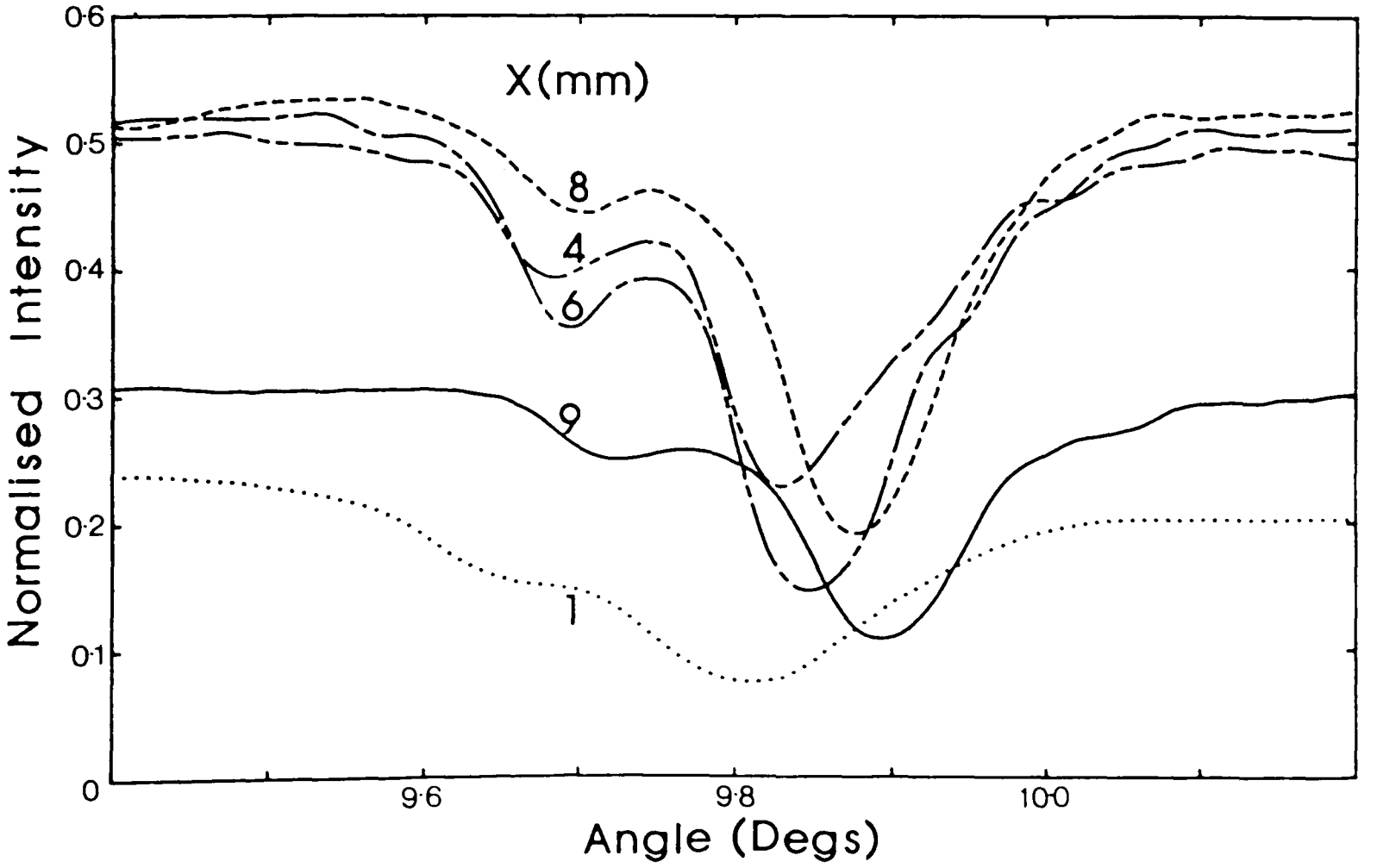

Fig 7.11: Function of X co-ordinate (crystal I)

VII.3.3 Non-uniformities

The experimental results shown in Fig 7.10 and Fig 7.11 are angle scans of crystal I in a horizontal plane through one of the Bragg interactions. The set of curves in Fig 7.10 were generated by varying the Y co-ordinate of the crystal, where Y = 0 corresponds to the position of the crystal face nearest the recording beams. Note the rapid decrease in transmitted intensity when the edges of the crystal restrict the diameter of the probe beam. The most significant feature is the change in grating efficiency, in accordance with the predictions of section VI.5. Fig 7.11 shows a set of curves generated by varying the X co-ordinate, where X = 0 corresponds to one end of the crystal. There is evidence of non-uniformity, though the explanation is unclear. The complex structure follows a similar pattern independent of position within the crystal; consequently, it is probably not caused by boundary effects.

Fig 7.12 and Fig 7.13 shows the gradual decay of the same unfixed grating when left in the dark over a period of two weeks. The grating efficiency at two different points in the crystal, X = 6 mm and X = 9 mm, were monitored. If the variation in Bragg angle is due to photo-induced changes in the bulk refractive index, it should disappear at the same rate as the grating modulation (since the relaxation time τ_e is independent of period). No such improvement, however, was observed.

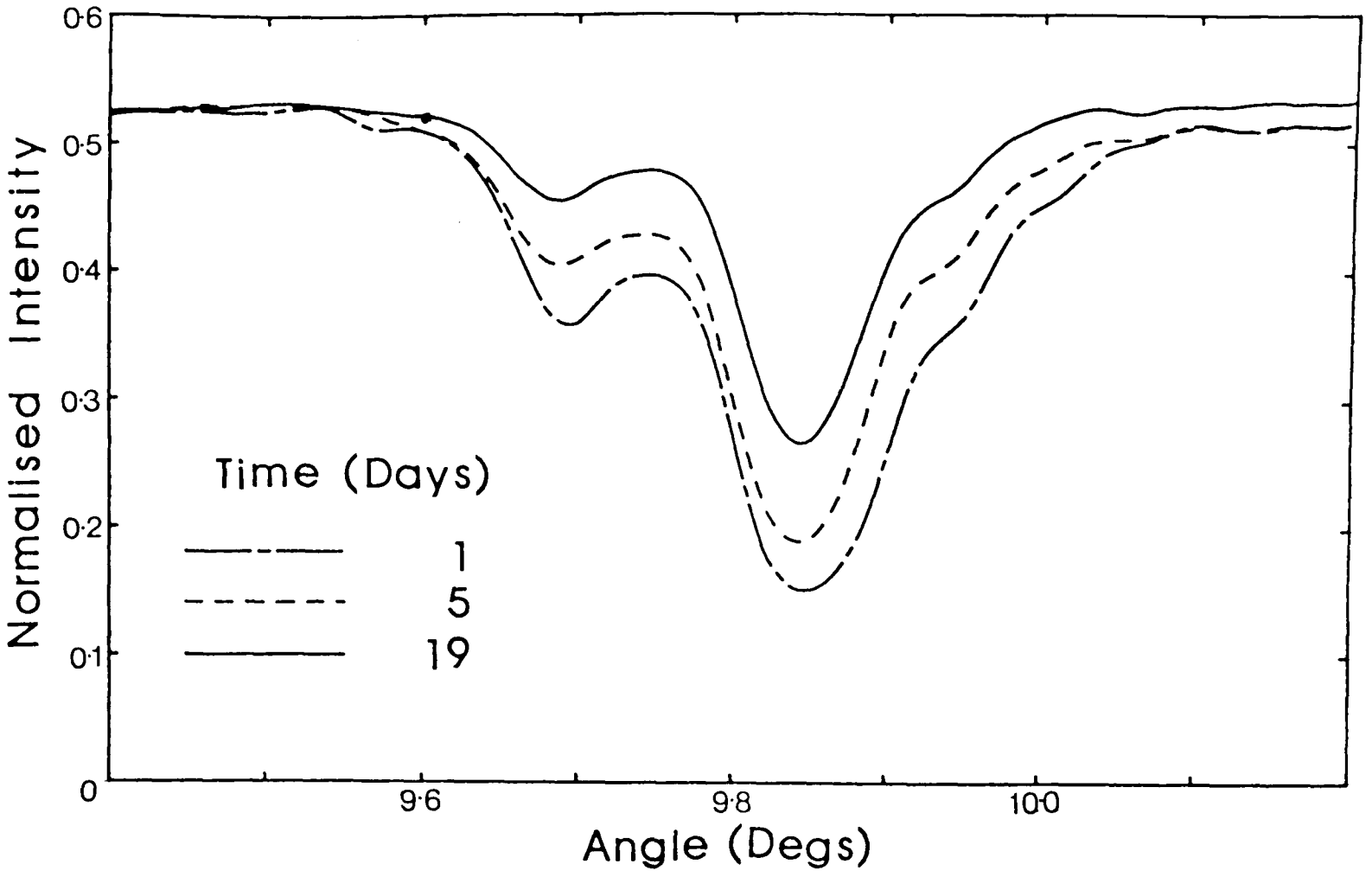

Fig 7.12: Decay of grating in the dark at the point X = 6 mm

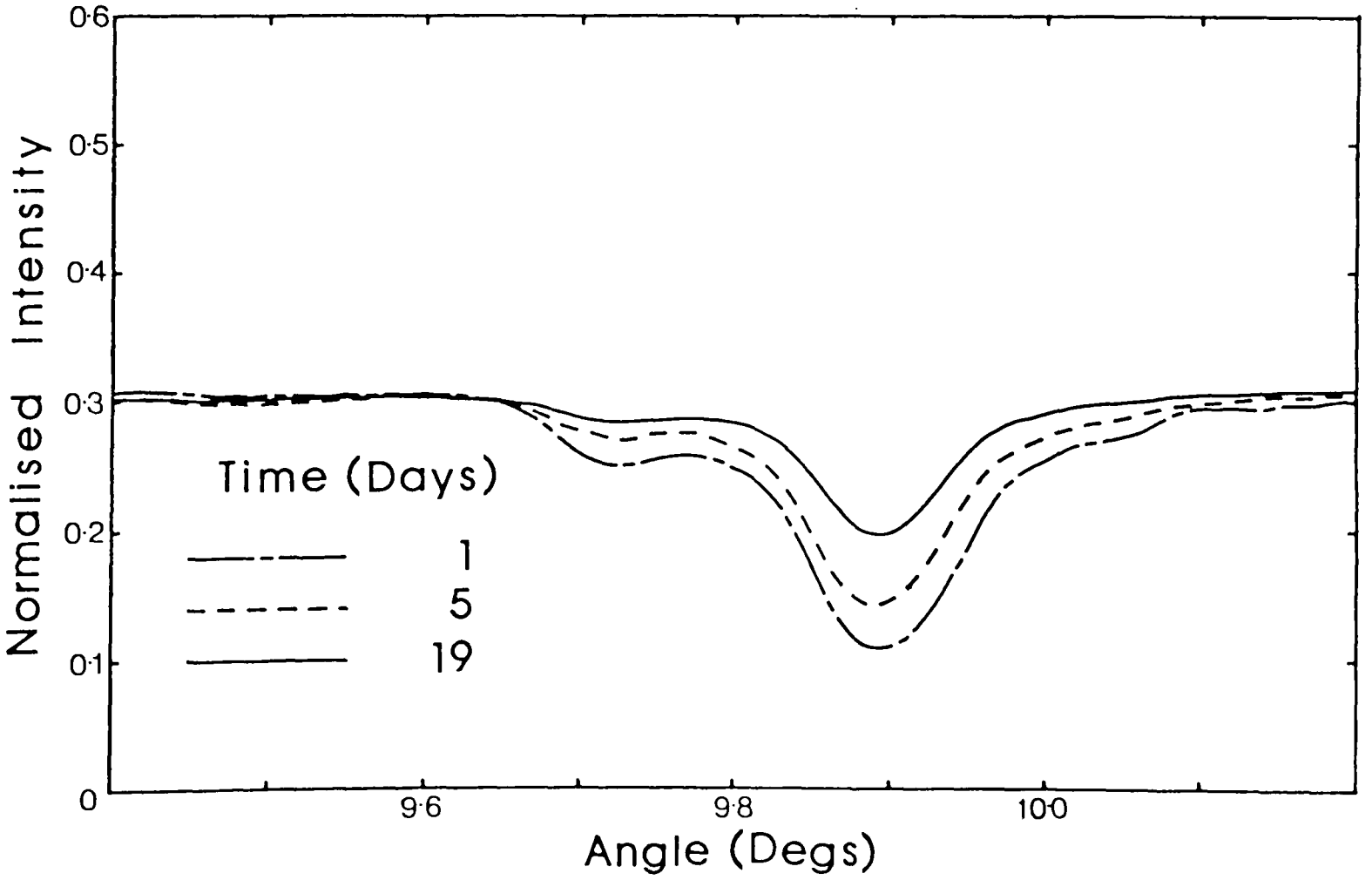

Fig 7.13: Decay of grating in the dark at the point X = 9 mm

VII.3.4 Polarisation

As discussed in appendix D the other polarisation state of the birefringent crystal can be detected by rotating the electric field vector of the incident beam. Polarisation dependence is a useful property of the grating to measure because in principle it is independent of propagation direction. In this experiment an IR polaroid (plastic laminated type HR) intercepted the beam just before the crystal. The polaroid was rotated to provide three polarisation angles: vertical, 45° and nearly horizontal (exact horizontal polarisation could not be achieved since the beam was originally vertically polarised). As shown below, the two interactions were clearly observable. Furthermore, their relative positions agreed moderately well with theory (for $\underline{K}$ // c-axis). The discrepancy in Bragg angles between the three curves was probably caused by the polaroid behaving like a prism and deflecting the beam.

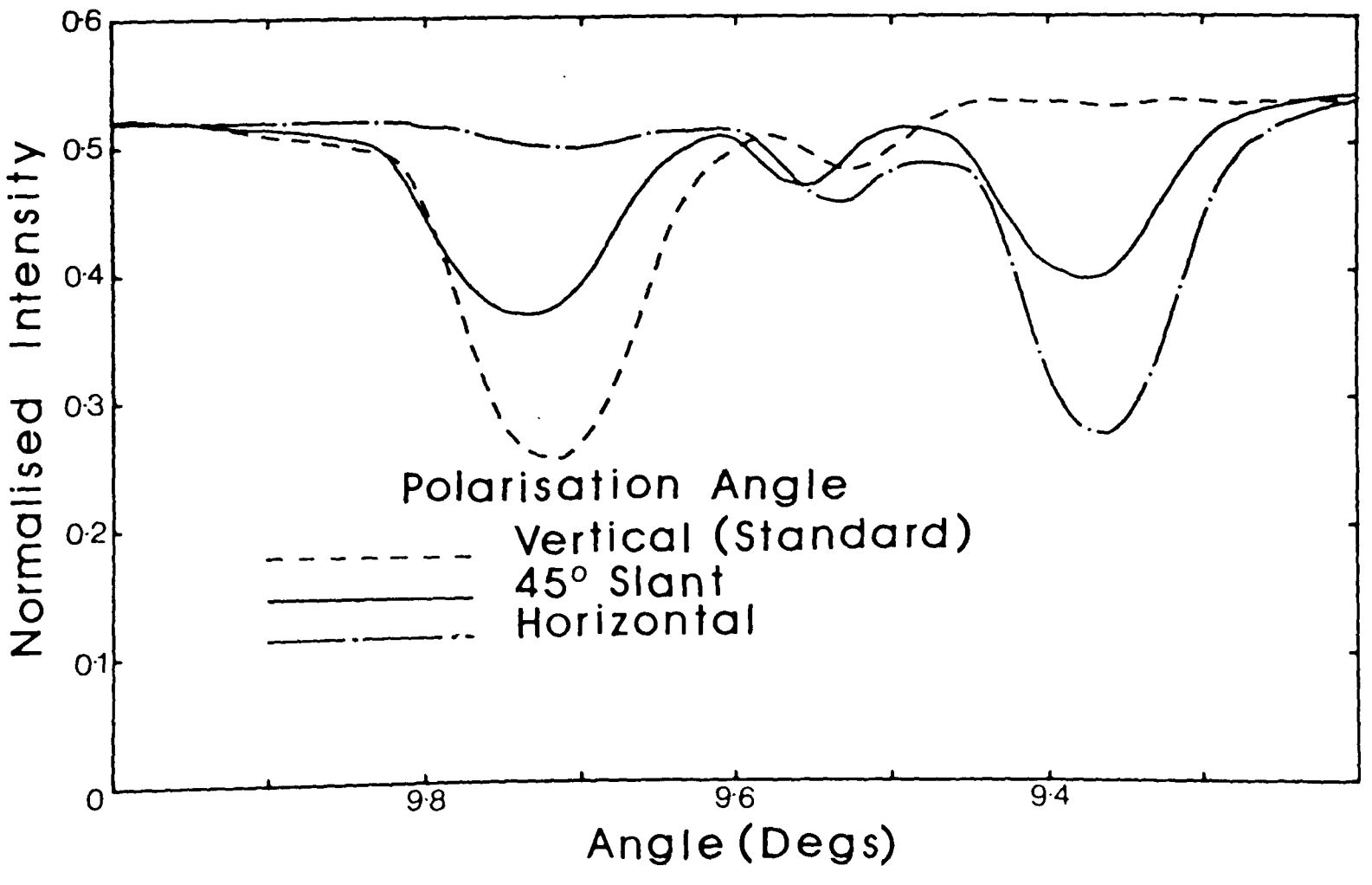

Fig 7.14: Function of polarisation angle

VII.3.5 Optical bleaching

A limited control over the grating profile was possible by illuminating the unfixed grating with incoherent light. This feature provided the opportunity to erase various regions of the grating inside the crystal. Before this technique can work reliably, however, a number of practical difficulties have to be overcome. The principle of the experiment was to expose the crystal to an intense collimated beam of visible light projected through a lithographic mask.

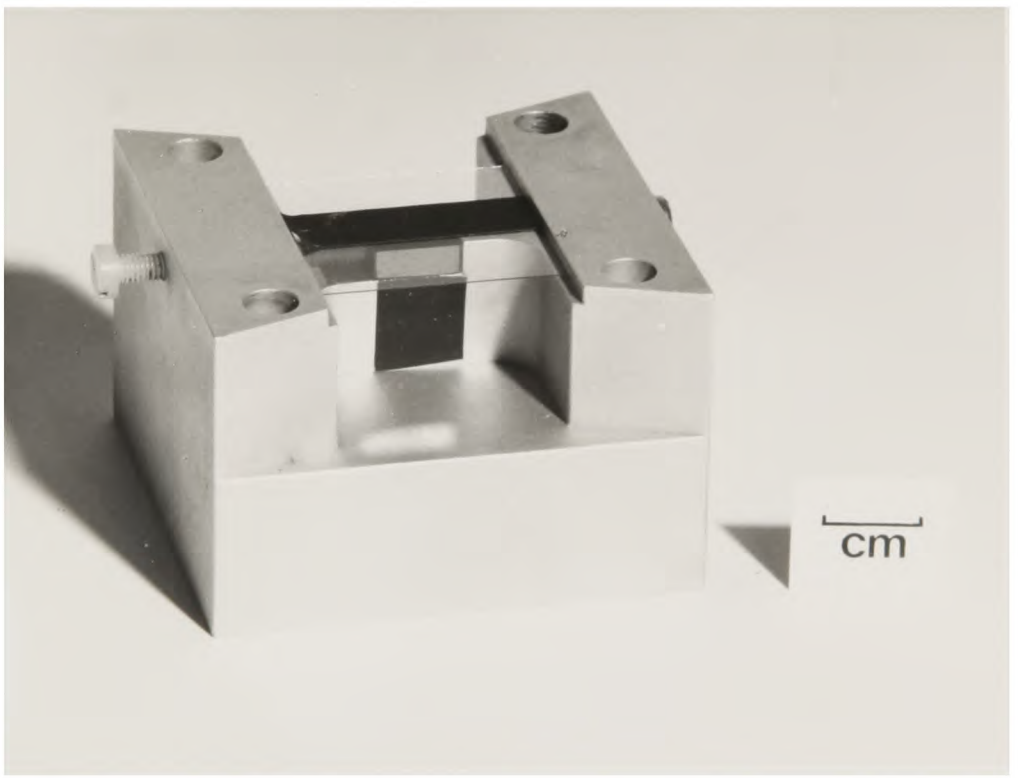

Fig 7.15: Crystal mount

The mask consisted of black circuit-tape in various widths accurate to 0.05 mm, mounted on microscope slides. The definition of the projected pattern depended upon the parallelism of the beam. Using a 100 W Zenon arc lamp the limiting factor was found to be the finite size of the source. Preliminary experiments predicted a blurred edge at least 0.07 mm wide after the beam had passed through the 3 mm thick crystal. Scattering and reflections at the surfaces of the crystal will also degrade the achievable resolution. Careful cleaning of the crystal and a black background, however, alleviated this problem. To avoid spurious

thermal effects, a heat filter was placed in front of the lamp and the crystal was allowed to reach thermal equilibrium before measuring the angular response.

A serious complication was the presence of a photo-induced bulk change in refractive index as described in chapter four. The phenomena was clearly observable by imaging an edge onto the crystal. The change in light intensity at the boundary produced a distinct line inside the crystal, initially mistaken for a crack, due to the formation of a refractive step. After a few hours of uniform illumination, however, this feature disappeared.

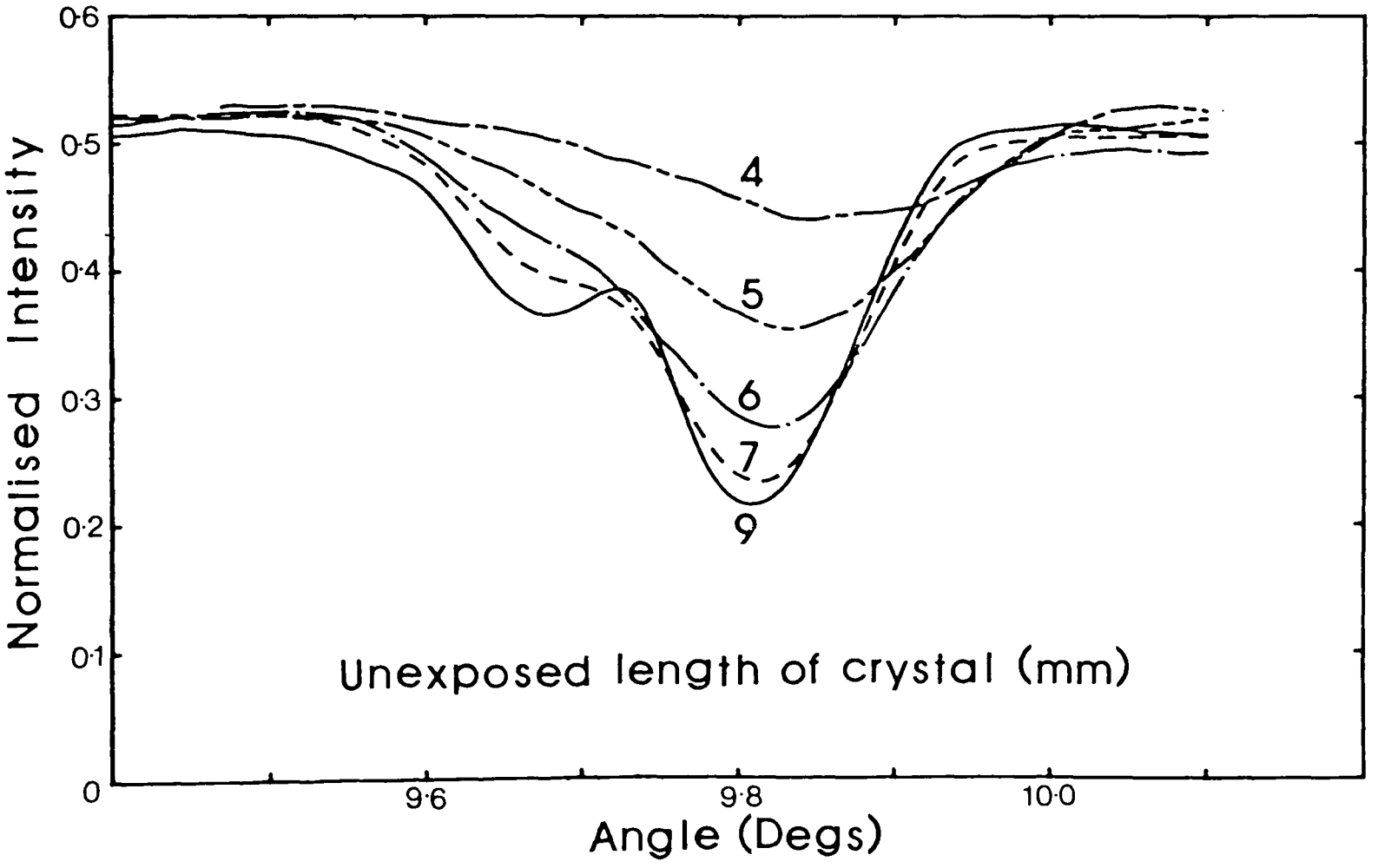

Fig 7.16: Bleaching of crystal

Fig 7.16 shows various stages in the bleaching of a grating in crystal I. It was decided, following the discussion in section VI.3, to systematically erase the grating from the end of the crystal furthest away from the prism apex at recording. As the length of the grating is reduced the overall quality of the grating should improve at the expense

of reduced efficiency and angular selectivity. Most significantly, the unusual 'side-lobe' also disappeared, proving that it was associated with the crystal rather than the measuring apparatus.

VII.3.6 Thermal fixing

Fig 7.17 shows the effect of thermal fixing on the efficiency of the grating. The crystal was heated to a temperature of 160^{o}C in the dark for a period of about 15 minutes and then allowed to slowly cool back to room temperature. Due to the movement of H^{+} ions at this elevated temperature (see chapter four) the grating interaction was no longer measurable. However, after subsequent illumination with incoherent light from an argon lamp for about half an hour the grating partially reappeared. The shift between the peaks is attributable to misalignment of the crystal jig when replaced in the replay apparatus.

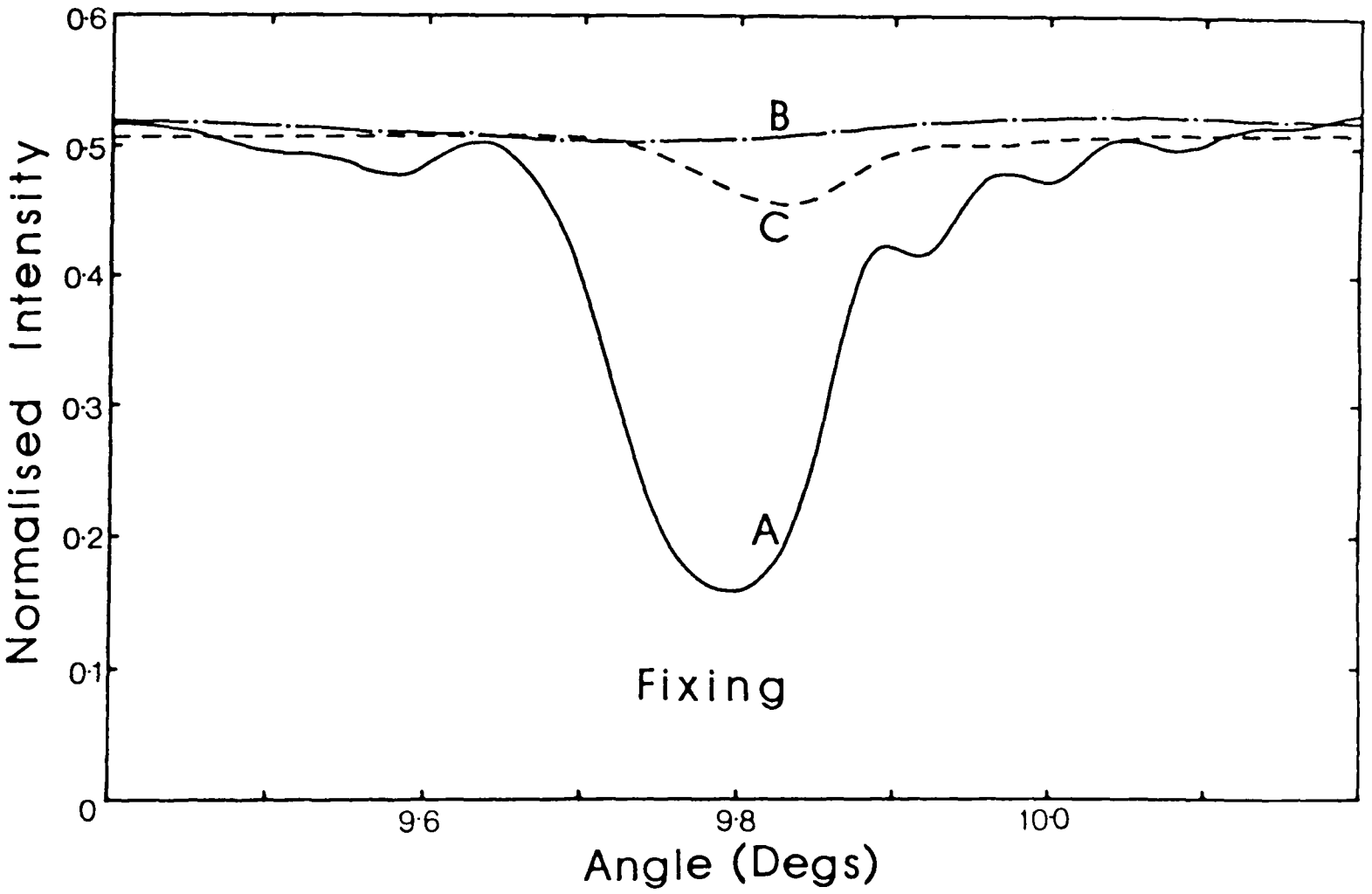

Fig 7.17: Thermal fixing, curve A: original response; curve B: after heating to 160^{o}C; curve C: after illumination with light.

VII.4 SUMMARY

The main features of a highly selective grating in iron doped lithium niobate have been demonstrated, namely: the effect of absorption at recording, the decay of the unfixed grating, the anisotropy of the grating, and the loss of efficiency on fixing. The problems encountered were the lack of consistent results between different crystals, the non-uniformity of the grating response, and the absence of a normal side-lobe structure. A few other attempts were made to explain these complications, such as recording with only one beam (when no grating was formed). However, further work is still required.

CHAPTER EIGHT

MODE SELECTION OF A LASER AND OTHER APPLICATIONS

VIII.1 INTRODUCTION

This chapter discusses how the special qualities of an infra-red VHOE filter could be practically employed. One interesting application, the single mode operation of a semiconductor laser, was successfully demonstrated, at the Plessey research centre, Caswell, Northampton.

VIII.2 PROPERTIES OF A VOLUME HOLOGRAPHIC FILTER

The primary function of this type of filter is to behave as a pass-band device in reflection or a stop-band in transmission. In reflection, a selective volume filter will either diffract a relatively large amount of light from a spectrally narrow light source, such as a semiconductor laser, or diffract a small amount of light from a wide band source.

VHOE's fabricated in photographic emulsion can be used as a IR filter telescope [83], or a tilt-tunable IR filter [75] for atmospheric measurements. A important requirement, however, for these types of wide-band applications is high diffraction efficiency (>90%) and low insertion loss. Since the diffraction efficiency of the lithium niobate filter, especially when fixed, is relatively low, only applications associated with laser sources will be considered.

As discussed in chapter seven, the Bragg wavelength of the volume filter cannot easily be modulated. Therefore the filter must be considered as only a passive device. The complication of fixing then arises. For the experiments described in this chapter fixing has been

avoided, but obviously it must be thoroughly investigated and optimised before the filter can be called a practical device.

The properties of the filter must not be degraded by long term exposure to IR light. Even in undoped lithium niobate, intense IR beams of typically MW/cm^2 will cause unwanted photorefractive changes, known as optical damage. For example, Schmidt [78] discovered that a 1 mW, 1·06 μm laser beam, producing an intensity of $4kW/cm^2$ in an integrated optics waveguide, will cause a refractive index change of about 10^{-5}. In iron doped material the optical damage effect will be a factor 10^2 to 10^3 greater [5]. The problem can be overcome by distributing the incident power over a cross-sectional area of $(mm)^2$ instead of $(\mu m)^2$.

VIII.3 APPLICATIONS WITH LASERS

Consider how the wavelength selectivity of the volume holographic filter compares with the longitudinal mode spacing $\Delta\lambda_{mode}$ of lasers in general use. If $(\tilde{n}L)$ is the optical path length of the lasing cavity,

$$\Delta\lambda_{mode} = \frac{\lambda^2}{\tilde{n}L} \qquad (8.1)$$

Semiconductor lasers are exceptional because their unusually short cavity length (typically 1 mm or less) corresponds to a large mode spacing ($\Delta\lambda_{mode} \approx 4$ Å) – a value greater than the wavelength selectivity of the volume filter (≈ 1 Å for a 4 mm long grating). Two uses for the filter can therefore be envisaged:

i) Demultiplexing or multiplexing [90], either by recording a set of different gratings in one crystal, or by using a set of filters each containing only one grating.

ii) Mode selection of a multi-mode semiconductor laser by selective optical feedback.

The rest of this chapter will concentrate on the feasibility of the second application.

At first sight, it appears that a single mode source can be produced by simply selecting a specific longitudinal mode from the multi-mode output of the semiconductor laser. The problem with this method is the presence of 'partition noise' [89] in the diffracted output caused by random intensity coupling between the lasing cavity modes. For an amplitude modulated signal this is unacceptable. Preferably, the mode spectrum inside the laser should be changed. External optical feedback is one way to achieve this objective.

In gas lasers (like He-Ne or Argon-ion) various methods [80] have been employed to achieve single frequency operation. In all of them the round-trip gain of the laser cavity must not be removed by introducing an attenuating element. Semiconductor lasers, on the other hand, have an intrinsically high gain and therefore do not suffer from this handicap. Furthermore, the difference in round-trip gain between the lasing modes is very small. Consequently, the output spectrum of the laser can readily be affected by minute external reflections which can modulate the effective reflectivity of a cavity mirror as a function of wavelength.

There are at least 11 different designs of single frequency semiconductor lasers. A few examples are shown in Fig 8.1 below. They can be classified under four general headings: coupled cavity, injection locked, geometry controlled and frequency selective feedback. At present, none of these competing designs have shown outstanding properties and consequently the final choice has not been made.

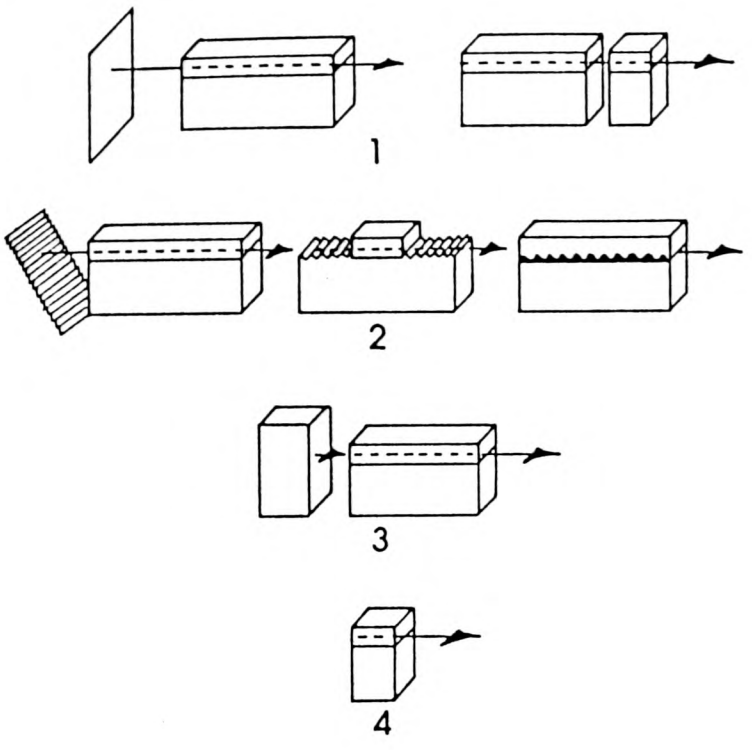

Fig 8.1: Various categories of single frequency semiconductor lasers: 1) coupled-cavity; 2) frequency selective feedback; 3) injection locked; 4) geometry controlled.

In coupled-cavity devices (CCD) the laser beam passes through two separate etalons. Only when a mode is common to the characteristic set of both etalons does lasing occur. CCD's have been fabricated on a single chip, as achieved in the cleaved-coupled-cavity C^3 laser [92]. Alternatively, an external cavity [33] can be added to a conventionally manufactured semiconductor laser. The cavity is formed, either with a mirror, or, if a tunable frequency output is desired, a grating. Both methods are very sensitive to optical path variations. Therefore, the current to the two sections of the C^3 laser must be regulated, and good mechanical stability is necessary for the external cavity configuration.

Injection locked lasers [86] require an external laser, not necessarily another semi-conductor laser, as a reference source to sustain single mode output. This method effectively transfers the condition for single mode operation from one laser to another. British Telecom has used a 1·55 μm He-Ne laser as a stabilised reference, but the whole assembly is very bulky and incompatible with the aim of manufacturing a compact source. There is also the possibility of a

geometry controlled laser. In this type of laser single mode operation is achieved by reducing the length of the cavity to typically only 50 μm.

Frequency selective lasers are usually more difficult to fabricate. There is the choice of either incorporating distributed feedback within the laser itself [51], or introducing feedback using an external grating. The first type of device is not only extremely difficult to manufacture, but is also adversely affected by the interaction between the lasing medium and the grating structure. For example, one notable failing with this geometry is the high value of κd which reduces the effective coupling length of the grating (see section II.4) and hence the achievable selectivity. In comparison, one advantage of external feedback is the separate manufacture of the laser and grating. It simplifies the overall fabrication process, and increases the production yield. Recently an integrated optical filter has been butted against a laser facet [42] to achieve single mode operation. These planar filters, however, need accurate (to microns) stable alignment with micro-positioners. The VHOE filter is the volume equivalent of the planar filter; both devices will diffract only a small range of wavelengths. The advantage of a VHOE over the integrated filter is the simplicity of fabrication and alignment. Experiments using the VHOE filter will be described in the following sections.

VIII.4 THE FIRST EXPERIMENT

The aim of the first experiment was to record an IR filter using the 0·514 μm laser line, designed to counter-propagate a laser beam with wavelength of 1·3 μm incident along the $\underline{K}$-vector of the grating. The optimum recording angle measured with respect to the normal of the 45° prism, was calculated to be 14° 20". There was a small amount of flexibility over the precise recording angle (about ± 0·2 degrees) since

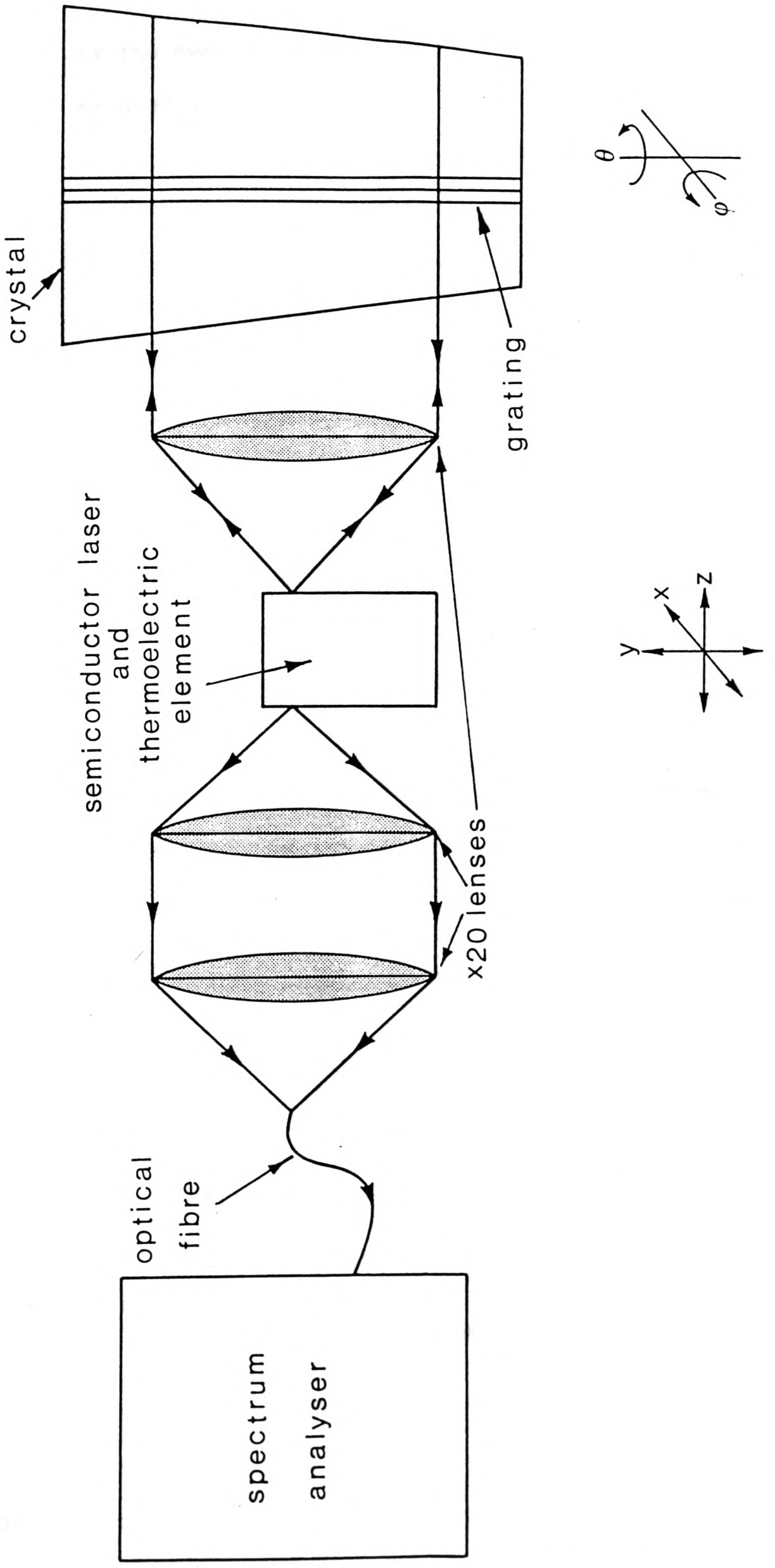

Fig 8.2: Diagram of apparatus used to achieve single mode enhancement

the wavelength from the semiconductor could be tuned over a 1% bandwidth. The crystal was exposed until scattering severely depleted the recording beams.

The experimental equipment, assembled to demonstrate the effect of external optical feedback on a DCBHL (double-channel-buried-hetero-laser) semiconductor laser, is shown in Fig 8.2. A laser module, mounted on a thermoelectric element, with both end facets aligned to optical fibre pigtails, was the IR source. Temperature tuning (of ≈ 5 $\mathring{A}/^{\circ}C$) allowed a limited coarse adjustment of the lasing wavelength, whereas current tuning (indirectly changing the temperature by a small amount) permitted fine wavelength adjustment. A monochromator, containing a rotating glass cube, monitored the spectrum of light passing along one fibre. The other fibre pigtail was aligned with a standard × 20 microscope objective lens to form a collimated beam.

If the divergence of the expanded beam is comparable with the angular Bragg response of the filter, feedback selectivity will be sacrificed. Assuming diffraction-limited optics, this condition will occur when

$$\Delta\theta'_{dif} = \Delta\theta'_{i/2} \qquad (8.2)$$

where,

$$\Delta\theta'_{i/2} \approx \tilde{n} \times \left[\frac{\lambda_R}{\tilde{n}d}\right]^{1/2} \quad ; \quad \Delta\theta'_{dif} = \frac{\lambda_R}{W} \qquad (8.3)$$

and W is the width of the beam. For d = 4 mm, λ_R = 1·3 μm and $\tilde{n}$ = 2·2, $\Delta\theta'_{i/2}$ = 1·5 degrees and W must be greater than 0·02 mm, whereas in the experiment, 0·5 mm < W ≤ 1 mm.

The IR light, diverging from the laser facets, was collimated by adjusting the separation between the laser and lens until the diameter of the expanded beam appeared identical at two positions about half a metre apart. Using this technique, an angular deviation of less than 0·1

degrees could be achieved. The diffraction efficiency of the grating was determined by measuring the dip in transmitted intensity on turning the crystal through the Bragg angle. In this experiment only about a 5% dip in the transmitted beam could be discerned.

The wavelength of the laser was changed until it coincided with the expected Bragg wavelength of the grating. The two reflected beams, derived from the front and back surfaces of the crystal could be seen, with the aid of an IR camera, as two spots on a piece of card; but when the optimum laser wavelength was approached, another spot appeared, the diffracted beam. The orientation of the crystal, in both the vertical and horizontal planes, and the laser wavelength, were systematically adjusted until the diffracted beam passed through the lens of the microscope objective.

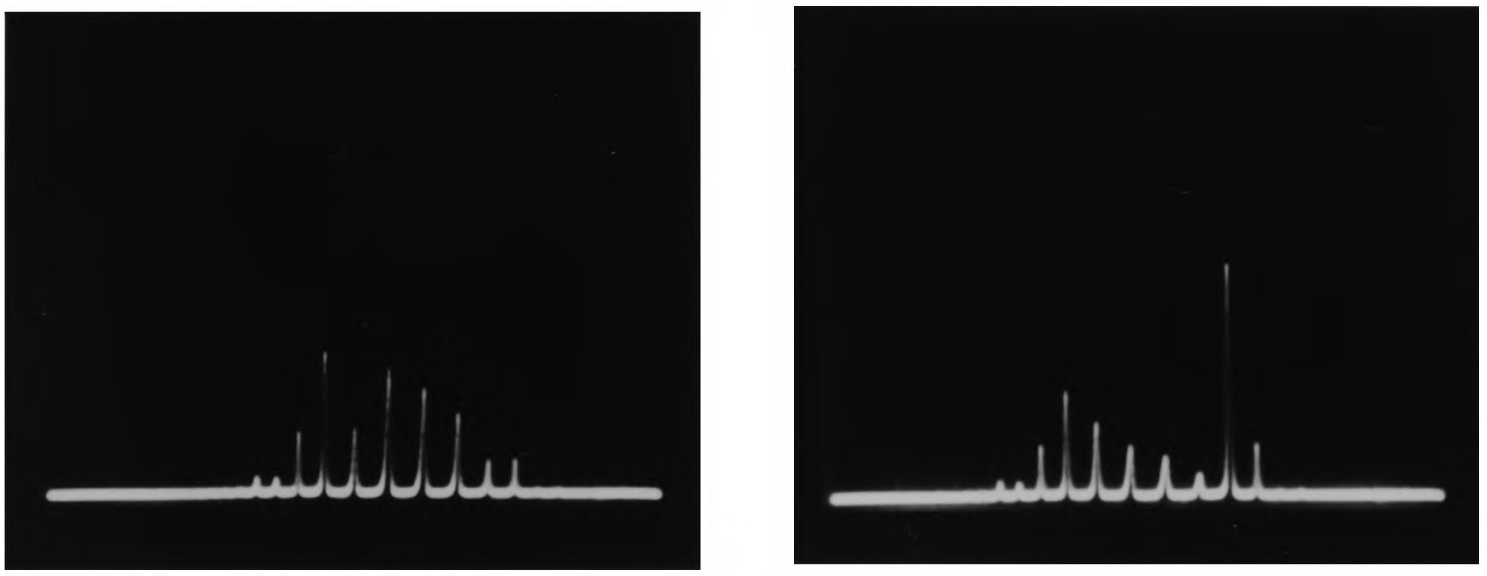

1 2

Fig 8.3: Before (1) and after (2) application of feedback to the 1·3 μm semiconductor laser

Immediately, the relative intensity of the laser modes changed and one particular mode, as shown in Fig 8.3, was enhanced. The wavelength of this mode, according to the reading on the monochromator, was (1·2880 ± .0002) μm - remarkably close to the intended value of 1·3 μm!

When the light path between the laser and crystal was blocked the mode spectrum of the laser returned to its normal multi-mode

distribution. Neither were any feedback effects from the grating observed within a ± 60 Å range of the Bragg interaction. Both the incident and exit polished faces of the crystal were deliberately slanted to divert spurious reflections away from the laser. The grating was therefore responsible for the feedback.

The apparent bandwidth of the grating was about 4 Å, compared with an intermode spacing of about 10 Å, but the complications introduced by the effect of the laser response made this value disputable. The unexpectedly low selectivity and diffraction efficiency of the grating implied that the effective length of the grating was unusually short. Nevertheless, the results were sufficiently promising to warrant another trial run at a different laser wavelength. It was also hoped that feedback could be substantially increased by removing the fibre pigtails.

VIII.5 THE SECOND EXPERIMENT

In the second experiment the grating was arranged to reflect at 1.55 μm. At this longer wavelength, the low attenuation [38] of optical fibres allows long distances (about 100 km) between repeater stations. It is therefore a popular wavelength for optical communication systems. The necessary recording angle was calculated to be $25^{\circ}\ 20''$.

At replay, the two fibre pigtails were removed to make the facets of the laser directly accessible. A large proportion of the radiated light could then be intercepted by the microscope objective. The single mode behaviour in this experiment, with an adjacent mode rejection ratio of ≈ 16 dB, was far superior to that obtained in the first experiment, as shown by the set of traces in figure 8.4. The laser temperature was adjusted until the grating wavelength coincided with a longitudinal mode

of the laser. Single mode operation could then be maintained over a C.W. current range I_{DC} of over 20 mA.

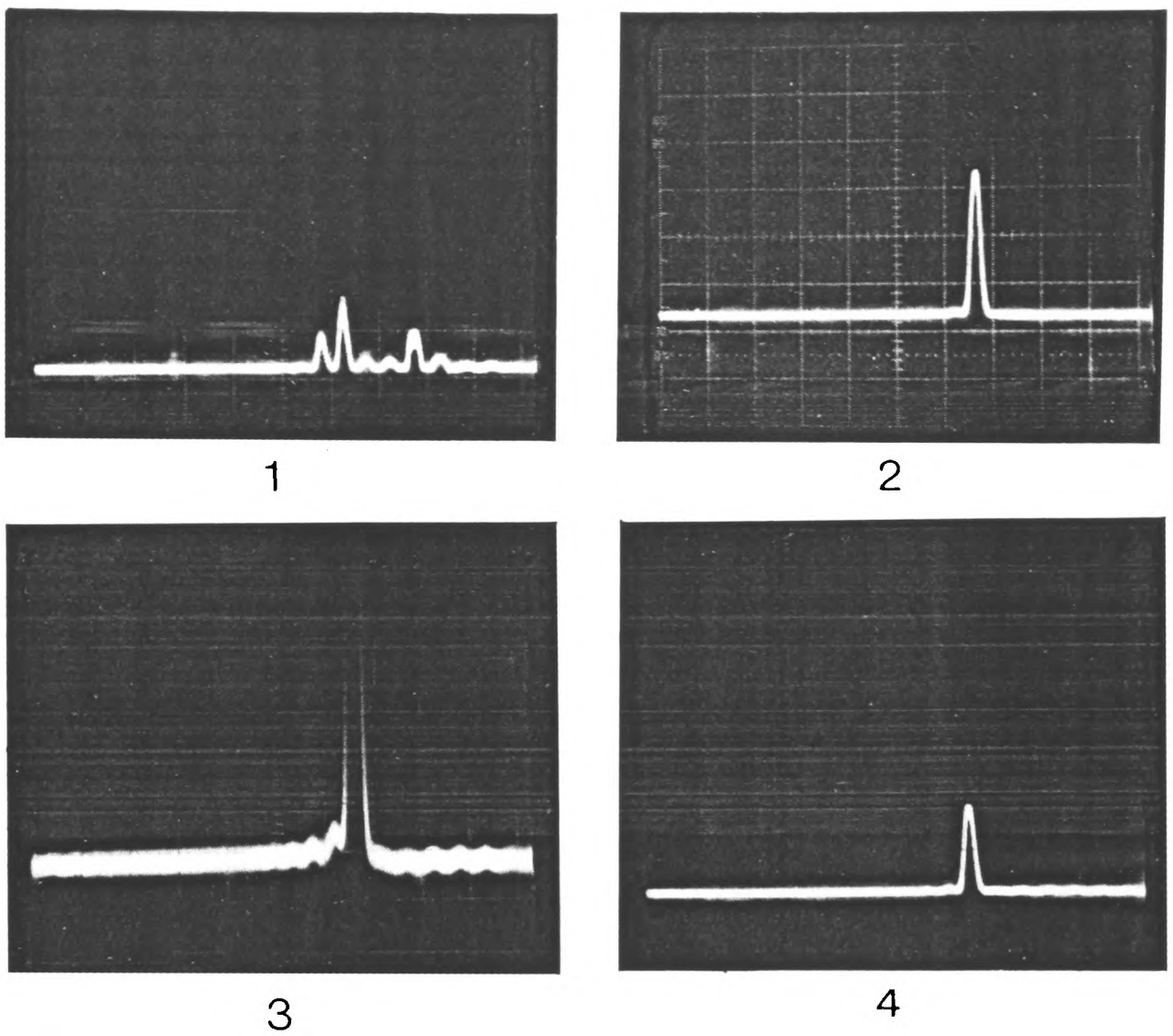

Fig 8.4: Single mode behaviour of the 1·55 μm laser: 1) No feedback; 2) feedback, I_{DC} = 70 mA; 3) As 2) with ×10 scale; 4) feedback, I_{DC}= 60 mA. $I_{threshold}$ = 40 mA.

VIII.6 PROPOSED IMPROVEMENTS

Can the performance of the hybrid device be improved by evaporating anti-reflection coatings onto the laser facets? To answer this question it is necessary to discuss the relative importance of the various optical cavities in the system. Three will be mentioned.

Cavity I, generally the most important, is defined as the optical path length between the parallel polished laser facets. Multiple internal reflections inside the laser will establish a standing wave pattern associated with a characteristic set of longitudinal cavity modes. Cavity II is the filter, if considered as an etalon of length d,

and as mentioned before has only one excitable mode. Cavity III is the optical path length between one laser facet, and the filter at the other end behaving as a distributed mirror (see Fig 8.5).

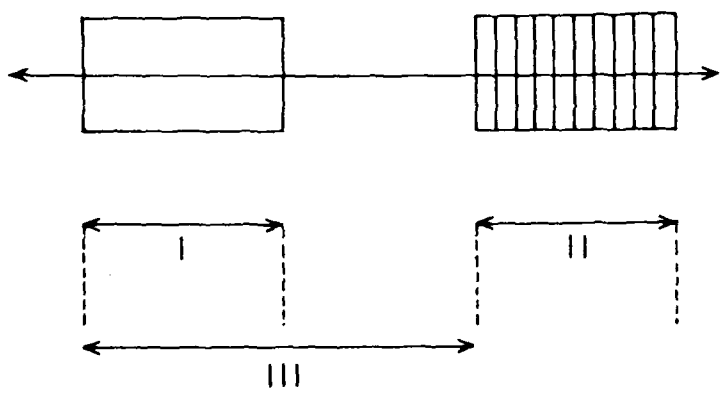

Fig 8.5: Significant cavity modes

So far, the contribution from cavity I has been dominant. When the laser facets are bloomed, however, cavities II and III will become important and significantly perturb the laser output. Cavity III is associated with a much longer optical path length (about 1 - 2 cm in this experiment) and therefore a finer mode spacing (< 1 Å). At the expense of more effective feedback there could be a series of closely spaced modes lasing within the bandwidth of the filter selectivity response. This problem can be avoided if the selectivity of the filter is sufficiently large or cavity III is sufficiently short.

The amount of feedback can also be increased by improving the performance of the collimating lenses. For optimum beam coupling the lenses must have a large f-number (to collect most of the diffracted light from the laser), a small focal point (for efficient injection of the feedback light back into the laser) and low reflection or scattering losses (to reduce spurious feedback effects). Further work is required to optimise the diffraction efficiency of the grating and increase the uniformity of the Bragg response.

VIII.7 APPLICATIONS FOR A SINGLE MODE LASER

Two possible applications for a fixed frequency single mode laser are:

i) optical heterodyning, when two lasers called the 'local oscillator' and the 'signal generator', operating at different wavelengths, both with stable, pre-determined frequency, are mixed together in a non-linear system, or,

ii) any system where two or more lasers must be locked together to emit a common reference wavelength output. For a VHOE this can be achieved by arranging for the lasers to share the feedback characteristics of the same grating.

CHAPTER NINE

CONCLUSIONS

This thesis has discussed a way of holographically creating an infra-red filter in a large volume of materials (mm^3) rather than as a two dimensional surface variation. Using the principle of 'scaling' - recording and replaying at different wavelengths, a grating with a characteristic coupling length of 4 mm has been successfully fabricated. The complications arising from this technique have been identified in a number of ways.

There are the limitations of the recording material itself. For iron doped lithium niobate the most important are: scattering, low exposure sensitivity and the lack of repeatability. The experiments monitoring the time-development of the grating during exposure, have shown that dynamic scattering severely depletes the recording beams and prematurely retards the development of the grating. Considerably higher diffraction efficiencies may be achievable if the sources of scattering can be minimised. The relatively long exposure time, typically three minutes, does not pose a serious stability problem for the recording geometry discussed in this thesis. A continual handicap, however, has been the inability to record gratings from one exposure to the next and from one crystal to the next with repeatable filter characteristics. In this respect there is a weakness with the recording geometry because it is difficult to accurately relocate the optical components between exposures.

The diagnostic replay experiments show the problems that occur when trying to determine the profile of an inhomogeneous volume grating, if all its dimensions are comparable with the width of the probe beam.

Under these circumstances, the finite extent of the hologram and probe beam must be considered. The task of analysis was hampered by having to scan the angular rather than the frequency response of the filter. Nevertheless, some general comments can still be made. First of all, high wavelength selectivity cannot be disassociated from high angular selectivity, secondly, a scaling geometry clearly shows the variation in grating strength caused by absorption at replay and thirdly, the effect of birefringence has been demonstrated. A totally different way of measuring the grating profile was attempted using a Scanning Electron Microscope (SEM), which could possibly reveal the underlying space charge fields responsible for the refractive index variation. However, this proved to be unsuccessful, because although the crystal was coated with a thin layer of aluminium, the crystal rapidly charged up to a high voltage and all detail was obliterated. It also raises the point that the space charge variation would be averaged out by the process of measurement.

Although the control of grating profile achievable in iron doped lithium niobate compares unfavourably with planar integrated optics devices, it is nevertheless possible in lithium niobate to alter the modulation strength by optical bleaching. The choice between bulk and planar devices will probably depend on the exact type of application; the use of a volume rather than a planar filter to achieve single mode operation of a semiconductor laser being a good example.

Further work is required to optimise the uniformity and efficiency of the fixed grating. One option available is to investigate whether simultaneous recording and fixing can improve the final efficiency of the grating. Another possibility is to deliberately slant the $\underline{K}$-vector with respect to the c-axis of the crystal. In the standard replay arrangement only the r_{113} tensor component can be used. If the $\underline{K}$-vector is slanted, however, a component of the r_{333} tensor component is available to increase the coupling constant, although the photovoltaic field

contribution will then be less. One crystal was specially cut with the c-axis arbitrarily slanted at an angle of 45 degrees out of the plane containing the incident (XZ) face. Unfortunately, a measurable grating could not be recorded in the crystal. If a greater selection of crystals is available the effect of doping level and visible absorption on grating efficiency could also be investigated.

When discussing fixing, the problem of electronic relaxation must be considered. Once the fixed grating is left in the dark the internal electric fields will slowly return to a new state of equilibrium. There will be two modulated patterns of electronic and H^+ ions present (refer to chapter four) which due to the effects of diffusion do not completely cancel. The remaining or remnant field is responsible for the presence of a grating. To regenerate the maximum fixed modulation strength, however, the crystal must be periodically illuminated with light.

Latent photopolymers, as mentioned in chapter three, are also capable of storing a thick volume hologram, though apparently without the same loss of efficiency during fixing. It would be profitable to discover the practical advantages and disadvantages of this material in comparison with lithium niobate.

APPENDIX A

THE ELECTRO-OPTIC TENSOR

The vector $\underline{\tilde{D}}$ in any medium is related to the propagating $\underline{\tilde{E}}$ field of the light wave by a tensor relationship

$$\tilde{D}_i = \tilde{\epsilon}_{ij}(\underline{E})\,\tilde{E}_j \qquad (A.1)$$

(where repeated indices imply the Einstein summation convention and i,j,k = 1..3). The permittivity tensor $\tilde{\epsilon}$ is assumed to be a function of the static electric field $\underline{E}$.

A common geometric representation of this tensor, convenient for describing the behaviour of light waves in anisotropic media, is the indicatarix or the index ellipsoid which can be mathematically expressed as

$$\eta_{ij} \cdot \underline{x}_i \cdot \underline{x}_j = 1 \qquad (A.2)$$

or,

$$\eta_{11}x^2 + \eta_{22}y^2 + \eta_{33}z^2 + \eta_{12}xy + \eta_{21}yx + \eta_{23}yz +$$

$$\eta_{32}zy + \eta_{31}zx + \eta_{13}xz = 1 \qquad (A.3)$$

where η_{ij} is the impermeability tensor equal to $1/\tilde{\epsilon}_{ij}$. From energy considerations, $\eta_{ij} = \eta_{ji}$ and therefore,

$$\eta_{11}x^2 + \eta_{22}y^2 + \eta_{33}z^2 + 2\,\eta_{12}xy + 2\,\eta_{23}yz + 2\,\eta_{31}zx = 1 \qquad (A.4)$$

The plane normal to the wave vector $\underline{k}$ intercepts this surface in an ellipse; the axes of the ellipse provide the directions of polarisation for the ordinary and extraordinary rays.

The application of a static electric field will redistribute the valence charges in the material, alter the polarisation, and consequently will perturb the η tensor. For lithium niobate the induced birefringence is proportional to the first power of the applied $\underline{E}$-field, commonly known as the Pockels or linear electro-optic effect. The Pockels effect only

occurs because the material lacks inversion symmetry; there is no central point through which every atom can be reflected into an identical atom. Hence,

$$\eta_{ij}(\underline{E}) - \eta_{ij}(0) = \Delta\eta_{ij} = r_{ijk}\, E_k \qquad (A.5)$$

The above identity is generally used to define r_{ijk}, the third rank linear electro-optic tensor. There are 27 elements, but because $\eta_{ij} = \eta_{ji}$ only 18 of these are independent. A contracted Voigt notation can Therefore be introduced where

$$(11)\rightarrow 1,\ (22)\rightarrow 2,\ (33)\rightarrow 3,\ (23)=(32)\rightarrow 4,\ (31)=(13)\rightarrow 5,\ (12)=(21)\rightarrow 6 \qquad (A.6)$$

The values for the elements [102] of the electro-optic tensor for undoped lithium niobate (crystal class $3\bar{m}$) are usually stated in this reduced notation, with units of 10^{-12} m/V and k corresponding to the column number

$$r_{(ij)k} = \begin{vmatrix} 0 & -3.4 & 8.6 \\ 0 & 3.4 & 8.6 \\ 0 & 0 & 30.8 \\ 0 & 28.0 & 0 \\ 28.0 & 0 & 0 \\ -3.4 & 0 & 0 \end{vmatrix} \qquad (A.7)$$

Since,

$$\Delta\tilde{\epsilon}_{ij} = -\frac{\tilde{\epsilon}_{ii}(0)\,\tilde{\epsilon}_{jj}(0)\,\Delta\eta_{ij}}{\epsilon_o} \qquad (A.8)$$

$$\Delta\tilde{\epsilon}_{ij} = -\frac{\tilde{\epsilon}_{ii}(0)\,\tilde{\epsilon}_{jj}(0)\,r_{ijk}\,E_k}{\epsilon_o} \qquad (A.9)$$

In heavily doped crystals of lithium niobate there will a large photovoltaic field along the crystallographic z-axis (c-axis). The perturbed $\tilde{\epsilon}_{ij}(\underline{E})$ tensor will then be

$$\begin{vmatrix} \tilde{\epsilon}_{11}(0) - r_{113}\tilde{\epsilon}_{11}^{2}(0)\,E_3 & 0.0 & 0.0 \\ 0.0 & \tilde{\epsilon}_{22}(0) - r_{223}\tilde{\epsilon}_{22}^{2}(0)\,E_3 & 0.0 \\ 0.0 & 0.0 & \tilde{\epsilon}_{33}(0) - r_{333}\tilde{\epsilon}_{33}^{2}(0)\,E_3 \end{vmatrix}$$

where for lithium niobate $\tilde{\epsilon}_{11}(0) = \tilde{\epsilon}_{22}(0) \neq \tilde{\epsilon}_{33}(0)$. The tensor is already in a diagonal form and so the relevant perturbed refractive indices can be directly determined.

APPENDIX B

RESOLUTION OF THE DETECTION SYSTEM

B.1 INSTRUMENTAL BROADENING

The phase and amplitude distribution across the incident probe beam can be considered as either Fraunhofer (plane waves) or Fresnel, depending upon the Rayleigh criterion [10]. If C, as defined below, is equal to unity there will be a $\frac{\lambda}{8}$ phase deviation from parallelism across the beam. If C << 1 the Fraunhofer condition applies.

$$C = \frac{2\ W^2}{\lambda_R\ \Delta z} \qquad (B.1)$$

where W is the width of the beam. The value of Δz, the separation between aperture and crystal, was about 0·5 m in all these experiments. Typical values for C, as a function of W are tabulated below.

W(mm)	0·2	0·5	1·0
C	0·14	0·86	3·4

Table B.1: Criterion for Fraunhofer and Fresnel approximations

With experimental values for W in the range of 0·5 to 1 mm, the replay conditions are intermediate between Fraunhofer and Fresnel. A Fraunhofer approximation simplifies the mathematical calculation and will therefore be used as the initial approximation.

Consider the effect of diffraction at the aperture generating an angular spread of plane waves in both the vertical (ϕ) and horizontal (θ) plane. If in either of these orthogonal planes the angular spread is

comparable with the angular selectivity of the grating, the resolution of the measuring system will be impaired. As explained below, when $\theta_o \neq 0$ and $\phi = 0$, the angular selectivity of the grating in the vertical plane ($\Delta\phi_{1/2}$) can be significantly less than the angular selectivity of the grating in the horizontal plane ($\Delta\theta_{1/2}$). Under these circumstances, diffraction of light in the vertical plane can be neglected.

Extending equation (2.34) to two dimensions, the first minimum in the Bragg interaction will occur when

$$\cos(\theta)\cos(\phi) - \cos(\theta_o)\cos(\phi_o) = \frac{\lambda_R}{\tilde{n}d} \qquad (B.2)$$

Rotating the crystal in a vertical plane, assuming $\theta = \theta_o$ and $\phi_o \approx 0$.

$$(\phi - \phi_o) = \Delta\phi_{1/2} \approx \left[\frac{\lambda_R}{\tilde{n}d\cos(\theta_o)}\right]^{1/2} \approx \left[\frac{\lambda_R}{\tilde{n}d}\right]^{1/2} \qquad (B.3)$$

From chapter two, if $\theta_o >> \Delta\theta_{1/2}$,

$$\Delta\theta_{1/2} \approx \frac{\lambda_R}{2\,\tilde{n}d\sin(\theta_o)} \qquad (B.4)$$

$$\text{therefore } \Delta\theta_{1/2} << \Delta\phi_{1/2}. \qquad (B.5)$$

Making this one-dimensional approximation, the amplitude of the transmitted beam $\underline{\rho}$ in a given direction, using a transfer function approach, is

$$\chi\left[\theta'_w\right] = \Pi\left[\theta'_w\right] \times R\left[(\theta' - \theta'_w), d\right] \qquad (B.6)$$

where Π is an aperture function, generating a set of plane waves, R is the angular response of the grating, and χ is the measured response. The external angles θ' and θ'_w are drawn in Fig B.1.

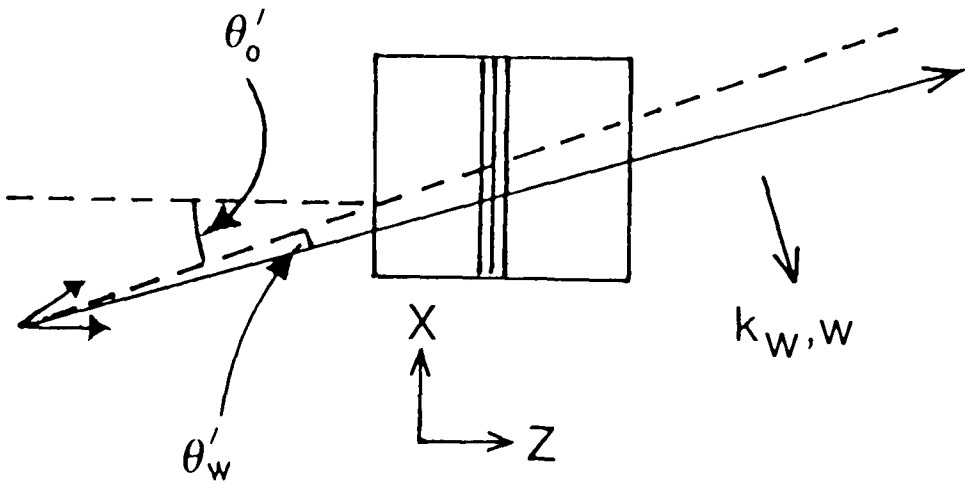

Fig B.1: Angular spread of plane waves incident upon the crystal due to diffraction at slit.

The intensity measured at a particular point on the detector will be the sum of all these plane waves, or $|\bar{\chi}(w)|^2$, where $\bar{\chi}(w)$, $\chi(k_w)$ are a Fourier transform pair and w is measured from the centre of the beam.

$$\bar{\chi}(w) = \frac{1}{2\pi} \int_{-\infty}^{+\infty} \chi(\theta'_w)\, e^{ik_w w}\, dk_w \qquad (B.7)$$

where for small angles,

$$k_w = k \sin(\theta') \approx k\, \theta'_w \qquad (B.8)$$

$$dk_w \approx k\, d\theta'_w \qquad (B.9)$$

As expected, the result is a convolution integral,

$$\bar{\chi}(w) = \frac{k}{2\pi} \int_{-\infty}^{+\infty} \Pi(\theta'_w)\, R(\theta' - \theta'_w)\, e^{ik\theta'_w w}\, d\theta'_w \qquad (B.10)$$

Assuming the slit severely truncates the Gaussian laser beam, the aperture function $\Pi(w)$ can be considered as a top hat function. The Fourier transform of Π is then,

$$\Pi(\theta'_w) = W \times \mathrm{sinc}(kW\theta'_w/2) \qquad (B.11)$$

At w = 0, the intensity of the transmitted beam will be

$$|\bar{\chi}(0)|^2 = \left| \frac{kW}{2\pi} \int \mathrm{sinc}(kW\theta'_w/2)\, R(\theta' - \theta'_w)\, d\theta'_w \right|^2 \qquad (B.12)$$

The function $|\bar{\chi}(0)|^2$ has been plotted below in figure B.2 for a typical replay Bragg angle of θ'_o = 9·8 degrees. The real and imaginary

values of the function R were generated from a numerical coupled-wave model (see chapter two). From figure B.2 we conclude that instrumental broadening due to diffraction can be neglected for slit widths greater than 1 mm in the horizontal plane.

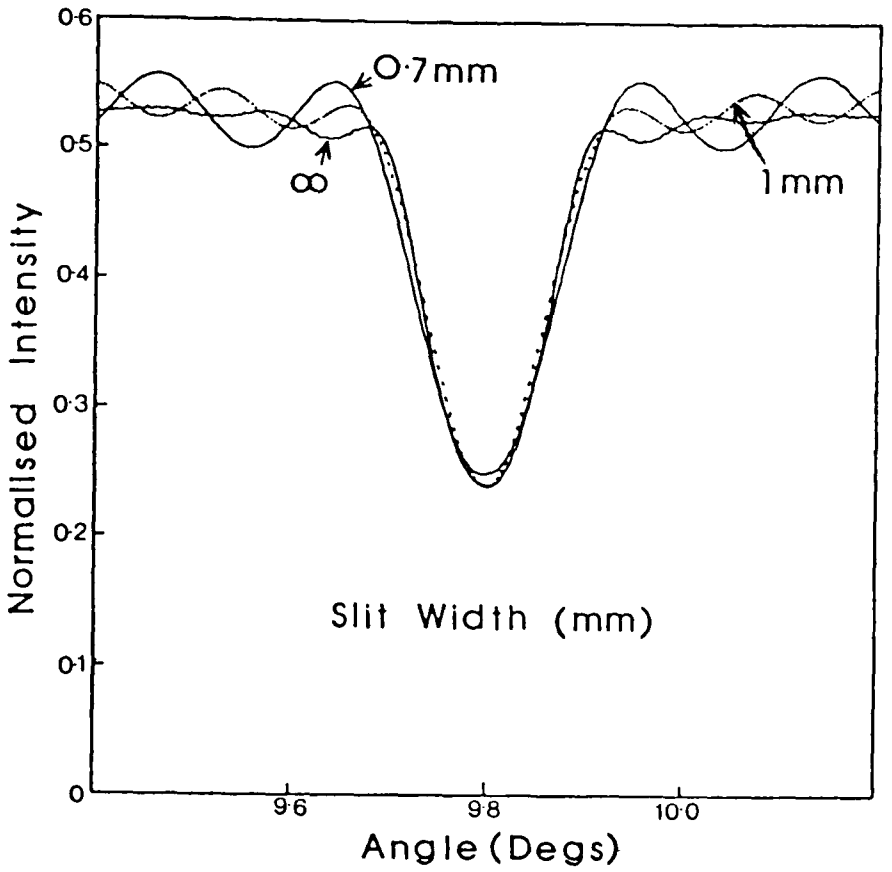

Fig B.2: Convolution of grating response with sinc function for three different slit widths.

B.2 VARIABLE GRATING LENGTH

The finite width recording beams will overlap inside the grating to produce the grating region shown in Fig B.3 below. Consequently, the IR probe beam will sample across its width a varying number of reflecting fringe planes. From equation (6.4), the change in grating length Δd across an incident probe beam of width W will be

$$\Delta d = 2 \times W \times \left[\left[\frac{\beta_G}{\beta_R} \right]^2 - 1 \right]^{-1/2} \qquad (B.13)$$

For a typical value of W equal to 1 mm, a recording wavelength of 0·514 μm, and a replay wavelength of 1·15 μm, Δd is about 1 mm. The effect of this variation on the measured intensity response is illustrated in Fig B.4. The first curve is the best fit, using coupled-wave theory, to the experimental curve in Fig 7.9 with a characteristic

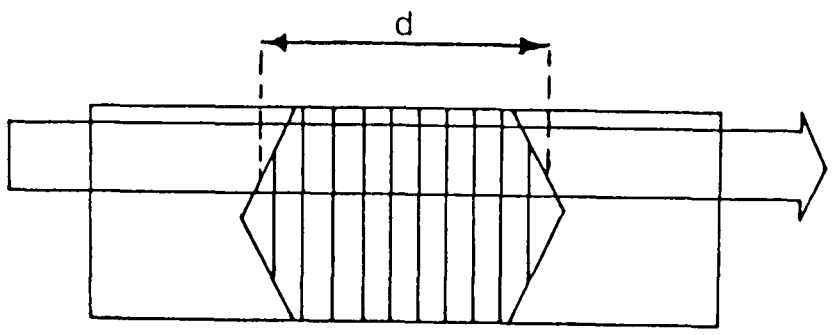

Fig B.3: Overlap region inside crystal

grating length d = 4 mm. The other two show the change in the off-Bragg characteristics for d = 4·5 mm and d = 3·5 mm.

Generally a weighted average over the whole width of the beam is required. However, whichever model is used, it is obvious the sharp structure will be removed. In particular, the side-lobe structure will be smoothed out, but the central maximum and half-width will not be strongly affected.

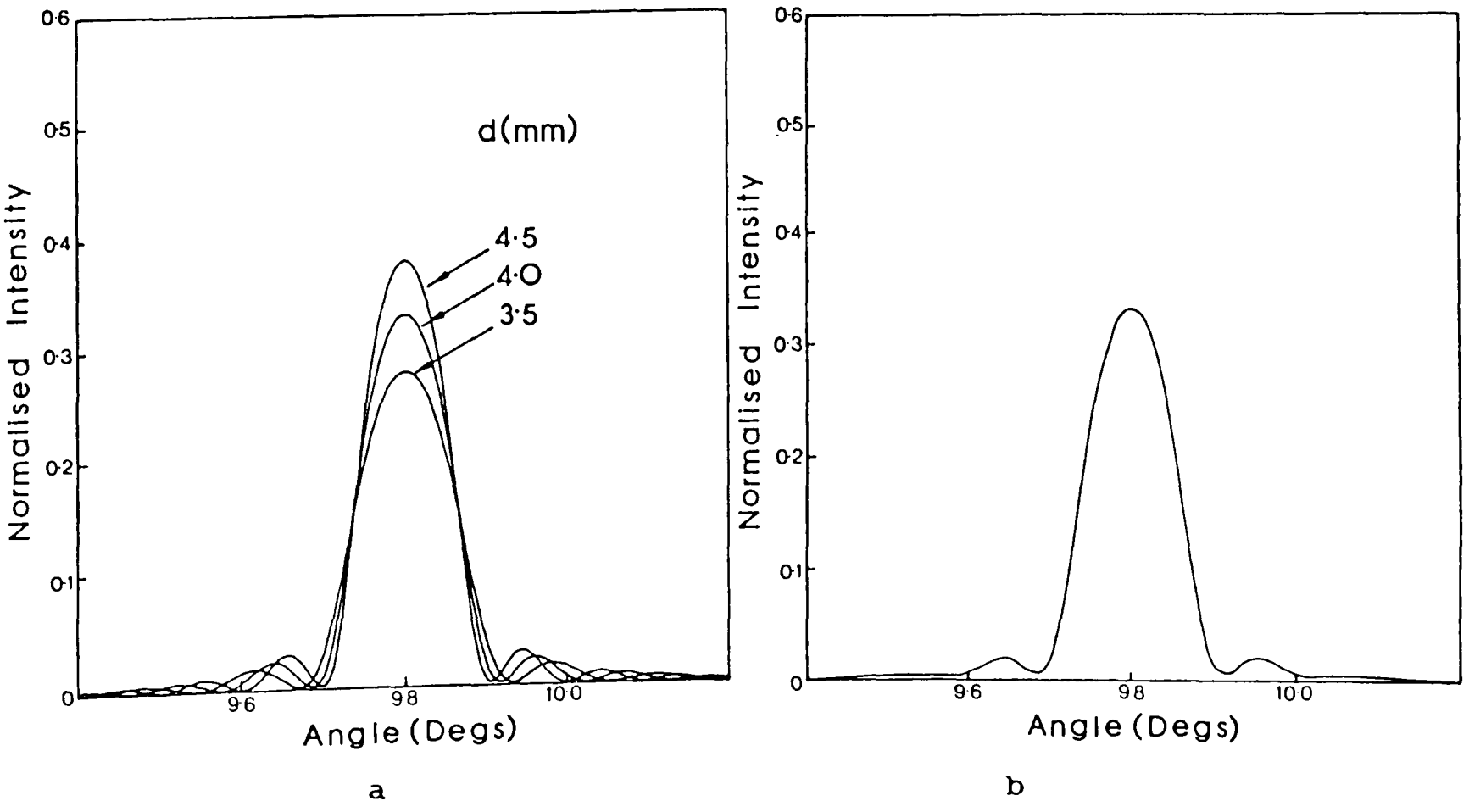

Fig B.4: Effect of variable grating length. Fig a): diffraction curves for d = 3·5, 4·0 and 4·5 mm; Fig b): Average of the three curves in Fig a)

B.3 FINITE WIDTH OF THE CRYSTAL

Another limitation of having a finite width incident beam occurs when the grating is probed off-normal incidence; various parts of the beam will be diffracted by different lengths of the volume grating. The diffracted beam is now split into three separate regions as shown in Fig B.5, namely AB,BC and CD.

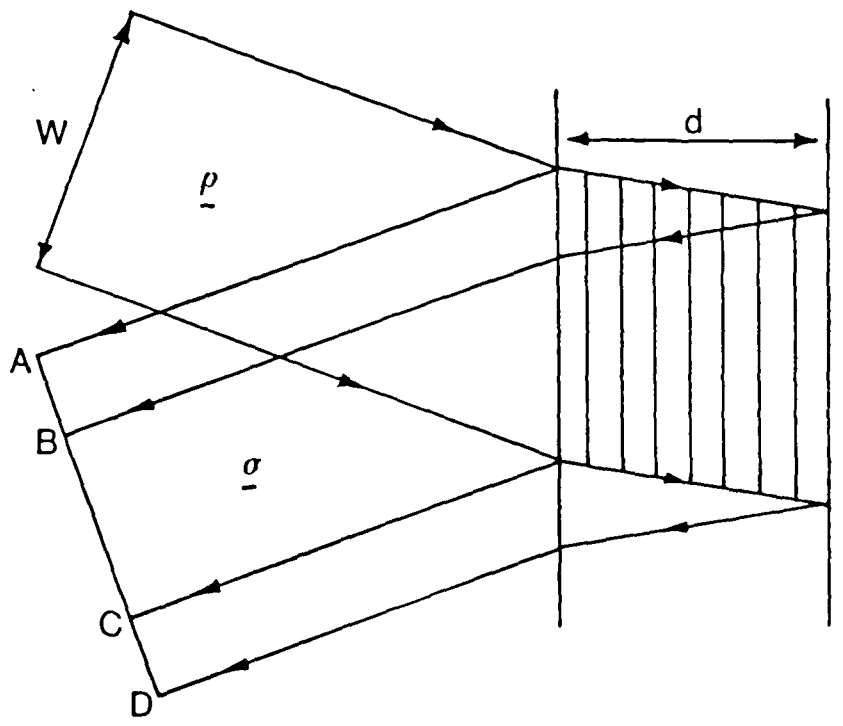

Fig B.5: Diffraction off-normal incidence

The centre region BC, contains light which is diffracted from the full length of the grating. Light directed into the two wings AB and CD, however, cannot be produced from the full number of reflecting planes inside the grating. The 'off-Bragg' response for each point (or line in two dimensions) within AB or CD will therefore deviate from the expected value for an ideal grating.

In the experiment the detector generates a signal proportional to the integrated total of all the local intensity contributions across the diffracted beam. Depending upon the relative size of the three regions, it is expected that the overall side-lobe structure will either be

blurred or totally removed. The calculation given below indicates that this effect will be important. The width of AB, W_{AB} is

$$W_{AB} = d \times \sin(2\theta'_o) \times \left[\tilde{n}^2 - \sin^2(\theta'_o)\right]^{-1/2} \qquad (B.14)$$

For a typical grating length d = 3 or 4 mm, $\tilde{n} = 2{\cdot}23$ at $\lambda_R = 1{\cdot}152\ \mu m$, with external Bragg angle θ'_o of 10 degrees,

$$W_{AB} \approx 0{\cdot}5 \text{ mm} \qquad (B.15)$$

Since the width of the incident beam,

$$W = W_{AC} = W_{BD} \quad \left[W_{AB} = W_{CD}\right] \qquad (B.16)$$

is only about 1 mm, further analysis is required.

A comprehensive treatment of this problem requires a numerical two-dimensional coupled wave model, allowing for spatially non-uniform beams and off-Bragg effects [81]. But even this calculation can only include self-diffraction by rigorously solving the differential equations. A simpler approach is to use the kinematic theory described in chapter two. However, only the intensity of the diffraction beam can be directly analysed. From equation (2.4), when no absorption is assumed to be present,

$$\zeta = 2\ K\ \Lambda \cos(\theta) \qquad (B.17)$$

If N fringe planes contribute to the diffracted beam at a particular point on the wavefront, the resultant amplitude in the kinematic approximation will be

$$A_N = r\left[1 + e^{i\zeta} + e^{2i\zeta} + e^{3i\zeta} \ldots\ldots\ldots e^{i(N-1)\zeta}\right] \qquad (B.18)$$

where r is the reflectivity of a fringe plane, per unit length. Summing this series,

$$A_N = r\,\frac{(e^{iN\zeta} - 1)}{(e^{i\zeta} - 1)} = r\,e^{i\zeta(N-1)/2}\,\frac{\sin(N\zeta/2)}{\sin(\zeta/2)} \qquad (B.19)$$

Generally, there are two ways to calculate the diffracted intensity: adding the local amplitudes (coherent addition implying Fraunhofer) or adding the local intensities across the beam (incoherent addition). The first method assumes no self-diffraction of the beam,

whereas the second assumes maximum self-diffraction. The actual situation must be somewhere between these two limits.

B.3.1 Incoherent addition

For region AB,

$$I_{AB} = \sum_{N=0}^{N_m - 1} I_N = \sum_{N=0}^{N_m - 1} \left[A_N \times A_N^* \right] = r^2 \sum_{N=0}^{N_m - 1} \left[\frac{\sin(N\zeta/2)}{\sin(\zeta/2)} \right]^2 \qquad (B.20)$$

When the grating is probed 'on-Bragg', then for $N_m >> 1$ this expression reduces to

$$I_{AB} = \sum N^2 \approx \frac{r^2 \, N_m^3}{3} \qquad (B.21)$$

but generally,

$$I_{AB} = \frac{r^2}{2} \sum_{N=0}^{N_m - 1} \left[\frac{1 - \cos(N\zeta)}{\sin^2(\zeta/2)} \right] \qquad (B.22)$$

performing the summation,

$$I_{AB} = \frac{r^2}{2 \sin^2(\zeta/2)} \left[N_m - \frac{\sin(N_m\zeta/2)}{\sin(\zeta/2)} \cos\left[(N_m - 1)\zeta/2 \right] \right] \qquad (B.23)$$

This expression can be approximated under the circumstances $N_m >> 1$, $\left[N_m\zeta \right] \approx 1$, when $\sin(\zeta/2) \approx \zeta/2$ to give

$$I_{AB} = r^2 \, \frac{2 \, N_m^3}{(N_m\zeta)^2} \left[1 - \frac{\sin(N_m\zeta)}{(N_m\zeta)} \right] \qquad (B.24)$$

$$\text{as } \zeta \to 0, \; I_{AB} \to \frac{N_m^3 \, r^2}{3} \qquad (B.25)$$

agreeing with the earlier value. In the central region, where the full number of reflecting beams contribute,

$$I_{BC} = \sum_{N=0}^{N_m - 1} \left[A_{N_m} \times A_{N_m}^* \right] = r^2 \, N_m^3 \left[\frac{\sin(N_m\zeta/2)}{(N_m\zeta/2)} \right]^2 \qquad (B.26)$$

Hence,

$$I_{BC} = 2 \, r^2 \, N_m^3 \, \frac{\left[1 - \cos(N_m\zeta) \right]}{(N_m\zeta)^2} \qquad (B.27)$$

The total intensity measured by the detector is therefore

$$I_{AD} = \left[W_{AB} \times I_{AB}\right] + \left[W_{BC} \times I_{BC}\right] + \left[W_{CD} \times I_{CD}\right] \qquad (B.28)$$

Inserting the expressions for each bracket, the final expression for the diffracted intensity, with no absorption present, is

$$I_{AD} = \frac{r^2 N_m^3}{(N_m\zeta)^2}\left[4W_{AB}\left[1 - \frac{\sin(N_m\zeta)}{(N_m\zeta)}\right] + 2W_{BC}\left[1 - \cos(N_m\zeta)\right]\right] \qquad (B.29)$$

The normalised function I_1 has been plotted for W_{AB} = 0·5 mm, where

$$I_1\left[W, \frac{N_m\zeta}{2\pi}\right] = \frac{I_{AD}}{I_{AD(MAX)}} \qquad (B.30)$$

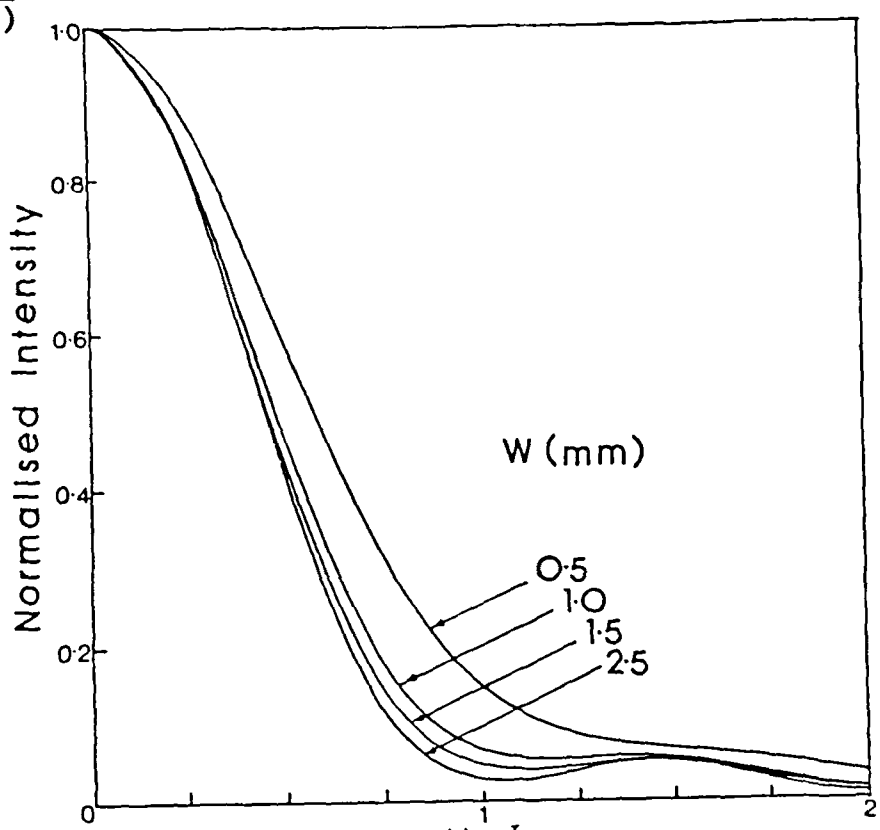

Fig B.6: Incoherent summation

B.3.2 Coherent addition

In this case amplitudes instead of intensities must be summed and

$$I_{AB} = \left[\sum_{N=0}^{N_m-1} A_N\right] \times \left[\sum_{N=0}^{N_m-1} A_N^*\right] \qquad (B.31)$$

where,

$$\Sigma A_N = \frac{r\, e^{-i\zeta/2}}{2i \sin(\zeta/2)} \sum_{N=0}^{N_m-1} (e^{iN\zeta} - 1) \qquad (B.32)$$

Probing the grating 'On-Bragg', for $N_m >> 1$

$$I_{AB} = \Sigma N \times \Sigma N \approx \frac{r^2 N_m^4}{4} \qquad (B.33)$$

but generally, the final expression is

$$I_{AB} = \frac{r^2 N_m^2}{4 \sin^2(\zeta/2)} \left[1 + X^2 - 2X \cos\left[(N_m - 1)\zeta/2\right]\right] \qquad (B.34)$$

$$\text{where } X = \frac{\sin(N_m \zeta/2)}{\sin(\zeta/2)\, N_m} \qquad (B.35)$$

In the central region,

$$I_{BC} = \left[\sum_{N=0}^{N_m - 1} A_{N_m}\right] \times \left[\sum_{N=0}^{N_m - 1} A_{N_m}^{*}\right] \qquad (B.36)$$

$$I_{BC} = 2 r^2 N_m^4 \frac{\left[1 - \cos(N_m \zeta)\right]}{(N_m \zeta)^2} \qquad (B.37)$$

Hence the final expression for I_{AD} is

$$\frac{r^2 N_m^4}{(N_m \zeta)^2} \left[2W_{AB}\left[1 + X^2 - 2X \cos(N_m \zeta/2)\right] + 2W_{BC}\left[1 - \cos(N_m \zeta)\right]\right] \qquad (B.38)$$

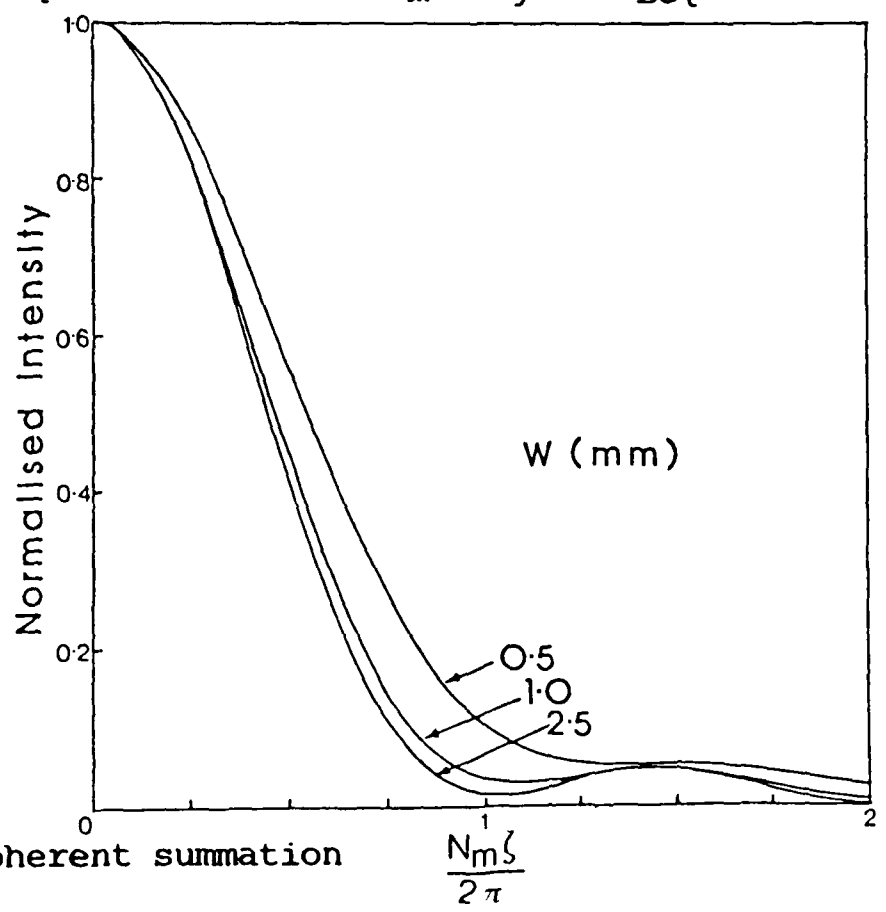

Fig B.7: Coherent summation

The normalised function I_2 has been plotted in Fig B.7 where,

$$I_2\left[W, \frac{N_m \zeta}{2\pi}\right] = \frac{I_{AD}}{I_{AD}(MAX)} \qquad (B.39)$$

For both coherent and incoherent summation, when no absorption is present, the side-lobes will gradually disappear as the width of the incident beam is reduced. For the experimental conditions encountered W ≈ 1 mm, and the blurring will be significant but incomplete.

APPENDIX C

FRINGE WARPING

As discussed in chapter five, the dynamic nature of the holographic recording process can curve the grating planes inside the crystal. This is shown in Fig C.1 below

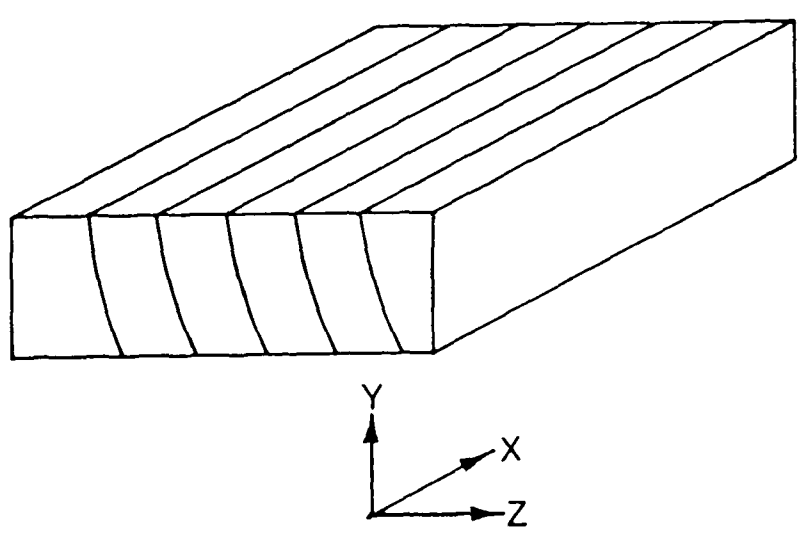

Fig C.1: Warping of fringe planes inside the crystal

The effect of fringe warping on the replay Bragg angle can be determined by introducing a modified $\underline{K}$-vector for the grating

$$\underline{K} = \Delta K(y)\ \hat{\underline{y}} + K\ \hat{\underline{z}} \qquad (C.1)$$

Here the component of $\underline{K}$ along the $\hat{\underline{z}}$ crystallographic axis remains unchanged, but there is a small y-dependent component $\Delta K(y)$ along the $\hat{\underline{y}}$ axis due to the curvature of the fringe planes. As usual, the replay probe beam $\underline{\rho}$ is assumed to propagate at an angle θ inside the crystal, where

$$\underline{\rho} = \beta_R \cos(\theta)\ \hat{\underline{z}} + \beta_R \sin(\theta)\ \hat{\underline{x}} \qquad (C.2)$$

To satisfy the isotropic Bragg condition $|\underline{\rho} - \underline{K}| = \beta_R$, and therefore,

$$\cos(\theta_o) = \frac{K^2 + \Delta K^2}{2\ \beta_R\ K} \qquad (C.3)$$

where β_R is the wavevector magnitude of the light at replay wavelengths Therefore, when $\Delta\theta_o < \theta_o$, the change in Bragg angle ($\Delta\theta_o$) associated with the ΔK component will be

$$\Delta\theta_o \approx - \left[\frac{\Delta K}{2\beta_R}\right]^2 \times \frac{1}{\sin(2\theta_o)} \qquad (C.4)$$

Since $\Delta K(0) = 0$ and $\Delta K(y) \approx \left(\frac{2\pi}{2\ mm}\right)$, whereas $\beta_R \approx \frac{2\pi \times 2{\cdot}23}{(1\ \mu m)}$, $\Delta\theta_o$ is very small ($\approx 10^{-6}$ radians). Consequently, for most practical purposes the curvature of the fringe planes can be neglected.

APPENDIX D

ANISOTROPY OF THE GRATING

Since lithium niobate is a birefringent material, its refractive index will generally have two different values, depending upon the polarisation state of the incident light beam. The two linear, orthogonal polarisation states are called extra-ordinary (denoted here by σ-) and ordinary (denoted here by π-); the σ-state occurring when the incident electric field vector $\hat{\underline{e}}$ lies within the plane containing the beam and the optical axis of symmetry (c-axis), and the π-state when $\hat{\underline{e}}$ is perpendicular to this plane.

Crystal anisotropy will be important at both recording and replay. At recording there is the possibility of forming two distinct gratings with different $\underline{K}$-vectors. This is drawn below, using Ewald's graphical representation, for the general situation when the $\underline{K}$-vector of the grating is not parallel to the c-axis.

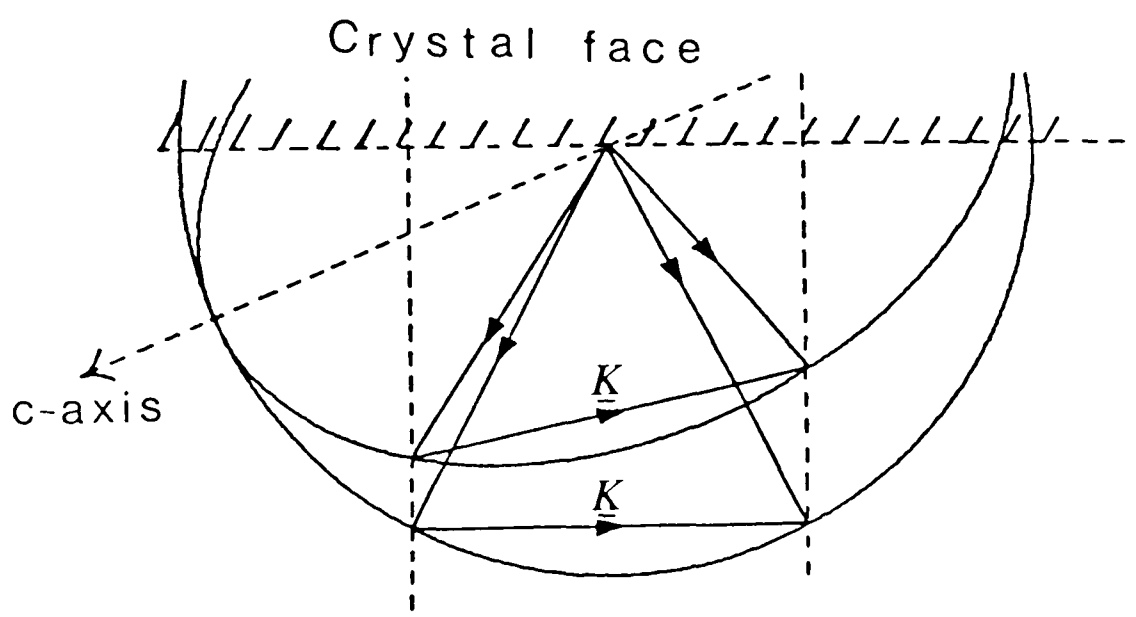

Fig D.1: Anisotropy at recording using Ewald's representation.

Since the polarisation of the recording beams is approximately perpendicular to the plane of incidence, however, the grating formed by the interference of extra-ordinary beams will be very weak and can be neglected.

At replay, there are generally four Bragg interactions associated with one recorded grating, because mode conversion between the ordinary and extra-ordinary polarisation states can occur [73]. In an isotropic medium, only coupling between the two ordinary polarisation states ($\pi\pi-$) and the two extra-ordinary states ($\sigma\sigma-$) is allowed. In an anisotropic medium, however, the situation is more complicated because the tensor properties of the permittivity constant $\tilde{\epsilon}$ must be included. If the grating $\underline{K}$-vector is not exactly parallel to the symmetry axis (c-axis) of the crystal, the modulated permittivity tensor will have non-zero off-diagonal elements and coupling between the polarisation states ($\pi\sigma-$ and $\sigma\pi-$) is possible. This is shown in figure D.2 below. For the infra-red grating discussed here, where the angle between the $\underline{K}$-vector and c-axis is probably only a few degrees, the off-diagonal elements of the permittivity tensor will be small. Under these circumstances $\sigma\pi-$ and $\pi\sigma-$ diffraction will be negligible.

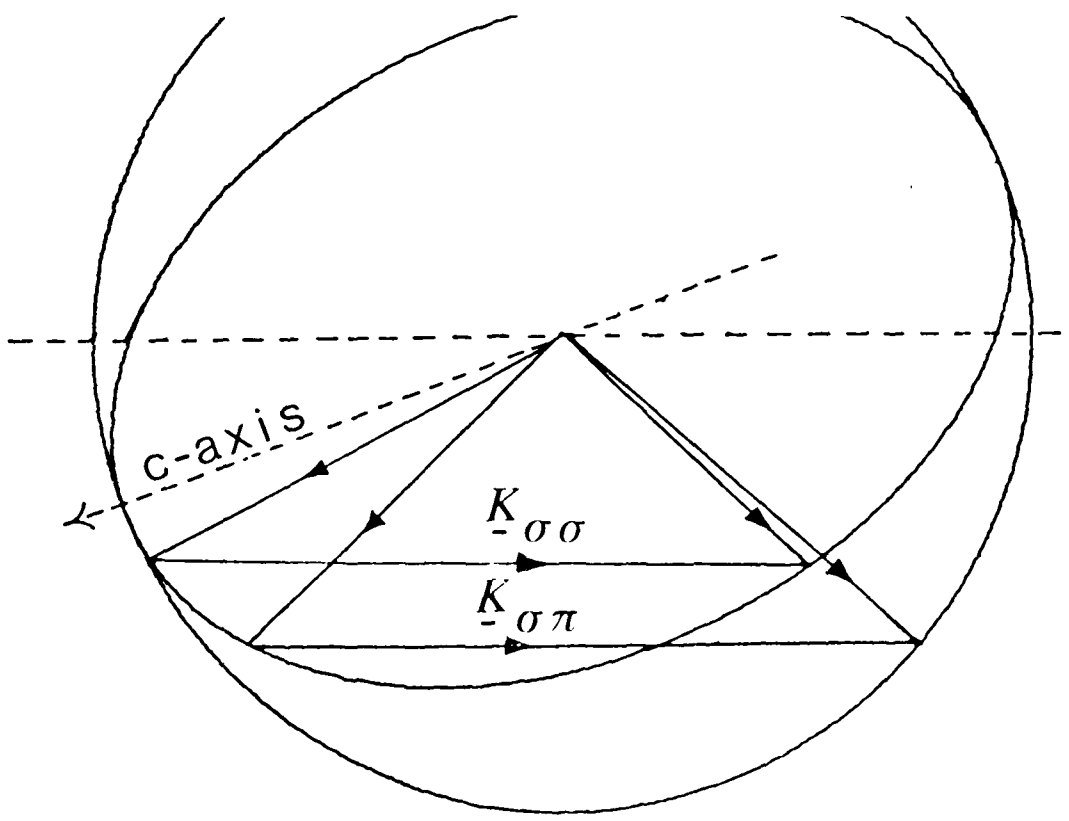

Fig D.2: Mode conversion between ordinary and extra-ordinary polarisation states

The standard replay geometry adopted in chapter five detects only the $\pi\pi$- Bragg interaction of the filter. However, when the polarisation angle of the probe beam is rotated, a $\sigma\sigma$- Bragg interaction at a different replay angle can be observed. Consider, the replay conditions, when $\underline{K}$//c-axis.

Since the difference $\tilde{n}_{ord}(\lambda) - \tilde{n}_{ext}(\lambda)$ between the ordinary and extra-ordinary principal indices of refraction is a positive quantity [11], $\sigma\sigma$- diffraction will occur at an angle closer to normal incidence than $\pi\pi$- diffraction (see Fig D.3 below).

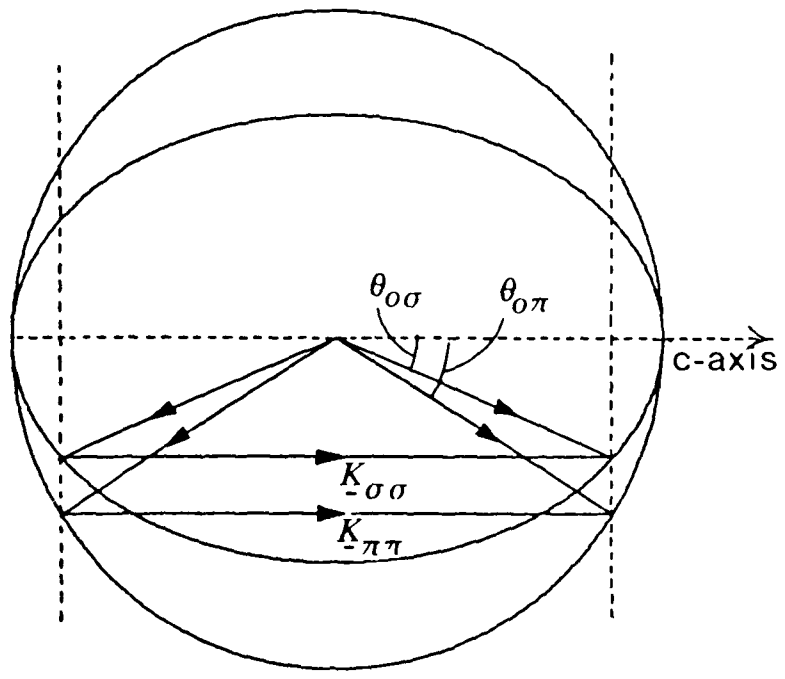

Fig D.3: Anisotropy at replay, assuming $\underline{K}$//c-axis

The index ellipsoid [102] for the probe beam in the σ-state can be mathematically expressed as,

$$\left[\frac{\cos(\theta_{o\sigma})}{\tilde{n}_{ord}(\lambda_R)}\right]^2 + \left[\frac{\sin(\theta_{o\sigma})}{\tilde{n}_{ext}(\lambda_R)}\right]^2 = \left[\frac{1}{\tilde{n}_{\sigma}(\lambda_R)}\right]^2 \qquad (D.1)$$

where $\theta_{o\sigma}$ is the replay Bragg angle for $\sigma\sigma$- diffraction and $\tilde{n}_{\sigma}$ the refractive index seen by the replay beam in the σ-state. For both $\pi\pi$- and $\sigma\sigma$- diffraction to satisfy Bragg's Law,

$$2\,\beta_{\sigma}\cos(\theta_{o\sigma}) = K = 2\,\beta_{\pi}\cos(\theta_{o\pi}) \qquad (D.2)$$

where β equals $2\pi n/\lambda_R$. Expressed in terms of refractive indices,

$$\tilde{n}_{\sigma}\cos(\theta_{o\sigma}) = \tilde{n}_{ord}\cos(\theta_{o\pi}) \qquad (D.3)$$

because,

$$\tilde{n}_{\pi} = \tilde{n}_{ord} \qquad (D.4)$$

Eliminating $\theta_{o\sigma}$ between equations (D.1) and (D.3),

$$\tilde{n}_{\sigma}^2 = \cos^2(\theta_{o\pi})\left[\tilde{n}_{ord}^2 - \tilde{n}_{ext}^2\right] + \tilde{n}_{ext}^2 \qquad (D.5)$$

If the value for $\tilde{n}_{\sigma}$ in equation (D.5) is inserted into equation (D.3) an analytic expression for $(\theta_{o\pi} - \theta_{o\sigma})$ can be produced. In figure D.4 the corresponding difference in external Bragg angles $(\theta'_{o\pi} - \theta'_{o\sigma})$ or δ has been plotted against $\theta'_{o\pi}$, the standard replay angle. Since the exact values of the principal refractive indices are unknown, two curves have been plotted for similar sets of parameters (see legend). Note the sensitivity of δ to small changes in refractive index for large off-normal replay angles.

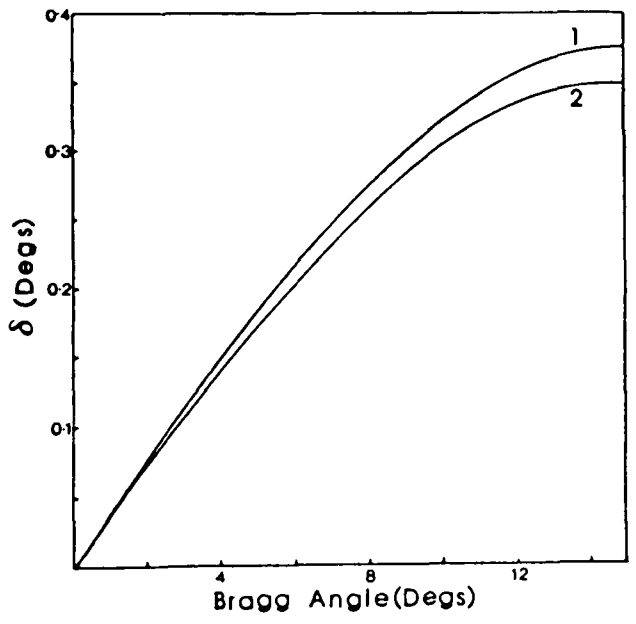

Fig D.4: Difference in external Bragg angle δ for $\pi\pi$- and $\sigma\sigma$- diffraction as a function of replay angle $\theta'_{o\pi}$. Curve (1): $\tilde{n}_{ord} = 2{\cdot}232$, $\tilde{n}_{ext} = 2{\cdot}148$; curve (2): $\tilde{n}_{ord} = 2{\cdot}230$, $\tilde{n}_{ext} = 2{\cdot}150$.

APPENDIX E

MATERIAL PREPARATION

E.1 MATERIAL GROWTH

Good quality iron doped lithium niobate is not readily available and considerable difficulty has been experienced in acquiring suitable crystals. Various sources of the material have been tried. In trying to optimise the quality of the material the following difficulties have been encountered.

i) High cost (≈ £1000 per crystal from Crystal Technology)

ii) Scarcity of good optical quality raw material

iii) Inhomogeneous doping concentration

iv) Thermal shock during poling (the conversion to single ferroelectric domain [70])

The usual source of iron doped material is Crystal Technology, USA. Unfortunately, crystals of suitable dimensions could not be supplied. Crystals ordered from Chiba University, Japan contained visible striations caused by inhomogeneous conditions in the melt. The crystals used in this thesis were cut from a boule grown by Barr and Stroud, Scotland. The boule was pulled along its crystallographic b-axis to improve optical homogeneity. An X-ray topograph across a 3 mm wide Y-cut cross-section of the boule is shown below. The optical quality was generally bad, but a few regions were reasonable. Two 9×3×9 mm^3 blocks were cut from this cross-section of the boule: one with relatively good

optical quality as judged by Barr and Stroud (crystal II) and one with poor quality (crystal I).

Fig E.1: Topograph of a Y-cut cross-section through the boule

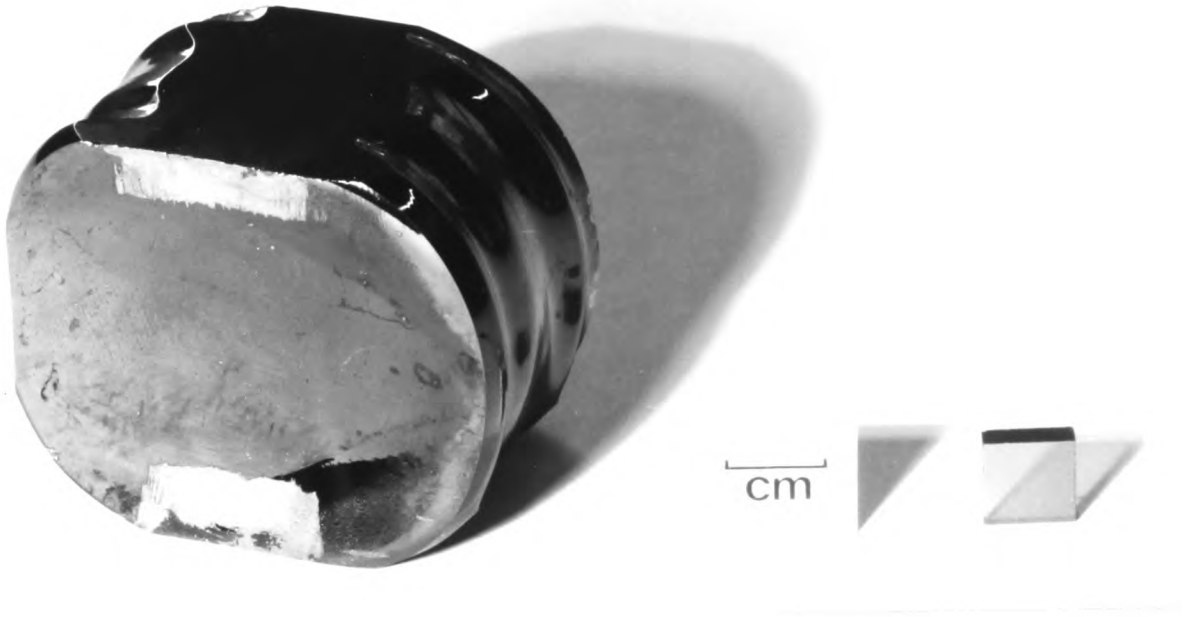

Fig E.2: Boule and cut crystal

E.2 DETERMINATION OF IRON CONTENT

The standard technique for determining the total amount of iron in the crystal relies upon (Electron paramagnetic resonance) EPR. Since it was difficult to acquire the appropriate equipment, an alternative method involving destructive chemical analysis was perfected by the Oxford University Geology Department. The procedure is outlined below:

1) Pressure decompose the sample in a teflon vessel containing HF/HNO_3 in the ratio 1:2 at a temperature of 150°C for about 12 hours.

2) Add to the decomposition products a solution of boric acid H_3BO_3 to neutralise the HF and then dilute to a specified volume.

3) Take measures of this 'master' solution and add increasing concentrations of Fe (in the form of a Ferric Nitrate standard solution).

4) Using the method of standard additions, measure the Fe concentration by atomic absorption spectroscopy (AAS) at 0·2483 μm in spiked and unspiked samples.

5) Compute the Fe concentration in the original sample weight.

The variation in doping level along a longitudinal cross-section of the boule near the surface was measured using this method. From the results obtained at four different points, the graph in figure E.3 was produced. The concentration of iron increased along the boule towards the end immersed in the molten crucible, in accordance with Takei's [88] experimental results.

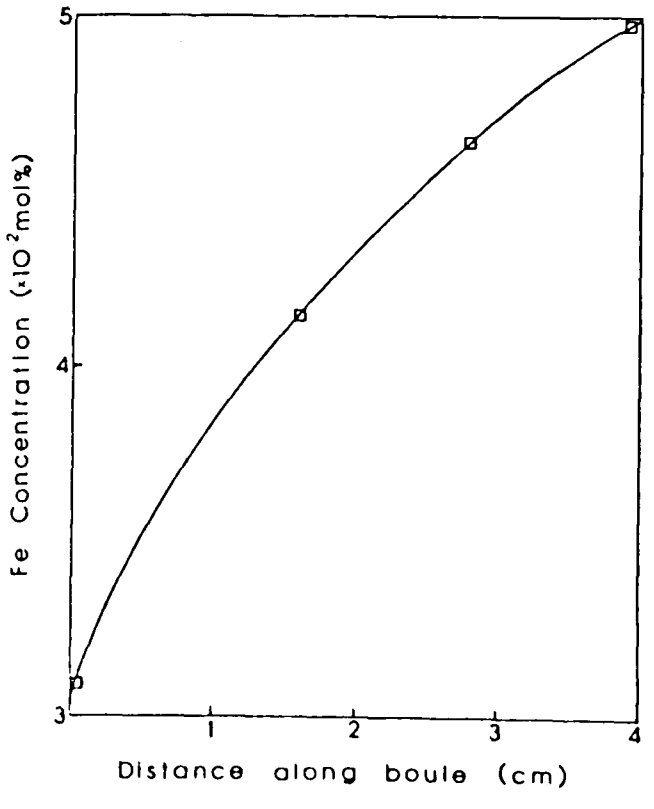

Fig E.3: Doping level profile along a longitudinal cross-section of the boule

The two crystals used for these experiments had a local iron concentration of 0·04 mole% iron.

E.3 ANNEALING

Both the crystals were annealed in an Argon/oxygen enviroment to oxidise the Fe^{2+} ions to Fe^{3+} and thereby reduce the visible absorption of the material. A horizontal furnace containing a quartz tube was used to heat the samples. Chemical contamination was minimised by holding the crystal in a platinum boat and passing gas along the tube.

The temperature inside the furnace was controlled by a digital Eurotherm temperature unit, allowing slow ramping of the crystal temperature up to its final annealing value, a variable 'soaking time', followed by a gradual cooling back to room temperature. To avoid thermal shock, which could crack the crystal, the cooling rate of the furnace was always less than 100°C/hour (the value quoted by Philips [74]).

A few trial runs were undertaken to determine the best annealing conditions. After annealing the crystal for 12 hours at 800°C, no change in the colour of the crystal was observed. Annealing at 850°C for 12 hours, however, began to visibly reduce the crystal colouration.

PUBLICATIONS ARISING FROM THIS THESIS

1. Heaton, J.M., Mills, P.A., Paige, E.G.S., Solymar, L., Wilson, T., "Diffraction efficiency and angular selectivity of volume phase holograms recorded in photorefractive materials" Optica Acta 31, 885-901 (1984).

2. Mills, P.A., Plastow, R., "Single-mode operation of 1·55 μm semiconductor lasers using a volume holographic grating" Electronics Letters 21, 648-649 (1985).

3. Mills, P.A., Paige, E.G.S., "Holographically formed, highly selective, infra-red filter in iron doped lithium niobate" Electronics Letters 21, 885-886 (1985).

REFERENCES

1. Alferness, R.C., Joyner, C.H., Divino, M.D., Buhl, L.L., "InGaAsP/InP waveguide grating filters for $\lambda = 1.5\ \mu m$" Appl. Phys. Lett. 45, 1278-1280 (1984).
2. Alphonse, G.A., Alig, R.C., Staebler, D.L., Philips, W., "Time dependent characteristics of photo-induced space-charge field and phase holograms in lithium niobate and other photorefractive media" RCA Rev. 36, 213 (1975).
3. Alphonse, G.A., Philips, W.D., "Read-write holographic memory with iron doped lithium niobate" Ferroelectrics 11, 397-401 (1976).
4. Amodei, J.J., "Electron diffusion effects during hologram recording in crystals" Appl. Phys. Lett. 16, 22-24 (1971).
5. Amodei, J.J., Philips, W., Staebler, D.L., "Improved electro-optic materials and fixing techniques for holographic recording" Appl. Opt. 11, 390-396 (1972).
6. Ashkin, A., Boyd, G.D., "Optically-induced refractive index inhomogeneities in $LiNbO_3$ and $LiTaO_3$" Appl. Phys. Let. 9, 72-74 (1966).
7. Barkan, L.B., Vorobev, A.V., Lebedev, V.V., Marennikov, S.I., "Volume holographic grating in $LiNbO_3$ as a spatial-frequency selector for a tunable dye-laser" Sov. Tech. Phys. Lett. 5, 308-309 (1979).
8. Biedermann, K., Ragnarsson, S., Komlos, P., "Volume holograms in photographic emulsion of extended thickness" Opt. Comm. 6, 205-208 (1972).
9. Bleaney, B.I., Bleaney, B., "Electricity and magnetism" Published OUP, 306 (1978).
10. Born, M, Wolf, E., "Principles of optics" Published Pergamon Press, 384 (1980).
11. Boyd, G.D., Bond, W.L., Carter, H.L., "Refractive index as a function of temperature in lithium niobate" J. Appl. Phys. 38, 1941 (1967).
12. Bragg, W.L., "The diffraction of short electromagnetic waves by a crystal" Proc. Cambridge Phil. Soc. 17, 43 (1912).
13. Brauchie, C., Wild, U.P., Burland, D.M., Bjorklund, G.C., Alvarez, D.C., "A new class of materials for holography in the infra-red" IBM J. Res. Dev. 26, 217-227 (1982).
14. Burke, W.J., Staebler, D.L., Philips, W., Alphonse, G.A., "Volume phase holographic storage in ferroelectric crystals" Opt. Eng. 17, 308-316 (1978).
15. Chandross, E.A., Tomlinson, W.J., Aumiller, G.D., "Latent-imaging photopolymer systems" Appl. Opt. 17, 566-573 (1978).
16. Chang, B.J., "Dichromated gelatin as a holographic storage medium" SPIE 177, 71-81 (1979).
17. Chen, C., Kim, D.M., Linde, D., "Efficient pulsed photorefractive process in $LiNbO_3$:Fe for optical storage and deflection" IEEE J. Quant. Elect. QE-16, 126-129 (1980).
18. Chen, F.S., LaMacchia, J.T., Fraser, D.B., "Holographic storage in lithium niobate" Appl. Phys. Let. 13, 223-224 (1968).
19. Clark, M.G., DiSalvo, F.J., Glass, A.M., Peterson, G.E., "Electronic structure and optical index damage of iron-doped lithium niobate" J. Chem. Phys. 59, 6209-6219 (1973).
20. Close, D.H., "Holographic optical elements" Opt. Eng. 14, 408-419 (1975).
21. Coleman, D.J., Magarinos, J., "Controlled shifting of the spectral response of reflection holograms" Appl. Opt. 20, 2600-2601 (1981).

22. Cornish, W.D., Moharam, M.G., Young, L., "Effects of applied voltage on hologram writing in lithium niobate" J. Appl. Phys. 47, 1479-1484 (1976).
23. Cornish, W.D., Young, L., Thewalt, M.L.W., "Space charge fields: a fringe technique for observing such fields during hologram writing in $LiNbO_3$" Appl. Opt. 15, 1258-1260 (1976).
24. Croft, T.D., Ritter, J.E., Bhagavatila, V.A., "Low loss dispersion shifter fibre manufacture by the OVD process" Optical Fibre Communications OFC, (1985).
25. Cronin-Golomb, M., Fischer, B., White, J.O., Yariv, A., "Theory and applications of four-wave mixing in photorefractive media" IEEE J. Quant. Elect. QE-20, 12-29 (1984).
26. Decker, G., Herold, H., Rohr, H., "Holography and holographic interferometry with pulse high-power infra-red lasers" Appl. Phys. Lett. 20, 490-492 (1972).
27. Denisyuk, Y., N., "Photographic reconstruction of the optical properties of an object in its own scattered radiation field" Sov. Phys. Dok. 7, 543-545 (1962).
28. Dickson, L.D., Sincerbox, G.T., Wolfheimer, A.D., "Holography in the IBM 3687 Supermarket Scanner" IBM J. Res. Dev. 26, 228-234 (1982).
29. Dukhovnyi, A.M., Korelev, A.E., Ryabova, R.V., Staselko, D.I., "Diffraction efficiency of holograms recorded in the IR region by pulses of 2×10^{-10} to 15 sec duration" Opt. Spectrosc. USSR 49, 510-513 (1981).
30. Duncan, S.S., Mcquoid, McCartney, D.J., "Tunable holographic filters in dichromated gelatin operating in the near infra-red region" Proc SPIE conf Tech. Sympos. Optical and electro-optical Eng. Jan 20-25 (1985).
31. Ewald, P.P., "Crystal optics for visible light and X-rays" Rev Mod Phys. 37, 46-56 (1965).
32. Fisher, J.F., "Wide angle raster head up display" Marconi Avionics (1982).
33. Fleming, M.W., Mooradian, A., "Spectral characteristics of external-cavity controlled semiconductor lasers" IEEE J. Quant. Elect., QE-17 44-59 (1981).
34. Fridkin, V.M., "Review of recent work on the bulk photovoltaic effect in ferro and piezoelectrics" Ferrolectrics 53, 169-187 (1984).
35. Gabor, D., "A new microscopic principle" Nature 161, 777-778 (1948).
36. Gallagher, N.C., Sweeney, D.W., "Infra-red holographic optical elements with applications to laser material processing" IEEE J. Quant. Elect. QE-15, 1369-1381 (1979).
37. Glass, A.M., Linde, D.V., Negran, T.J., "High voltage bulk photovoltaic effect and photorefractive process in $LiNbO_3$" Appl. Phys. Lett. 25, 233-234 (1974).
38. Goodfellow, R., Plastow, R., Monham, K., Carter, A., Ritter, J.E., Croft, T.D., Bhagavatila, V., Gibson, M., "Practical demonstration of 1.3 Gb/s over 107 km of dispersion shifted monomode fibre using a 1.55 μm multimode laser" Optical Fibre Communication Conf. OFC Late News PD5 (1985).
39. Gornall, W.S., "The world of Fabry-Perots" Lasers & Applications, 47-52 (1983).
40. Graube, A., "Infra-red holograms recorded in high-resolution photographic plates with the Herschel reversal" Appl. Phys. Let. 27, 136-137 (1975).
41. Guibaly, F., "Optically induced light scattering and beam distortion in iron doped lithium niobate" Ferroelectrics 46, 201-208 (1983).

42. Hammer, J.M., "Dynamic wavelength stabilisation in a hybrid external Bragg reflecting grating waveguide laser" OFC, 60 (1985).
43. Haruna, M., Koyama, J., "Thermo-optic effect in $LiNbO_3$ for light deflection and switching" Elect. Lett. 17, 842-844 (1981).
44. Heaton, J.M., Mills, P.A., Paige, E.G.S., Solymar, L., Wilson, T., "Diffraction efficiency and angular selectivity of volume phase holograms recorded in photorefractive materials" Optica Acta 31, 885-901 (1984).
45. Heerden, P.J., "Theory of optical information storage in solids" Appl. Opt. 2, 393-400 (1963).
46. Huignard, J.P., Herriau, J.P., Valentin, T., "Time average holographic interferometry with photoconductive electro-optic BSO crystals" Appl. Opt. 16, 2796-2798 (1977).
47. Jordan, J.A., Hirsch, P.M., "Kinoform lenses" Appl. Opt. 9, (1883).
48. Klein, M.B., "Beam coupling in undoped GaAs at 1.06 μm using the photorefractive effect" Opt. Soc. Am. 9, 350-352 (1984).
49. Kogelnik, H., "Coupled wave theory for thick hologram gratings" Bell Syst. Tech. J. 48, 2909-2947 (1969).
50. Kogelnik, H., "Filter response of nonuniform almost-periodic structures" Bell Syst. Tech. H. 55, 109-126 (1976).
51. Kogelnik, H., Shank, C.V., "Stimulated emission in a periodic structure" Appl. Phys. Lett., 18, 152-154 (1971).
52. Kukhtarev, N.V., Markov, V.B., Odulov, S.G., Soskin, M.S., Vinetskii, V.L. "Holographic storage in electro-optic crystals" Ferroelectrics 22, 949-960 (1979).
53. Kulikov, V.V., Stepanov, S.I., "Mechanisms of holographic recording and thermal fixing in photorefractive $LiNbO_3$" Sov. Phys. Solid State 21, 1849-1851 (1979).
54. Kurtz, H., "Lithium niobate as a material for holographic information storage" Philips Tech. Rev. 37, 116 (1977).
55. Latta, M.R., Pole, R.V., "Design techniques for forming 488 nm holographic lenses with reconstruction at 633 nm" Appl. Opt. 18, 2418-2421 (1979).
56. Leith, E.N., Upatnieks, J. "Reconstructed wavefronts and communication theory" JOSA. 52, 1123-1130 (1962).
57. Linde, D von, Glass, A.M., "Photorefractive effects for reversible holographic storage of information" Appl. Phys. 8, 85-100 (1975).
58. Lippmann, G., "Sur la theorie de la photographie des couleurs simples et composees par la methode interferentielle" J. Physique 3, 97 (1894).
59. Malacara, D., "Optical shop testing", Published Wiley & Sons, 109 (1978).
60. Malin, W., Morrow, H.E., "Wavelength scaling holographic elements" SPIE 240, 2-4 (1980).
61. Markov, V., Odulov, S., Soskin, M., "Dynamic holography and optical image processing" Optics and Laser Technology", 95-99 (1979).
62. Marrakchi, A., Huignard, J.P., "Diffraction efficiency and energy transfer in two-wave mixing experiments with $Bi_{12}SiO_{20}$ crystals" Appl. Phys. Lett. 24, 131-138 (1981).
63. Mikealyan, A.L., "Reflection holograms in iron doped lithium niobate crystals" Sov. J. Quant. Elect. 8, 257-258 (1978).
64. Mitchel, G.R., Grek, B., Johnston, T.W., Martin, F., Pepin, H., "Nanosecond photography at 10.6 microns using sliver halide film" Appl. Opt. 18, 2422-2425 (1979).
65. Moharam, M.G., Young, L., "Reading and optical erasure of holograms stored by the photorefractive effect in lithium niobate" Appl. Opt. 17, 2773-2778 (1978).

66. Moharam, M.G., Gaylord, T.K., Magnusson, R., "Holographic grating formation in photorefractive crystals with arbitrary electron transport lengths" J. Appl. Phys. 50, 5642-5651 (1979).
67. Moharam, M.G., Young, L., "Hologram writing by the photorefractive effect with Gaussian beams at constant applied voltage" J. Appl. Phys. 47, 4049-4051 (1976).
68. Moharam, M.G., Young, L., "Criterion for Bragg and Raman-Nath diffraction regimes" Appl. Opt. 17, 1757-1759 (1978).
69. Murty, M., "Use of a single plane parallel plate as a lateral shearing interferometer with a visible gas laser source" Appl. Opt. 3, 531-534 (1964).
70. Nassau, K. Levinstein, H.J., Loiacono, G.M., "Ferroelectric lithium niobate. 2. Preparation of single domain crystals" J. Phys. Chem. Solids 27, 989-995 (1966).
71. Oates, D.E., Gottschalk, P.G., Wright, P.V., "Holographic-grating acoustic devices" Proc. IEEE Ultrasonics Symp. 1, 97-101 (1984).
72. Owen, M.P., Solymar, L., "Large factor wavelength scaling for a high efficiency volume holographic collector" Proc ICO-12 Ensenada (1980).
73. Petrov, M.P., Pencheva, T.G., Stepanov, S.I., "Light diffraction from volume phase holograms in electrooptic photorefractive crystals" J. Optics (Paris) 12, 287-292 (1981).
74. Philips, W., Staebler, D.L., "Control of the Fe^{2+} concentration in iron doped lithium niobate" J. Electr. Mat. 3, 601-617 (1974).
75. Roche, A.E., Title, A.M., "Tilt-tunable ultra narrow-band filters for high resolution infra-red photometry" Appl. Opt. 14, 765-769 (1975).
76. Schein, L.B., Cressman, P.J., "Pyroelectric induced optical damage in lithium niobate" J. Appl. Phys. 49, 798-800 (1978).
77. Schmahl, G., Rudolf, D., "Holographic diffraction gratings" Progress in Optics XIV, 197-243 (1976).
78. Schmidt, R.V., Cross, P.S., Glass, A.M., "Optically induced crosstalk in $LiNbO_3$ waveguide switches" J. Appl. Opt. 51, 90-93 (1980).
79. Shockley, W., "Electrons and holes in semiconductors" Published van Nostrand Company, 300 (1950).
80. Smith, P.W., "Stabilised single-frequency output from a long laser cavity" IEEE J. Qu. Electr. QE-1, 343-348 (1965).
81. Solymar, L, Jordan, M.P., "Finite beams in large volume holograms" J. Micro. Opt. Acous. 1, 89 (1977).
82. Solymar, L., Wilson, T., Heaton, J.M., "Space charge fields in photorefractive materials" Int. J. Elect. 57, 125-127 (1984).
83. Soskin, M.S., Taranenko, V.B., "Hologram filter telescope" Sov. Tech. Phys. Lett. 5, 38-39 (1979).
84. Staebler, D.L., Amodei, J.J., "Thermally fixed holograms in $LiNbO_3$" Ferroelectrics 3, 107-113 (1972).
85. Staebler, D.L., Burke, W.J., Philips, W., Amodei, J.J., "Multiple storage and erasure of fixed holograms in Fe-doped $LiNbO_3$" Appl. Phys. Let. 26, 182-184 (1975).
86. Stover, H.L., Steier, W.H., "Locking of laser oscillators by light injection" Appl. Phys. Lett 8, 91-93 (1966).
87. Su, S.F., Gaylord, T.K., "Determination of physical parameters and processes in hologram formation in ferroelectrics" J. Appl. Phys. 47, 2757-2758 (1976).
88. Takei, H., Katsumata, T., "Properties of congruently-melting $LiNbO_3$ - Fe_2O_3 solid-solution single crystals" Japanese J. Appl. Phys. 21, 994-998 (1982).
89. Takeshi, I, Machida, S. Naivata, K., Ikegami, T., "Intensity fluctuations in each longitudinal mode of a multimode AlGaAs laser" IEEE J. Quant. Elect. QE-13, 574-579 (1977).

90. Tomlinson, W.J., "Wavelength multiplexing in multimode optical fibres" Appl. Opt. Let. 16, 2180-2194 (1977).
91. Tomlinson, W.J., Chandross, E.A., Weber, H.P., Aumiller, G.D., "Multi-component photopolymer systems for volume phase holograms and grating devices" Appl. Opt. 15, 534-541 (1976).
92. Tsang, W.T., Olsson, N.A., Logan, R.A., "High-speed direct single-frequency modulation with large tuning rate and frequency excursion in cleaved-coupled-cavity semiconductor lasers" Appl. Phys. Lett. 42, 650-652 (1983).
93. Tsang, W.T., Shyn, W., "Simultaneous exposure and development technique for making gratings on positive photoresist" Appl. Phys. Lett. 24, 196-199 (1974).
94. Vahey, "A nonlinear coupled-wave theory of holographic formation in ferroelectric materials" J. Appl. Phys. 46, 3510 (1975).
95. Verber, C.M., Wood, V.E., Kenan, P., Hartman, N.F., "Large-angle optical switching in waveguides in $LiNbO_3$" Ferroelectrics 10, 253-256 (1976).
96. Vinetski, V.L. et al, "Amplification of coherent light beams by dynamic holograms in ferroelectric crystals" Izvest. Acad. SSSR Ser. Fizi 41, 135-143 (1977).
97. Volk, T.R., Ginzberg, A.V., Kovalevich, V.I., Shuvalov, L.A., "Electric fields during photorefraction in $LiNbO_3$ - Fe crystals" Izvestiya Academii Nauk SSSR Seriya Fizicheskaya 41, 783-787 (1977).
98. Vormann, H., Weber, G., Kapphan, S., Kratzig, E., "Hydrogen as origin of thermal fixing in $LiNbO_3$:Fe" Solid State Com. 40, 543-545 (1981).
99. Wood, V.E., Rand, C., Sherman, C., "Infra-red holographic gratings in lithium niobate optical waveguides by a two-step process" Ferroelectrics 50, 155-160 (1983).
100. Wood, V.E., Sherman, R.C., Hartman, N.F., Verber, C.M., "Optical erasure of one and two photon holograms in Fe-doped lithium niobate" Ferroelectrics 34, 175-178 (1981).
101. Woods, R.J., Young, L., "Spatial phase shift during hologram writing in lithium niobate" Ferroelectrics 46, 275-280 (1983).
102. Yariv, A., "Introduction to optical electronics" Published Holt, Rinehart, Winston, 251 (1976).
103. Yasuhira, T., Mitsuhashi, Y., Morikawa, T., Shimada, J., Kamijo, T., "Electrically accessible Lippmann hologram memory" Appl. Opt. 16, 2532-2534 (1977).
104. Zhdanova, V.V., Klyuev, V.P., Lemanov, V.V., Smirnov, I.A., Tikhonov, V.V., "Thermal properties of lithium niobate crystals" Sov. Phys. Solid. State. 10, 1360-1361 (1968).